

COMPUTATIONAL MODELING OF GLOW DISCHARGE-INDUCED FLUID
DYNAMICS

By

BALAJI JAYARAMAN

A DISSERTATION PRESENTED TO THE GRADUATE SCHOOL
OF THE UNIVERSITY OF FLORIDA IN PARTIAL FULFILLMENT
OF THE REQUIREMENTS FOR THE DEGREE OF
DOCTOR OF PHILOSOPHY

UNIVERSITY OF FLORIDA

2006

Copyright 2006

by

Balaji Jayaraman

This document is dedicated to my parents and all my teachers from whom I have learnt
all my life.

ACKNOWLEDGMENTS

I would like to thank my advisor, Professor Wei Shyy, for his advice, inspiration, patience and mentoring. He constantly provided insightful suggestions when I needed help and motivation.

I would also like to express gratitude to my committee members: Dr. Siddharth Thakur, Professors Corin Segal, Toshi Nishida, Lou Cattafesta and William Lear. A special mention needs to be made of Dr. Thakur for his suggestions regarding the thesis content. I have also gained significantly from the various technical discussions which I have had with him. Finally, I am forever indebted to my parents for their understanding and support when required. This acknowledgement will not be complete without the mention of the role played by my research group members for their support and friendship.

TABLE OF CONTENTS

	<u>page</u>
ACKNOWLEDGMENTS	iv
LIST OF TABLES	vii
LIST OF FIGURES	ix
NOMENCLATURE	xii
ABSTRACT	xiv
1 INTRODUCTION	1
1.1 Overview of Plasma Generation and Dielectric Barrier Discharges (DBD's)	1
1.2 Plasma Actuator Operating Mechanism	3
1.3 Numerical Challenges	6
1.4 Overview of Present Approach	7
1.5 Outline of the Dissertation	9
2 LITERATURE REVIEW	12
2.1 Review of Experimental Discharge Plasma Studies	12
2.1.1 Early Discharge Studies	13
2.1.2 Mechanism of Plasma-Induced Flow Applications	15
2.1.3 Aerodynamic and Control Strategies Using Glow Discharges	20
2.2 Review of Discharge Modeling Studies	25
2.2.1 Phenomenological Modeling of the Plasma Actuator	26
2.2.2 First Principles-Based Plasma Modeling Approaches	27
2.2.2.1 Review of dielectric barrier discharge (DBD) modeling studies	27
2.2.2.2 Review of plasma actuator modeling studies	33
3 NUMERICAL MODELING OF GLOW DISCHARGE PLASMA	36
3.1 Plasma Modeling Hierarchy	36
3.1.1 Kinetic Modeling Approach	38
3.1.2 Hybrid Modeling Approach	42
3.1.3 Fluid Modeling Approach	44
3.2 Numerical Modeling of Glow Discharge Plasmas	47
3.2.1 Plasma Discharge Governing Equations	48

3.2.2 Numerical Algorithm.....	59
3.2.3 1-D Parallel Plate Discharge Modeling in Helium.....	74
3.3 Integration of Plasma Dynamics with Fluid Dynamics.....	78
4 MODELING FLUID FLOW WITH PLASMA EFFECTS.....	81
4.1 Body Force Formulation.....	82
4.2 Navier-Stokes Equations with Body Force.....	84
4.3 Modeling a Plasma Actuator Using a Phenomenological Force Model.....	85
4.3.1 Plasma Generation in an Asymmetric Electrode Configuration	85
4.3.2 Linearized Electric Body Force.....	88
4.3.3 Problem Description.....	91
4.3.4 Effect on Flow Structure	93
4.3.5 Effect on Heat Transfer	97
4.3.6 Thrust Estimation	98
4.3.7 Effect of Plasma on Aerodynamics	102
4.4 Self-Consistent Fluid-Model-Based Plasma Dynamics.....	108
4.4.1 Discharge Actuator Setup.....	109
4.4.1.1 Boundary condition.....	111
4.4.1.2 Plasma species initial condition	112
4.4.2 Plasma Structure.....	113
4.4.3 Geometric Effects.....	125
4.4.3.1 Impact of electrode spacing.....	125
4.4.3.2 Impact of lower electrode size	127
4.4.4 Impact of Applied Voltage and Frequency	128
4.4.4.1 Frequency sensitivity.....	129
4.4.4.2 Applied voltage sensitivity.....	130
4.5. Summary.....	131
5 SUMMARY AND FUTURE WORK	134
5.1 Summary and Conclusions	134
5.2 Future Work.....	137
LIST OF REFERENCES.....	139
BIOGRAPHICAL SKETCH	149

LIST OF TABLES

<u>Table</u>	<u>page</u>
1 Representative EHD operating mechanisms.....	18
2 Summary of experimental plasma actuator studies	22
3 Summary of turbulent flow control studies	25
4 Summary of low frequency plasma modeling studies	31
5 Summary of high frequency plasma modeling studies	33
6 Summary of plasma-induced fluid flow modeling studies	35
7 Kinetic model studies of discharge plasmas	40
8 Summary of hybrid modeling studies	43
9 Plasma chemistry considered in a helium discharge.....	46
10 Representative time scales of various processes in a 1-D helium discharge model operating at 10KHz, 1.5KV rms, calculated based on values of parameters.	60
11 Summary of governing equations used in different studies.....	61
12 Different types of boundary conditions for the ions and electrons used in modeling studies.....	76
13 Change in drag coefficient and drag force with Reynolds number	104
14 Change in lift coefficient and lift force with Reynolds number	104
15 Effect of electrode position on aerodynamic and heat transfer properties.....	107
16 Summary of property models employed for the He discharge simulation.	111
17 Summary of boundary conditions for the different variables	113
18 Domain averaged force over the voltage cycle for different waveforms.....	125
19 Domain averaged force over the voltage cycle for different configurations	127

20 Force dependence on the lower electrode size.....	128
21 Domain averaged force over the voltage cycle for different frequencies.....	130
22 Mean domain averaged force over the time cycle for different voltage	130

LIST OF FIGURES

<u>Figure</u>	<u>page</u>
1 Experimental photograph illustrating the EHD effects on a laminar jet of titanium tetrachloride vapor.....	11
2 Generation of glow discharge in various arrangements.....	17
3 1-D Numerical modeling results showing different regions of the discharge gap at the instant when the current is maximum	18
4 A 3-D surface plot of photomultiplier light output from the plasma as a function of time and chordwise distance, for a single AC cycle of the applied voltage.....	21
5 Separation control on a NACA66-18 wing at a $Re=79000$, 16 degrees angle of attack.....	23
6 Streamer front propagation at different instants in a DC voltage	35
7 Levels of plasma modeling	38
8 Parallel plate arrangement for modeling DBD discharge	76
9 Evolution of discharge current over one period of the discharge cycle.....	76
10 Evolution of the gap voltage over one full cycle	77
11 Comparison of peak current species density.....	78
12 Schematic illustration of the plasma-fluid flow modeling framework.	83
13 Schematic of the actuator arrangement with approximate shape of electric field lines. The thickness of the electrodes d is 0.1 mm	86
14 The line A-B constitutes the plasma fluid boundary using linear approximation. The electric field strength outside this line is not strong enough to ionize the air.	89
15 The computational domain used for calculations shows the flat plate with the upper electrode	93
16 Velocity profiles compared at the four different stations	95
17 Effect of the various parameters as seen from the velocity profiles at ST4	96

18 Effect of the body force on the wall shear at ST4.....	96
19 Temperature profile along the wall for $Re=1027$ and $Pr=0.7$	97
20 Comparison of normalized heat flux for different voltages and frequencies.....	98
21 Comparison of the experimental and calculated plasma force for different voltages.....	101
22 A schematic of the computational domain with the flat plate and the electrode. The electrode has negligible thickness in the above arrangement	103
23 Drag variation with angle of attack for various Re . The plasma is operated at 4KV rms and 3KHz.....	103
24 Variation of lift with Re for different angles of attack. The plasma is operated at 4KV rms and 3 KHz.....	106
Nusselt number variation with angle of attack for various Reynolds number. The plasma is operated at 4KV rms and 3KHz frequency	106
26 Streamlines showing flow separation for $Re=333$ and an angle of attack twenty degrees for different positions of the electrode.....	108
27 A representative 2-D asymmetric discharge arrangements	110
28 Sensitivity to initial condition (20KHz, 1KV applied voltage)	114
29 Photo intentisty measurements to depict the observed discharge evolution over a time-cycle.	115
30 Time dependent plasma behavior (5 KHz, 1KV applied voltage).....	115
31 Ion density evolution in the domain over time (5 KHz, 1KV applied voltage).....	116
32 Force evolution over one time cycle (5 KHz, 1KV applied voltage)	117
33 Asymmetric sawtooth voltage waveforms used in the experimental and numerical studies.....	122
34 Experimental results comparing the discharge observed from the two different sawtooth waveforms.....	123
35 Impact of waveform on the species number density.....	123
36 Thrust measurements showing the more efficient	125
37 Axial force integrated over the domain with time (F_x (dynes)) for different waveforms	125

38	3-Different configurations to study the impact of electrode overlap.....	126
39	Time evolution of species number density over one time-cycle (20KHz, 1KV voltage signal)	126
40	Impact of the geometric configuration on the domain integrated force field (20KHz, 1KV voltage signal)	127
41	Three different lower electrode lengths modeled to investigate the effect of increased surface area on the discharge.....	128
42	Impact of lower electrode size	128
43	Charge density and force variation over time for different frequencies	129
44	Charge density and force variation over time for different voltages	130
45	Fx power-law dependence on voltage is compared for two different numerical models	131

NOMENCLATURE

n_j, n_i, n_e	Species number density
N	Gas number density
u_j, v_i, v_e	Velocity
ϕ	Potential
E	Electric field
T	Temperature of various species
$\mathcal{E}_{i,e,j}$	Species internal energy
γ_i	Ratio of specific heats
$\mu_{i,e,j}$	Species mobilities
$D_{i,e,j}$	Species diffusivities
$m_{i,e,j}$	Species mass
R_c, R_d	Creation/destruction of species
ν_c, ν_D	Creation/destruction frequencies
K_C, K_D	$\nu_c / N, \nu_D / N$
R_{ij}	Number density gain/loss from reaction
S_{ij}	Number density gain/loss from inelastic collisions
ν_{ij}	Elastic collision frequencies
q_j	Charge carried by j^{th} species
e	Elementary electronic charge

ε_0	Permittivity of free space
K	Boltzmann constant
R_m	Momentum loss from collision
$\nu_{m(i,e)}$	Momnetum loss collision frequency
K_m	ν_m / N
P_e	Electron pressure
R_{en}	Energy loss term
Q_e	Electron heat conduction
ε_T	Species thermal energy
τ_w	Driving/operating time scale
τ_c	Creation/ionization characteristic time
τ_{dr}	Species drift characteristic time
τ_{diel}	Dielectric relaxation characteristic time
C_i	Ion/species sound speed
C_e	Electron sound speed
C_{fluid}	Fluid sound speed
F_{tave}	Time-averaged body force
F_{coll}	Force resulting from species collision losses

Abstract of Dissertation Presented to the Graduate School
of the University of Florida in Partial Fulfillment of the
Requirements for the Degree of Doctor of Philosophy

COMPUTATIONAL MODELING OF GLOW DISCHARGE-INDUCED FLUID
DYNAMICS

By

Balaji Jayaraman

August, 2006

Chair: Wei Shyy

Major Department: Mechanical and Aerospace Engineering

Glow discharge at atmospheric pressure using a dielectric barrier discharge can induce fluid flow and operate as an actuator for flow control. The largely isothermal surface plasma generation realized above can modify the near-wall flow structure by means of Lorentzian collisions between the ionized fluid and the neutral fluid. Such an actuator has advantages of no moving parts, performance at atmospheric conditions and devising complex control strategies through the applied voltage. However, the mechanism of the momentum coupling between the plasma and the fluid flow is not yet adequately understood. In the present work, a modeling framework is presented to simulate athermal, non-equilibrium plasma discharges in conjunction with low Mach number fluid dynamics at atmospheric pressure. The plasma and fluid species are treated as a two-fluid system exhibiting a few decades of length and time scales. The effect of the plasma dynamics on the fluid dynamics is devised via a body force treatment in the Navier-Stokes equations. Two different approaches of different degrees of fidelity are

presented for modeling the plasma dynamics. The first approach, a phenomenological model, is based on a linearized force distribution approximating the discharge structure, and utilizing experimental guidance to deduce the empirical constants.

A high fidelity approach is to model the plasma dynamics in a self-consistent manner using a first principle-based hydrodynamic plasma model. The atmospheric pressure regime of interest here enables us to employ local equilibrium assumptions, signifying efficient collisional energy exchange as against thermal heating from inelastic collision processes. The time scale ratios between convection, diffusion, and reaction/ionization mechanisms are $O(10^7)$, making the system computationally stiff. To handle the stiffness, a sequential finite-volume operator-splitting algorithm capable of conserving space charge is developed; the approach can handle time-step sizes in the range of the slowest species convection time-scale. The Navier-Stokes equations representing the fluid dynamics are solved using a well-established pressure-based algorithm. A one-dimensional two-species plasma model was employed as a test case for validation purposes. The momentum coupling is primarily caused by the combination of factors which include discharge chemistry, individual species transport properties, geometric construction and the nature of the insulator and electrode material. Overall, the paraelectric momentum coupling mechanism is due to the cumulative effect over time of the force field in the domain, as seen from our computations.

Parametric studies conducted on the operating variables such as voltage. Frequency and geometric arrangements indicated strong agreement with the observed experimental work. The applied voltage indicated a power-law dependence on the voltage for the measured force in the domain.

CHAPTER 1 INTRODUCTION

This dissertation deals with the computational modeling of discharge processes and the accompanying plasma-fluid interaction with focus on the asymmetric electrode dielectric barrier plasma actuator and its applications. In particular we focus our attention on the operating mechanism and thermo-fluid effects of the discharge plasma actuator (see Figure 1) which generates efficient surface plasma using a dielectric barrier arrangement capable of interacting with the near-wall flow structure through momentum injection. In this chapter we will present (i) a brief overview and background of the discharge operating processes in the actuator (ii) the mechanism of operation of the plasma actuator and momentum injection to the flow (iii) the state of the research of the discharge-induced fluid mechanics and their numerical modeling. Finally we will present an outline of the various issues addressed and the overall organization of the present dissertation.

1.1 Overview of Plasma Generation and Dielectric Barrier Discharges (DBD's)

The plasma is defined as a quasineutral particle system in the form of gaseous or fluid-like mixtures of free electrons and ions, frequently also containing neutral particles [1]. Based on the extent of ionization, one observes either fully ionized or weakly ionized plasma. Typically, such ionization is realized in gases when a sufficiently large potential is applied under conditions of low pressures such as in vacuum discharges [1]. However, the advent of dielectric barrier discharges (or in short DBD's) presents an efficient mode

of volume plasma generation at atmospheric pressure conditions at which the potential for applications are enormous.

Dielectric barrier discharges have been studied since mid-nineteenth century when they were identified in the context of ozone generation (Siemens [2]). Since then, they have been the focus of extensive interest generated by their use in a wide variety of applications such as surface treatment, excimer ultraviolet lamps [3], large area flat plasma display panels [3] etc. Recent applications have taken this a step further by using the concept of the DBD to generate surface electro-hydrodynamic (EHD) flows [4] which have potential for flow control, thermal management among other applications.

DBD's are very attractive for industrial applications because they can provide non-equilibrium plasma conditions at atmospheric pressure. Typically, discharges at high pressure tend to develop into filamentary or arc type discharges which are unsuitable for certain applications. However, in recent years, homogeneous glow discharges have also been obtained at atmospheric pressure which can be used for large volume applications, surface treatment. The DBD provides a mechanism for generating uniform discharge at atmospheric pressures without arc formation. Typical discharge configurations use planar or cylindrical arrangements with a dielectric layer (e.g. glass, quartz, polymers) placed between the electrodes. The discharge gaps usually range from less than a millimeter to a few centimeters depending on the application [3]. The most interesting property of these discharges is that, at about atmospheric pressure, the breakdown is initiated in the form of a large number of independent current filaments which are known as microdischarges. These discharges are characterized as weakly ionized plasma channels which resemble high pressure glow discharges. Due to the charge build-up at the dielectric surface in a

short time after breakdown, the electric field in the discharge region is reduced, thus making it self-limiting. The short duration of the discharge current limits the energy dissipation and consequently results in little gas heating (hence, the plasma being athermal) and reduces power consumption. In recent years, homogeneous glow discharges have been generated at atmospheric pressures in DBD configurations [4-7]. Such a discharge generation mechanism has been used by Roth [5] to devise a source of uniform and stable surface plasma. It has been known that EHD is one of the efficient modes of flow control in an ionized gas [4]. The EHD induced flow is schematically illustrated below in Figure 1. The figure shows the effect of the plasma generated EHD flow on a surface using smoke flow visualization as reproduced from [4]. The dominant effect on the flow can be seen from the bending of the jet and re-emerging as a wall jet. This can be easily used to inject momentum in regions of adverse pressure gradients, boundary layers etc. Significant attention has been devoted to boundary layer flow control using methods such as synthetic jets [8]. The present method has the advantage of non-moving parts, small size, performance at atmospheric conditions and capacity for complex unsteady flow actuation. But, issues such as power consumption, force generation mechanism and optimum operating conditions have still not been adequately addressed. In this dissertation, we will focus on developing numerical models (both first principle-based high-fidelity as well as phenomenological approaches) to study the momentum generation and the thermo-fluid potential of these devices.

1.2 Plasma Actuator Operating Mechanism

The exact mechanism of electrohydrodynamic (EHD) flow generation is not sufficiently understood although the concept behind the force generation is widely perceived to be that of Lorentzian collisions. The piezoelectric effects arising from the

electric field gradient accelerate the ions which transfers momentum to the neutral fluid [4]. The effect of the plasma on the fluid is like a localized body force [9] on the neutral particles. Most of the investigations so far have been based on experimental observations and empirical arguments using approximate models [4,9] until recently. The above mentioned EHD effects involve the interaction between the discharge physics and the near-wall flow physics. In order to systematically explain the plasma fluid interaction, detailed modeling studies are required. Such studies should attempt to address the complex plasma physics and its interaction with flow physics. The coupled plasma-fluid problem is inherently non-linear by nature, just because one is forced to treat the fluid and plasma as separate entities which interact. It will be shown later in chapters 3 and 4 that the disparity in the fluid and plasma time scales can be used to decouple their solution methodologies. Moreover, the EHD flow can itself be of a different length scale as compared to the mean flow. Resolving these multiple scales is a challenging computational task. Also, the modeling of plasma dynamics in itself involves a convection-diffusion-reaction system operating over widely varying time and length scales.

The interaction between the aerodynamic motion of an electrically conducting medium and an electromagnetic field is of great interest in astro-physics; interstellar gas masses etc and is studied under magneto-aerodynamics. The potential of electromagnetic effects in enhancing aerodynamics performance have been discussed and reviewed by Shang et al. [10].

Mechanism of flow control using plasma studied in non-equilibrium hypersonic flows is fundamentally different from the EHD type mechanism described above. Here,

the ionized flow modified in the presence of electromagnetic fields represents the interplay of aerodynamics, electromagnetism, chemical physics, and quantum physics. This is encountered in hypersonic flights where, the air mixture bounded by the bow shock consists of highly energized internal energy modes and at high temperatures around 5000 K ionization is encountered. This ionized air mixture will interact with the electromagnetic field causing Lorentz force effects to affect the aerodynamic forces. This Lorentz force becomes significant at high altitudes and high speeds which are used to accelerate or decelerate a gas continuously at subsonic or supersonic speeds without choking even in constant cross section channels. However, this is achieved by coupling the velocity and the temperature of the conducting media through Joule heating effects. In other words, the Joule heating from the electromagnetic effects can significantly alter the thermal equilibrium. Research on shock wave propagation in plasma has been studied by Rivir et al. [11] and high speed flow control using weakly ionized plasma by Leonov et al. [12]. The studies reveal that at high speed non-equilibrium flows the weakly ionized gases can substantially modify a traveling shock wave. A propagating shock wave in a plasma decreases in strength and the wavefront disperses. Significant aerodynamic drag reduction via plasma injection in the stagnation region has been reported in the studies of Rivir et al. The origin of this drag reduction is not completely understood, but the non-equilibrium thermodynamics and the electromagnetic forces play significant roles. The modification of the flow field structure due to non-equilibrium thermodynamic phenomena is caused in two ways. The energy from the weakly ionized plasma energy source modifies the local gas temperature and reduces the Mach number upstream of the bow shock. Secondly, the non-equilibrium energy distribution among internal degrees of

excitation can also alter the thermodynamic properties within the shock layer. Also, in low supersonic flows, the high amounts of energy deposition upstream of the shock can make the flow locally subsonic. The modeling of the plasma effects in non-equilibrium effects also involves significant complications as intrinsic plasma properties such as transport properties, conductivity etc. need to be calculated from kinetic modeling studies and not from the equilibrium Maxwellian distribution assumption used in fluid models. However, the focus of the present research is the low Mach number flow regime where non-equilibrium effects are minimal and, moreover, the plasma dynamics is mainly shaped by the electromagnetic effects and to a lesser extent by the background low-speed neutral flow.

1.3 Numerical Challenges

Computational studies of the dielectric barrier discharges have been attempted for parallel plate arrangements with emphasis on modeling the plasma physics in detail [13]. The time and length scales operating in the plasma extend over a vast range, warranting kinetic models in the extreme case (highly non-equilibrium, low pressure, high frequency (RF) discharge conditions) to relatively simpler plasma-fluid models for equilibrium, high pressure plasmas. The latter is still an approximate model, but valid in certain situations such as at high pressures where equilibrium velocity distribution functions and isotropy assumptions for pressure gradients can be used in spite of the large electrostatic effects. Even modeling the evolution of the plasma discharge with reasonable complexity using a fluid model is computationally challenging and expensive due to

- strong non-linearities between the plasma-fluid equations and the electrostatics
- widely varying spatial and temporal scales, especially near the electrodes.

Most of the computational work in the area of plasma modeling has been done for high frequency discharges and for parallel plate arrangements which can be extended to complex arrangements used in flow control studies. Keeping in mind the computational cost, 2-D or higher dimensional discharge modeling studies are less common. More recently Roy et al.[14-18] have developed a finite-element method based 2-D modeling of such plasma-based actuators by solving for the discharge species and neutral transport. Although the model used only three species (ions, electrons and neutrals) in a 2-D framework, the computational time was significant (a week of computational time for a typical actuator configuration). However, the plasma and the neutral fluid display three-dimensional characteristics as reported from experimental observations. Also, the extent of plasma chemistry to be included is a compromise between exact physics and computational cost. Involving a large number of species will mean that we have to solve many transport equations and consequently a hugely coupled system. However, we will see in later chapters that the impact of the ion species (both positive and negative which are largely responsible for the collision dominated momentum transfer) on the evolution of the discharge and electric force field is significant as deduced from the discharge structure.

1.4 Overview of Present Approach

The key to modeling the DBD effects in fluid dynamics is to achieve realistic distributions of the species densities and their momentum in the domain which interacts with the neutral fluid by solving the plasma fluid equations. As a first step to model these effects we developed a phenomenological model [9] based on a linear force distribution in the domain. This linearized body force model was later adopted by Gaitonde et al. [14] for modeling plasma-based separation control in a NACA 0015 wing section. This model

was an attractive option because of the difficulty in achieving efficient multi-dimensional and self-consistent plasma dynamics simulations coupled with largely unsteady fluid dynamics.

This was followed up by a first principles-based self-consistent modeling of the plasma-dynamics using a hydrodynamic model in helium gas. This multi-fluid formulation to model the radio-frequency discharge in helium gas gives the spatial and temporal evolution of the charges species which is decoupled from the neutral fluid dynamics. The body force calculated from this data provides a more self-consistent way of modeling the plasma-fluid flow interaction.

The wide range of operating length and time scales characterizing both the discharge and flow physics resulting in a highly stiff system of equations and is a major limiting factor in achieving fully-coupled multi-dimensional plasma-fluid simulations. In this dissertation, we clarify some of the important computational issues pertaining to handling the multiple scales, while offering insight into improving our computational capability for modeling practical, multi-dimensional physics.

Both sequential and fully implicit approaches [15] have been used for discharge modeling. In the present multiple scale problem, we have employed an operator-split sequential solution algorithm in which the solution procedure can be adapted to handle the individual processes efficiently and realize overall gain in computation. This method is integrated with a multi-block finite-volume algorithm capable of handling 3-D curvilinear grids [19]. The method is employed to model the plasma dynamics in an asymmetric electrode configuration similar to that shown in Figure 1.

1.5 Outline of the Dissertation

The remaining document is organized as follows. In chapter 2, we present a review of the various studies on discharge plasma to provide a reasonable understanding of their generation and operating mechanisms. The first section is devoted to experimental studies aimed at analyzing the discharge operating characteristics and structure followed by some potential fluid flow control applications using the surface plasma arrangement. A brief glimpse is provided into the possible potential of these plasma actuators in a turbulent regime along with laminar separation control, drag reduction etc. The next section reviews the various numerical modeling efforts of discharges operating in high and low frequency regimes. These give a view of the various versions of models employed to study the plasma discharge in one and two dimensions. Further, we also look at some of the contemporary efforts at modeling the discharge plasma actuators in 2-D.

In chapter 3, an overview of the various levels of plasma modeling is presented starting from the studies which solve the Boltzmann equation in a kinetic model which are numerically intractable for large-scale problems. This is followed by a discussion on the hybrid methods which use both kinetic as well as fluid descriptions with the goal of developing an efficient, feasible and accurate description of the processes. The last section presents in detail the various features of fluid models including the various levels of complexity that can be achieved and the set of valid approximations. Motivated by our interest in efficiently handling the plasma equations, we present an overview of the techniques employed to handle such multiple scale processes. A solution framework for the coupled species transport equations and the electrostatics is presented. The wide range of scales needs to be handled using time-split methods and operator splitting

techniques are employed for the source term treatment. With the large difference in the plasma and neutral fluid flow time scales, the Navier-Stokes equations are treated independently from the discharge model. However, the effect of the glow discharge is included in the flow equations as a local body force term which can be evaluated from the quasi steady solution of the plasma-fluid equations. Having developed the modeling framework, a one-dimensional representative modeling study of a parallel plate glow discharge in helium is attempted as a validation exercise against prior modeling [20].

In chapter 4, a body force type coupling is developed in detail to facilitate interaction between the plasma dynamics and the fluid dynamics. A phenomenological body force model based on experimental observations, developed independent of the 1-D plasma model results, is used here to investigate qualitatively the induced flow structure. As a sequel to the above, the fully self-consistent discharge dynamics developed from the hydrodynamic plasma model is presented to provide insight into the discharge structure and the force generation mechanism.

Chapter 5 summarizes the present research status and enunciates the future research goals to be attained.

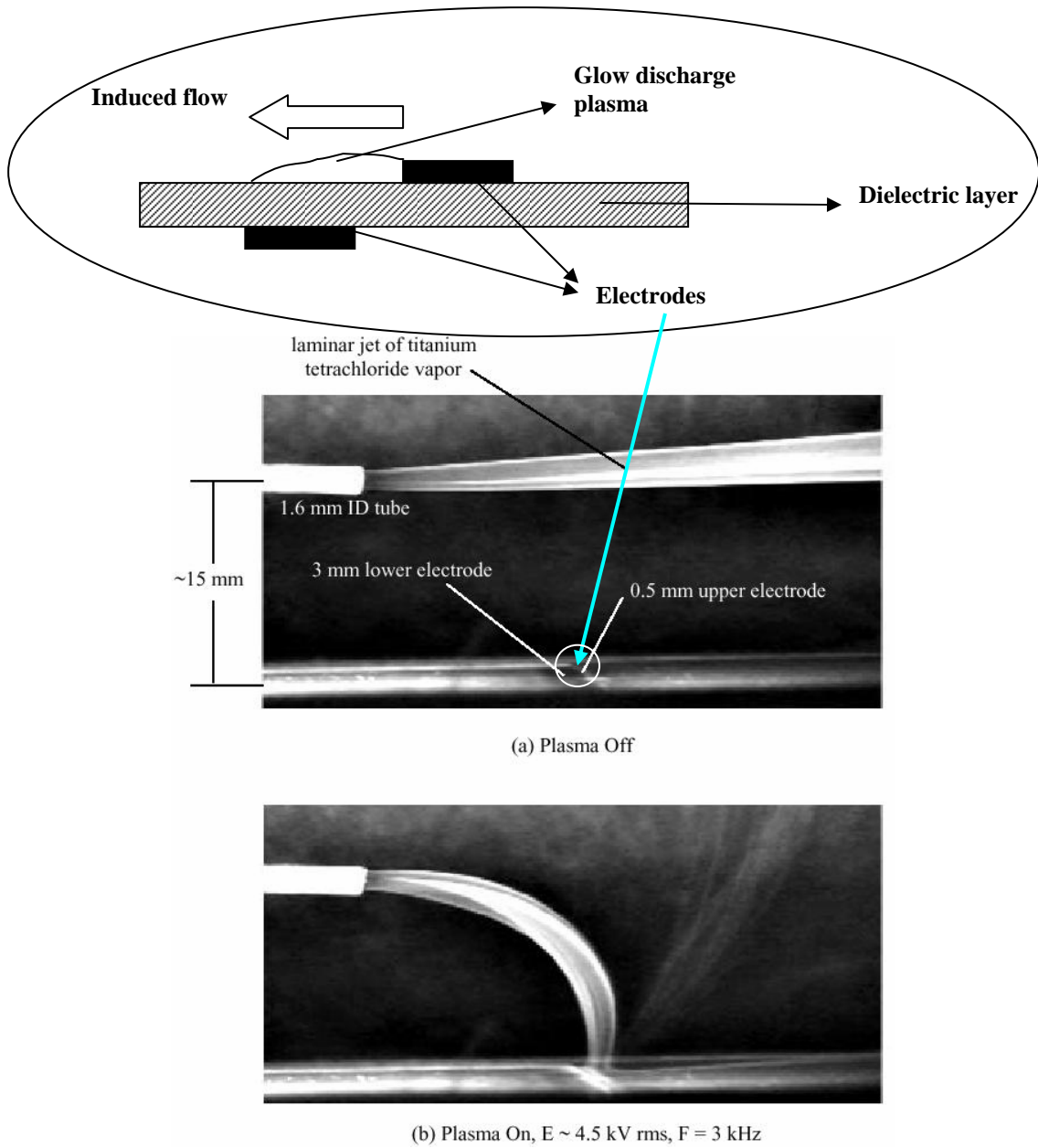


Figure 1 Experimental photograph illustrating the EHD effects on a laminar jet of titanium tetrachloride vapor. The top picture shows the unaffected jet when the plasma is non-existent and the bottom picture shows the effect on the jet which bends and forms a wall jet. Photograph reproduced from [4].

CHAPTER 2 LITERATURE REVIEW

Flow control through various mechanisms has been extensively researched in literature. Recently, the application of surface glow discharge plasmas as flow control devices has attracted particular interest as revealed in experimental studies undertaken in the last few years [5,21-27]. However, numerical studies to complement the above experimental efforts are not too common until recently [28-29,14-18]. The operating mechanism of the high frequency discharges between dielectric barriers has been studied using both experimental and numerical modeling techniques, in the context of surface coating, sterilization, ozone production, plasma display panels (PDP's) [3,6,30,31] etc. In the previous chapter we presented a brief overview of the dielectric barrier discharge plasma actuator, its operating mechanism, potential for thermo-fluid applications and some insight into the current status of the numerical aspect of the research and the associated challenges. Here, we review in detail some of the relevant experimental and numerical studies on discharge plasmas and fluid flows to help better understand the significance of this dissertation. The first section 2.1 is devoted to experimental studies pertaining to discharge actuator mechanisms and applications. The second section 2.2 reviews the various plasma dynamics modeling efforts and concludes with the numerical studies attempted at modeling the discharge-induced fluid flows.

2.1 Review of Experimental Discharge Plasma Studies

In this section we will review some of the experimental efforts to modify flow using the plasma based actuators and their operating mechanism. Initial studies of

Dielectric barrier discharges, characterized by the presence of numerous micro discharges which lead to filamentation of atmospheric air. In these studies, the frequency of the applied voltage usually ranged from line frequency to a few hundred kilohertz. This was first investigated in the context of ozone production. A detailed review of various efforts undertaken is presented in [3].

2.1.1 Early Discharge Studies

It was Kanazawa et al.[5] in the late 1980s, whose work indicated that homogenous glow discharges as against filamentary ones can be obtained under certain conditions. Since then the potential of DBD's in the context of plasma display panels for applications like flat television screens [3] etc. was realized, which led to spurt of research activity aimed at furthering the understanding of plasma dynamics applications. The experimental work on the plasma actuator development took off in the 1990s, when Roth et al.[32] formally devised the generation mechanism of uniform or homogeneous plasma discharges at atmospheric pressure which he called as the OAUGDP or One Atmosphere Uniform Glow Discharge Plasma. The OAUGDP is capable of operating at atmospheric pressure in air and other gases without significant generation of heat. It is non-equilibrium plasma, far from thermodynamic equilibrium. This means that the individual species such as the electron possess energies which are very far apart from the heavier ions as well as the neutral species. The generated plasma is more uniform in the breakdown region and attractive for surface and large volume applications. The active species thus generated had potential for use in sterilization, surface decontamination, increasing surface wettability and surface energy of materials [9]. A schematic of the OAUGDP generator is given in Figure 2. This plasma generation device can be operated

in a wide range of geometrical configurations such as, between two parallel plates or as surface plasma which can cover a flat or curved surface such as an aerofoil.

The asymmetric arrangement in Figure 2b is the source of the surface plasma over an aerofoil, with the direction of the generated electro hydrodynamic (EHD) flow given by the placement of the submerged electrode, i.e., the flow is always seen to be generated from the upstream electrode to the downstream electrode. This EHD flow is caused by the ‘paraelectric’ effect [4] the term given to the flow (say 1-10 m/s) created because of the curved electric field lines as in an asymmetric arrangement shown above in Figure 2c. Only an asymmetric arrangement as shown in Figure 2b generates usable wall jet type flow. There are other symmetric arrangements studied in [4] which by virtue of construction produce vortex flow as against wall jets. The momentum acquired by the ions in such an electric field is coupled to the neutral fluid through Lorentzian collisions. Roth et al.[33] identifies use of these EHD flows or its variants as control tools in aerodynamic boundary layers, pumping gases through tubes or ducts etc. A few key observations of the OAUGDP from these experimental studies [33] are

- Plasma is non-equilibrium and cold with time-dependent features.
- Discharge exhibits classical glow discharge characteristics with identifiable regions as identified by computer modeling in [20,34]
- Ionization occurs at ‘Stoletow’ point with minimum possible energy.

By non-equilibrium, it is implied that the plasma does not have thermodynamic equilibrium and the kinetic temperatures of the species are far from equal to each other. This further implies that the background gas need not be heated till thermodynamic equilibrium. Three prominent EHD based flow effects discussed in [4] are presented in Table 1.

2.1.2 Mechanism of Plasma-Induced Flow Applications

In this section we will present efforts to address the paraelectric flow mechanism. Experimental and analytical studies were conducted by Roth et al.[4,7,33]. Here, EHD body force is modeled as the electrostatic force acting on the charged particles which acts on the neutral gas. The generation of paraelectric effects as a consequence of electric field gradients is illustrated in [32-33]. A brief description of the analytical argument of Roth et al.[33] is given below. If E , is the electric field (V/m) and ρ_c (C/cu.m) is the charge density, then the local electric body force F_E (N) according to Roth et al.[7] is

$$F_E = E \rho_C. \text{ (N)} \quad (1.1)$$

Using Maxwell's equation, we get

$$\nabla \cdot E = \frac{\rho_C}{\epsilon_0} \quad (1.2)$$

Hence,

$$F_E = \epsilon_0 E \nabla \cdot E = \frac{1}{2} \epsilon_0 \nabla \cdot (EE) = \frac{d}{dx} \left(\frac{1}{2} \epsilon_0 E^2 \right) \quad (1.3)$$

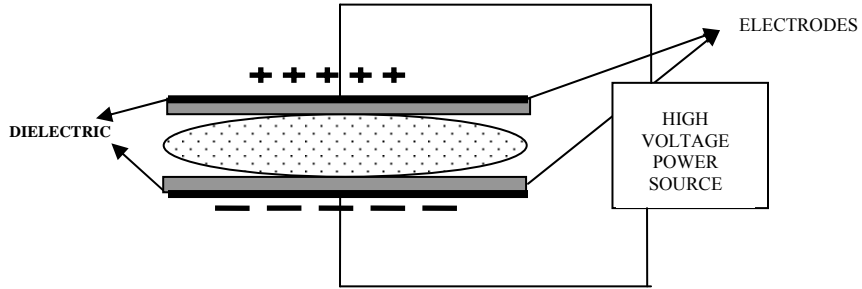
for a one-dimensional case. This formulation for the body force allows viewing it as an electrostatic pressure gradient where,

$$P_E = \frac{1}{2} \epsilon_0 E^2. \quad (1.4)$$

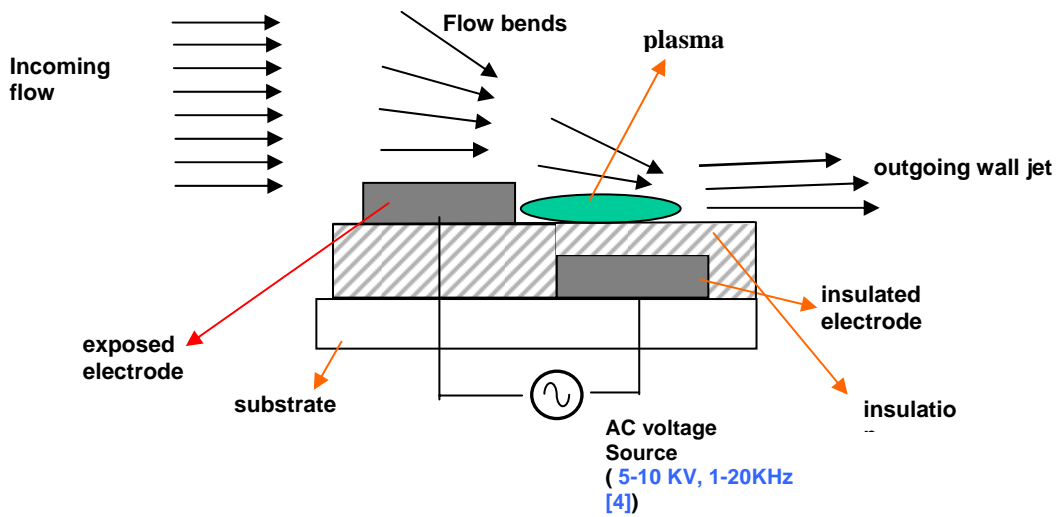
This simplified 1-D interpretation gives a feel for the nature of paraelectric body force effect, but cannot be extended to higher dimensions. Moreover, evaluating the exact distribution of E , requires solving for the charge particle distribution. Nevertheless, the above electrostatic pressure argument gives a feel for the observed phenomenon. The 'paraelectric' effect can be interpreted as the pumping of charged particles towards

regions of increasing electric field gradient. Also, in a quiescent medium, the electrostatic pressure acts as a driving pressure gradient causing the flow from a region of higher pressure to that of a lower pressure as reported from the smoke flow visualization study in [4]. More recently, Enloe et al.[21-22] studied, the plasma morphology and operating mechanism in an asymmetric electrode setup as shown in Figure 2b by means of optical measurements using a Photomultiplier (PMT) tube.

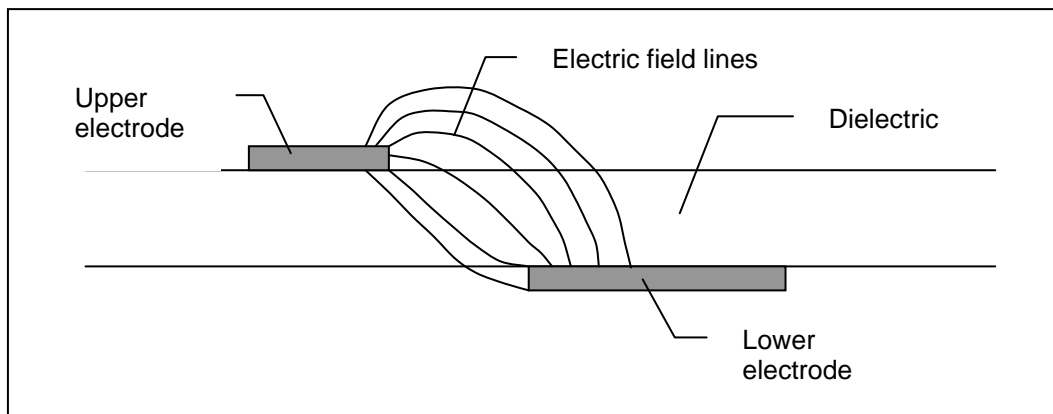
The experimental study revealed characteristic temporal and spatial structure. Computer modeling efforts for parallel plate arrangements in [20,34] showed that the DBD generated in those conditions possessed characteristic low pressure glow discharge qualities with regions such as the Faraday dark space, cathode glow, positive column etc. This is illustrated in the 1-D modeling study by Lee et al [34] as shown in Figure 3. The figure shows the distribution of the electric field and species densities at the instant of peak current which are characteristic of glow discharges. The temporal structure of the DBD generated in an asymmetric arrangement indicated noticeably different discharge patterns in the two half cycles. The light intensity used as a measure of the discharge was consistently regular when the exposed electrode was negative-going and highly irregular when positive-going. Further, it was noticed that a consistently increasing voltage form was necessary to sustain the discharge and the resulting light intensity depends heavily on the rate of increase. Also to study the asymmetry effects further, asymmetric saw-tooth waveforms having vastly different positive-going and negative-going duty cycles were used to model the discharge. The resulting outcome clearly established the preferential phase for the actuator operation during a whole time-cycle.



(a) parallel plate setup



(b) A single asymmetric electrode setup and its effect on fluid flow.



(c) Illustration of distorted field lines in an asymmetric arrangement

Figure 2 Generation of glow discharge in various arrangements such as between parallel plates (a) or as a surface discharge (b) and the curved electric field lines in such a case [9].

Table 1 Representative EHD operating mechanisms

Type of EHD effect	Max speed	Mechanism	Comments
Paraelectric body force effect due to net charge density in the plasma	1-10 m/s	Electric field gradients	Very large collision frequencies (7GHz) ensure adequate momentum by Lorentzian collisions.
EHD convection driven by DC ion mobility drift	300 m/s	DC electric field over a generated OAUGDP causes ion drift	Impractical due to high electric fields of the order of 10^4 V/cm requirement.
Peristaltic EHD plasma acceleration	100 m/s	Series of paraelectric actuators operating at a phase difference	Gives a higher induced flow velocity to work with- most useful and flexible of the three

Note: See [33] for more information.

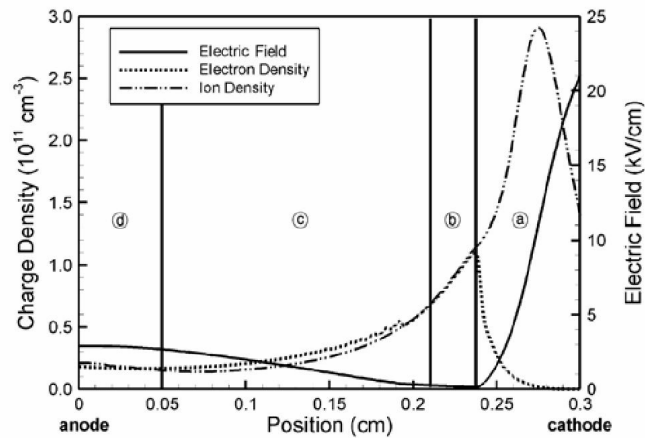


Figure 3 1-D Numerical modeling results from Lee et al.[34] showing different regions of the discharge gap at the instant when the current is maximum for a 10KHz, 1.5KV voltage. a- cathode fall; b- negative glow; c- faraday dark space; d- positive column

While the light intensity measurements of Enloe et al.[21-22], revealed the significant temporal and spatial structure of the discharge in the actuator, it still did not improve the understanding of the nature of momentum coupling. In a follow-up of the above study, Baird et al.[35] investigated the acoustic effects of the plasma actuator. The study revealed that the momentum transfer to the neutral fluid was different in the two halves and the acoustic pattern produced was a radiation pattern characteristic of a

coherently-driven system indicating possible compressibility effects. Near electrode fluid density measurements over time by Enloe et al.[36], indicate density variation in space akin to a pumping-type mechanism resulting in a wall-jet. However, hot-wire temperature and velocity measurements by Jukes et al.[37-38] around the exposed electrode show only a slight increase in ambient temperature of two degrees, thus reducing the possibility of buoyancy driven effects.

In the present dissertation we proposed as part of our phenomenological model (Shyy et al.[9]) that, the asymmetries introduced through the electrode arrangement and the dielectrics along with the asymmetric discharge structure had a significant role to play in the generation of EHD based paraelectric flow or simply glow-discharge induced flow.

It can be seen from Figure 4, that the distinct difference in the light intensity measurements between the two half cycles for asymmetric electrode arrangement. The first half cycle provides a more uniform discharge of high intensity while the other half cycle provides an overall weak light intensity. Overall, the studies on the discharge actuator summarily observed the following:

- Plasma structure is different in the two half cycles which was a fundamental assumption in the development of our phenomenological model (Shyy et al.[9]) and was also suggested in [21] (see Figure 4). It is possible caused by the geometric asymmetry.
- Material asymmetry of the exposed and submerged electrodes only influenced the net plasma intensity and a weak induced flow was present even with both electrodes insulated.
- Direction of flow is purely determined by electrode geometry for the actuator configuration discussed above.
- Mechanism of momentum coupling is yet to be adequately understood with possible reasons ranging from density-variation effects from acoustic measurements to contradicting temperature measurements indicating minimal buoyancy related effects.

It was also perceived from the outcome of our phenomenological model [9] that the net induced flow was a product of the various competing mechanisms listed above. Further, it also highlighted the glaring necessity for detailed multidimensional modeling of the actuator and plasma dynamics towards developing an accurate modeling strategy.

Parametric studies and the impact of the geometry on the actuator performance were studied by Enloe et al.[22] and Van Dyken et al.[26]. Specifically, the impact of voltage frequency, waveforms and geometrical parameters were investigated. Larger thickness of the exposed electrode resulted in more thrust which indicated possible ion concentration near the exposed electrode as they are the primary momentum imparting collision species. Also, a larger thickness can mean a sharper electrode edge while transitioning from the conductor to the insulator surface which can lead to stronger electric fields in the region. The charge species concentration in the plasma will lead to significant Debye shielding effects which can affect electric field distribution. In trying to provide an analytical insight, Enloe et al, discusses the effect of Debye shielding which further illustrates the inadequacy of Roth's electrostatic pressure argument.

2.1.3 Aerodynamic and Control Strategies Using Glow Discharges

Now that we have looked into some of the efforts to understand the plasma actuator operating mechanism, we will look at its various areas of application. The above discussed potential of the surface plasma to generate EHD flow effects whether wall jet type flows or re-circulating flows can be harnessed for a variety of applications. The injection of momentum into the boundary layer and delaying of separation has been primary motives in aerodynamic surface flow control.

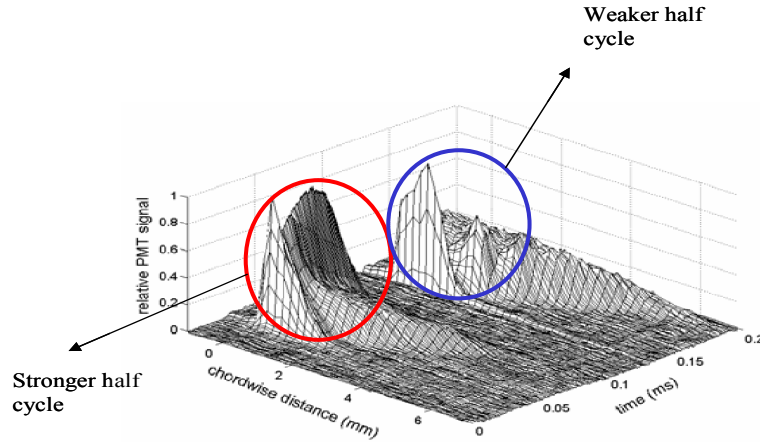


Figure 4 A 3-D surface plot of photomultiplier light output from the plasma as a function of time and chordwise distance, for a single AC cycle of the applied voltage. (Reproduced from Enloe et al.[23])

However, most of the efforts [4,25,39-40] listed indicate effective performance of the plasma actuator from low (10,000) to moderate (100000) Reynolds numbers, essentially limited by energy transfer from the plasma. Van Dyken et al.[26] use a single plasma actuator at 7% chord on a NACA0015 airfoil resulting in substantial increases in lift and reduction in drag beyond the baseline stall angle of attack. Santhanakrishnan et al.[41] present the possibility of using plasma-based flow control for Unmanned air vehicles (UAV's) to control stall and enhance lift, especially in the range of low to moderate Reynolds number range(10^4 - 10^5). Goskel et al.[42] did an experimental investigation of steady and unsteady plasma wall jets for separation control of Micro-air-vehicles in the low Reynolds number regime ($\sim 20,000$). It was observed that a gain in lift by a factor of two and the loss of low Reynolds number hysteresis was achieved using discharge power inputs in the range of 1.2mW/cm. Corke et al.[43], presents the idea of using an unsteady plasma actuator to achieve flow control performance on an airfoil comparable to that of a moving plane flap. This application is interesting for the reason that the unsteady operation was observed to reduce the actuator power consumption up to

ninety percent. Related work includes studies by Corke et al.[24], Rivir et al.[11] and Leonov et al.[12].

Table 2 Summary of experimental plasma actuator studies

Author and year	Work description	Comments
Roth et al(1998) [4]	Boundary layer flow control using plasma actuator arrays	Increase in drag. EHD flow altered boundary layer profile.
Corke et al(2000) [24]	Phased plasma arrays for unsteady flow control	
Corke et al.(2002) [25]	Flow control on a NACA 0009 wing	Lift enhancement and also that of drag (higher skin friction) when typically using single actuators.
Post et al.(2003) [27]	Separation control on a NACA 0066 wing	Increased lift to drag ratio and delays separation.
Roth et al.(2003) [39]	Flow re-attachment using Paraelectric and peristaltic EHD effects on a NACA0015 wing	Peristaltic acceleration is by a traveling electrostatic wave
List et al.(2003) [40]	Laminar separation control on a cascade turbine blade	Separation is quelled at moderate $Re \sim 50000$
Enloe et al.(2004) [21-23]	Experimental visualization of the generated plasma structure in space and time, effect of geometric construction	Plasma structure helped gain insight into the operating mechanism
Rivir et al, (2003) [45]	Turbine flow control with plasma	
Rivir et al.(2004) [11]	AC and Pulsed plasma flow control	AC plasma controls flow through wall jet mechanism and pulsed DC Plasma through heating mechanism
Leonov et al.(2003) [12]	Effect of plasma induced separation	Uses plasma as a local heat source
Chan (2005) [44]	Flow control using acoustic effects	A symmetric plasma actuator generates vertical structures interacting with shear layer instabilities.
Enloe et al.(2005) [36]	Temporal density, velocity measurements near the plasma actuator	Indicated density variation slope near the electrode edge as possible reason for momentum coupling.
Baird et al.(2005)[35]	Acoustic testing of plasma actuator.	Acoustic patterns showed a characteristic coherently driven system indicating compressibility effects.
Jukes et al.(2006) [37]	Characterization of discharge-induced wall flow mechanism	The discharge actuator characteristics are investigated using hot-wire measurements in the near wall region.

In [24] a plasma array with phased inputs with unsteady flow control is investigated. Separation control on a NACA66 wing is studied by Post et al.[27] and is illustrated in Figure 5. The plasma operation significantly reduces the size of the separation bubble. In [12] the plasma generation is used as a local heating mechanism thereby inducing boundary layer separation. Rivir et al.[11] compare the piezoelectric surface flow control mechanism with the heating mechanism of Leonov et al.[12]. A summary of experimental efforts is presented in Table 2.

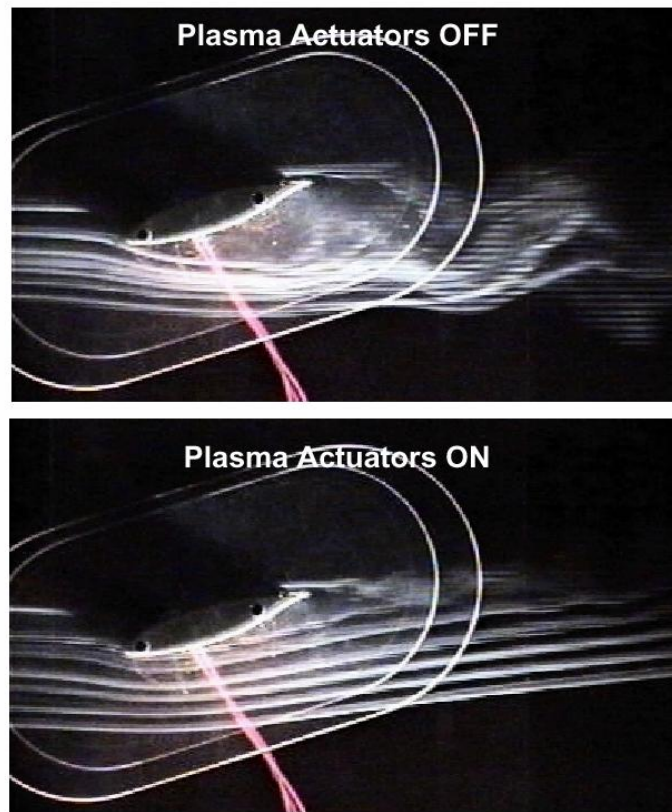


Figure 5 Separation control on a NACA66-18 wing at a $Re=79000$, 16 degrees angle of attack, reproduced from Post et al.[17]

A novel approach to apply plasma based EHD flow control to subsonic flows is being investigated by Chan [44]. The acoustic properties of low rectangular cavities are being investigated for the potential use of plasma as flow-control devices. In the

experiments, the electrodes of the plasma actuators were laid out streamwise to the flow. A symmetric electrode arrangement (where the lower electrode is wider compared to the exposed upper electrode and placed exactly below it to ensure symmetry) which can generate vortical structures is used upstream of the cavity to inhibit the feedback process in the shear layer which is key to the generation of large amplitude frequency tones. The plasma actuators were reported to attenuate completely the discrete tones produced by the cavity. The acoustic effects can act on the time-scale smaller than the fluctuating frequency.

There have also been efforts to use plasma based actuators in the context of turbulent boundary layer flow control. EHD based turbulent flow control concepts has been presented in recent articles by Soldati et al.[45-47]. As in the present effort, the electrohydrodynamic effects are modeled as a variable body force term in the equations describing fluid motion. The complex interaction between the EHD effects, wall structure of turbulence and the mean flow were studied. The EHD flows affect the turbulence field by increasing both dissipation as well as production thus maintaining the balance. However, overall drag reduction was observed with consistent decrease in the Reynolds stresses. The ionization in these cases is through electrostatic precipitators and efforts are being made to use OAUGDP in this context. Wilkinson [48] investigates the use of an oscillating surface plasma wave for turbulent drag reduction. Jukes et al.[38] looks at the turbulent boundary layer control for skin friction drag reduction using the surface plasma actuator. A summary of turbulent flow control literature relevant to the present study is tabulated in Table 3.

Table 3 Summary of turbulent flow control studies

Author and year	Work description
Soldati et al, (2001) [47]	Turbulent boundary layer control from EHD flows. Drag reduction is achieved by modifying the Reynolds stress contributions
Soldati et al, (1998) [45]	Turbulence control using large scale EHD flows
Du et al, (2002) [49]	Drag reduction in wall-bounded turbulence using a transverse traveling wave
Dhanak et al, (1999) [50]	Reducing turbulent wall friction through spanwise wall oscillations
Wilkinson (2003) [48]	Turbulent drag reduction using oscillating surface plasma 40 % drag reduction was achieved, but ineffective at frequencies < 100 Hz
Jukes et al.(2004) [38]	Turbulent boundary layer control for drag reduction.

2.2 Review of Discharge Modeling Studies

In general, the numerical modeling efforts are developed in conjunction with experimental studies to determine their fidelity. The complex physiochemical and spatiotemporal processes associated with the glow discharge plasma also make numerical modeling essential for their understanding and in modeling applications of plasma-based devices. Experimental studies as reviewed in section 2.1 were limited in their ability to reveal plasma structure and adequately explain the observed plasma dynamics and other mechanisms. Specifically, the apparently contradicting arguments for the momentum coupling based on compressibility effects proposed by Enloe et al.[35] as against the observed lack of significant bulk heating due to the plasma reported by Jukes et al.[38], highlight the necessity for a high-fidelity first principles-based numerical modeling approach. Also, most of the preliminary modeling attempts were empirical [5,22] and argumentative in nature. In order to establish a competent mechanism for the paraelectric

and other induced flow effects observed, detailed simulation of the plasma dynamics in an asymmetric electrode arrangement is necessary. In this section we will review some of the plasma and plasma actuator modeling efforts to establish the background for the present dissertation. Section 2.2.1 consists of the various phenomenological/simplified modeling approaches employed by various investigators to model the discharge-induced fluid dynamics while, in section 2.2.2 we will present some of the more high-fidelity discharge modeling studies.

2.2.1 Phenomenological Modeling of the Plasma Actuator

Most of the preliminary plasma actuator modeling efforts to study the fluid flow coupling was either simplified phenomenological approaches or models with reduced complexity. In the present dissertation we develop our own phenomenological model to study the plasma-induced fluid flows. This model involved the development of an empirical approach to calculate the time-averaged force to study the momentum coupling with the neutral fluid. The various discharge parameters were assumed spatial or temporal variations with the closure of the problem related constants requiring experimental data for validation. Our analytical-empirical model (see Chapter 4) based on a linear force distribution in the domain was later adopted by Gaitonde et al. [14] for modeling plasma-based separation control in a NACA 0015 wing section. This linearized body force model was an attractive option because of the difficulty in achieving efficient multi-dimensional and self-consistent plasma dynamics simulations coupled with the fluid dynamics.

Hall et al.[51] use a potential flow approach to model the aerodynamic effects of the plasma actuator. In particular, the actuator mechanism is modeled as a doublet (source-sink) to mimic the pumping action of the discharge on the neutral fluid.

Experimental validation was again required as a closure to determine the doublet strength. In a different approach, Orlov et al.[52], employ a lumped-element circuit model to account for the spatial and temporal variation of the discharge and mimic the plasma body force effect on the neutral fluid. While the above studies showed qualitative and reasonable qualitative correspondence with the experimental observations, they were limited in their ability to confidently predict as well as explain the observed mechanisms and the plasma-fluid interaction.

2.2.2 First Principles-Based Plasma Modeling Approaches

Most of these studies were undertaken either as part of studying dielectric barrier discharges (DBD's), between parallel plates operating in the kilohertz regime (low frequency) or the capacitively coupled radio frequency (high frequency) discharges for plasma applications with special emphasis on the plasma actuator. The knowledge of parallel plate discharge modeling is essential for gaining insight and developing a numerical model for the plasma actuator. This is divided into two subdivisions- the first one review the numerical challenges and approaches in the modeling of DBD's in general, while the latter places sole emphasis on the discharge-coupled fluid flows which are directly relevant to the present dissertation.

2.2.2.1 Review of dielectric barrier discharge (DBD) modeling studies

The modeling of low frequency (KHz) barrier discharges was attempted in the nineties, when the potential of uniform glow discharges was realized and experimental studies related to flow control and other surface processes gained momentum. In the various studies reviewed here, the focus is on parallel plate glow discharges controlled by a dielectric barrier in gases such helium, neon, argon, nitrogen and even air [53]. By low

frequency we mean a range 50Hz to a few KHz which is much smaller than the radio frequency regimes (MHz).

The modeling of glow discharges involves the consideration of mechanisms such as the reaction kinetics and plasma dynamics. With the high degree of complexity involved, the choice of model is usually simplified tailoring to the application. An overview of plasma models of varying complexity will be presented in the next chapter. The approximation chosen in different studies are mostly based on choice and convenience, resulting in each model differing slightly from the other while retaining the original qualitative behavior. One of the first numerical studies of dielectric barrier controlled discharges at atmospheric pressure was studied by Eliasson et al.[54] using a two-dimensional fluid model for the plasma. Almost all modeling studies employ a fluid model as against solving a Boltzmann equation because of the relatively easier nature of solution technique for the former. The fluid model consists of the transport equations for the charged and neutral species concentration, momentum and energy. The first three moments of the Boltzmann equation are considered for modeling purposes. The momentum and energy equations are also solved depending on the complexity of the model.

The numerical solution consists of three steps which all are interconnected. The first step is the solution of the Boltzmann equation to obtain the electron energy distribution function in the gas under investigation. This is essential, for the properties of electron transport such as mobility; diffusivity, mean energy etc vary as a function of E/N (E is electric field and N is the gas number density). The above transport properties are obtained solving a steady state Boltzmann equation under a constant field condition. This

assumption is reasonable because the characteristic time for energy equilibration under a changing electric field at atmospheric pressure is 10^{-11} s while the characteristic time for electric field fluctuation is 10^{-9} s [55]. This makes it possible to assume energy equilibration to be an instantaneous process. The solution of the Boltzmann equation for the electron energy distribution and other transport properties has been tabulated over a wide range of E/N and can be used during the next phase which is the transport module. In this second step, the transport equations of species number density, momentum and energy are solved.

The electric field E is solved from the Poisson equation

$$\nabla \cdot E = \frac{\rho}{\epsilon_0} \quad (1.5)$$

where ρ is the net charge density. Also, the charge build up on the dielectric as the discharge evolves and the external circuit should be added to the model at this stage. Discussed above is brief plasma modeling framework using fluid models. Eliasson et al, study a two dimensional model of the dielectric barrier discharge in three gases- Xenon, nitrogen and oxygen. Most modeling studies use inert gases in their studies so as to obtain stable glow discharges. Golubovskii et al, [13] use a multi-species 1-D fluid model to study the different modes of operation of a helium discharge at atmospheric pressure. The dielectric barrier discharges were seen to operate in two modes- a glow discharge mode, displaying characteristic low pressure discharge structure and a Townsend mode characterized by multiple current or discharge peaks. The formation of the various modes is governed by design parameters such as gap width, dielectric barrier thickness and applied voltage. Specifically, thin barriers and wide gaps led to a glow discharge mode and a Townsend mode was realized otherwise. Similar behavior was reported in the

experimental studies by Mangolini et al, [56]. Two-dimensional model studies were performed by Golubovskii et al., [57] Massines et al., [58] and Xu et al., [59]. All these studies included substantial plasma chemistry to account for the exact species concentrations. However, the significant aspect of these studies was it revealed significant two-dimensional structure for the discharge. Xu et al, [59] state that the radial expansion for the discharges can significantly alter the built up charge distribution on the dielectric surface. This has been observed in a number of two-dimensional studies such as Xu et al.[59] and Golubovskii et al, [60]. Mangolini et al.[56] state that the multiple pulses as seen in a Townsend mode are manifestations of the radial inhomogeneities. The radial expansion of the current pulse causes a non-uniform surface charge distribution with the next breakdown occurring at the discharge periphery. Another important modeling aspect is the consideration plasma chemistry. The treatment of plasma chemistry varies from the most complex reaction mechanisms which give rise to conservation and handling of multiple ion species, metastable atoms or molecules. The Penning ionization effect also contributes to the complex plasma chemistry. The simplest treatment of plasma chemistry is the two species model as used by Ben Gadri et al.[20] Shin et al,[61] with more complex multi species treatments by Mangolini et al.[62] Massines et al.[6,58] Tochikubo et al.[63] etc. Mangolini et al.[62] state that the metastable atoms in helium discharge contribute significantly to the pre-ionization through penning ionization mechanisms. This pre-ionization is important for the next breakdown. Handling more number of species implies higher computational cost and is usual kept at a possible minimum. The choice of boundary condition for the transport equations differs in various studies which try to approximate the species behavior in the

sheaths. Golubovskii et al.[60] discusses the nature of interaction between the charged particles and the dielectric boundary surface in the context of a homogeneous barrier discharge in nitrogen. The influence of different mechanisms of electron emission and the recombination are studied. A detailed discussion of the different numerical modeling strategies, treatment of boundary conditions etc. are presented in later chapters. A summary of the different low frequency numerical studies are tabulated in Table 4.

Table 4 Summary of low frequency plasma modeling studies

Author and year	Work description	Model
Golubovskii et al.(2003) [13]	Modeling of dielectric barrier discharges in helium at atmospheric pressure	Multi-species 1-D fluid model. Investigated various modes of barrier discharge operation
Golubovskii et al.(2004) [56]	Modeling of nitrogen	Multi-species 2-D model
Dongsoo Lee et al, (2004) [34]	Modeling of DBD's using a helium-oxygen mixture	1-D multi-species fluid model
Massines et al, (1998) [6]	DBD modeling using He-Ar mixture	1-D two-species fluid model
Massines et al, (2000) [58]	DBD modeling using He-Ar mixture	1-D multi-species model
Tochikubo et al, (1999) [63]	DBD modeling of pure Helium	1-D multi-species model
Mangolini et al, (2004) [62]	Modeling of Helium-oxygen mixture	1-D multi-Species model
Shin et al, (2003) [61]	Modeling of He-Ar mixture	0-D, 2-species model
Xu et al, (1998) [59]	Modeling of nitrogen based mixture	2-D multi species model
Eliasson et al, (1991) [54]	Modeling in Xenon	2-D multi-species model

High frequency modeling studies have been the focus of numerical model development for plasma simulations, in view of their extensive applications in material processing, plasma display panels (PDP's) etc. While the nature and physics of these RF discharges are different from what we are interested, the study of these discharges is useful for their numerical modeling. Prior to the last decade, the simulations were basically one-dimensional either with a fluid model or a particle model of the plasma. Since then, two and three-dimensional studies have been successfully presented. A

review of one-dimensional studies is presented by Govindan et al.[64]. The dominant type of plasma considered in these studies are low pressure, low-temperature and weakly ionized. High pressure glow discharges have also been modeled lately by Yuan et al.[65]. The fluid model is based on the self-consistent solution of the electron and ion continuity and momentum transfer equations coupled with the Poisson equation for solving the potential between the electrodes. Boeuf et al.[66] assume a local equilibrium between the charge particle kinetic and the electric field. This local equilibrium hypothesis serves as a closure relation in representing the actual Boltzmann equation through the continuity and the momentum transfer equations. Although, numerical modeling efforts to solve for the Boltzmann equation have been attempted [67] they are less preferred to simpler fluid models. Comparison studies have been made between the particle and fluid simulations by Nitschke et al.[68] to study the range of validity of the fluid approximation for the plasma. At higher pressures, the fluid model and the local equilibrium turn out to be pretty good approximations for the RF plasma. More detailed discussion of the above will be presented in later chapters. However, fluid models of varying complexity have been summarized in Table 5. Solution of the transport equations in the fluid models is computationally intensive because of their very stiff nature in space and time. To illustrate this we will look at the streamer propagation modeling in a DC voltage by Dhali et al.[69]. The propagation of the streamer obtained by a 2-D modeling study is shown in Figure 6. The wave-like solution and sharp gradients are characteristic of streamer propagation and also low frequency discharges. The system of equations is also highly non-linear with the modeling of multiple species transport equations along with the

Poisson equation for the electric field. The various numerical techniques used to handle these issues will be reviewed in the following chapters.

Table 5 Summary of high frequency plasma modeling studies

Author and year	Work description	Comments
Boeuf et al, (1987) [66]	2-D fluid model	2 moment equations, two specie
Nitschke et al, (1994) [68]	2-D fluid and particle model comparison	3 moment equations are used in fluid model and two species
Lymberopoulos et al, (1995) [70]	2-D fluid model for Gaseous electronic conference (GEC) reactor	Multi species plasma chemistry and three moment fluid formulation
Campbell et al, (1995) [30]	2-D fluid model for a PDP	Multi species plasma chemistry and two moment fluid equations
Boeuf et al, (1995) [31]	2-D fluid model for Gaseous electronic conference (GEC) reactor comparison with experiments	Two species plasma chemistry and three moment fluid equations
Meunier et al, (1995) [71] Veerasingham et al, (1996) [72]	1-D fluid model for PDP's	Multi species plasma chemistry and two moment fluid equations
Yuan et al, (2003) [65]	1-D fluid model for high pressure helium glow discharges	Multi species plasma chemistry and three moment fluid equations

2.2.2.2 Review of plasma actuator modeling studies

While numerical studies on discharge physics have been popular, computational modeling of the discharge actuator and its physics have been attempted only recently [14-18,29,74] in parallel with our ongoing efforts. The modeling the DBD effects in fluid flows requires realistic distributions of the species densities and their momentum in the domain which interacts with the neutral fluid by solving the plasma fluid equations. This will in turn enable us to calculate the net electric force acting on the charge species and acts as a body force on the neutral fluid. More recently, Roy et al.[15-16] proposed a

self-consistent two-dimensional DBD fluid model for helium gas with application to separation control using finite element techniques. This multi-fluid formulation to model the radio-frequency discharge in helium gas gives the spatial and temporal evolution of the charges species which is decoupled from the neutral fluid dynamics. The body force calculated from this data provides a more self-consistent way of modeling the plasma-wall jet interaction. This study employed a finite-element method and solved the various species transport equations using a globally implicit procedure where the system of charge continuity and momentum equations are assembled as part of a global matrix to solve for the solution vector. Singh et al.[17], in a related paper, present a parametric study of the different conditions in an asymmetric discharge configuration. Specifically, it was observed that the net body force production in the domain over a whole time-cycle produced a downward positive force for a typical configuration. Kumar et al.[18] study the nature of the discharge and the resulting force field in the presence of a magnetic field. Also studied is the shape effect of the electrodes in the event of a finite electrode thickness. All the above-mentioned modeling studies assume negligible electrode thickness. In the event of a finite-electrode thickness, the treatment of the dielectric-electrode edge can impact the near-wall force field. The common approach to be employed in the present study as well as in the previously mentioned modeling studies is that the plasma species and the neutral fluid are treated as a two-fluid system coupled through dynamic forces and pressure interactions. More recently, the simulation of the asymmetric electrode discharge actuator has been extended to atmospheric air chemistry instead of the Helium gas [75]. Visbal et al.[76] explored the potential of these plasma actuators in the control of turbulent and transitional separated flows by means of the

discharged-induced near wall effects. Specifically, a pulsed actuator producing an unsteady discharge was employed to highlight the role of turbulent and transition causing mechanisms in drag reduction as against a pure wall-jet momentum injection. A summary of the various modeling studies have been listed in Table 6.

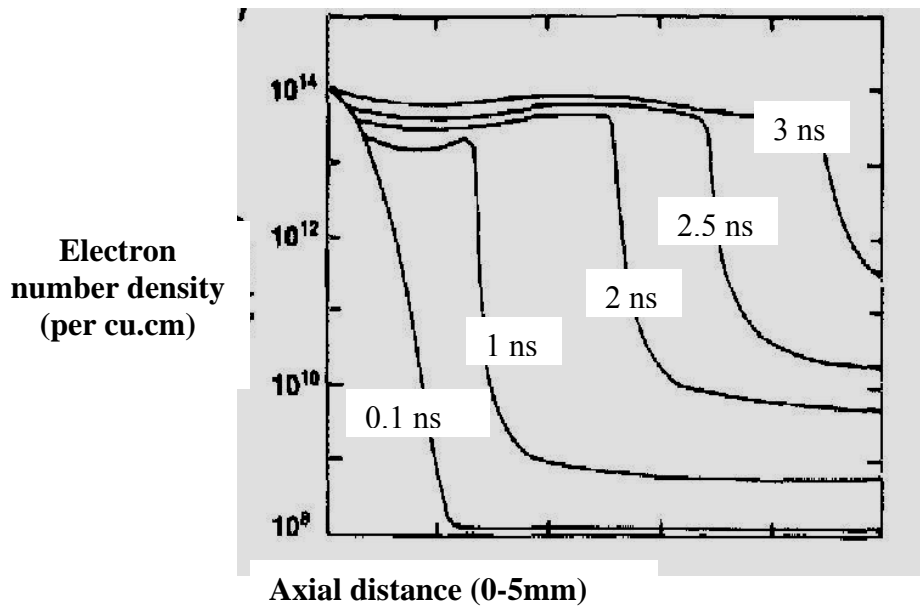


Figure 6 Streamer front propagation at different instants in a DC voltage (Dhali et al.[69])

Table 6 Summary of plasma-induced fluid flow modeling studies

Author and year	Work description	Model
Roy et al.(2005) [15-16]	Self-consistent discharge modeling using hydrodynamic plasma model.	Employed a 3-species model- ions, electrons and neutrals for Helium discharge.
Singh et al, (2005) [17]	Parametric analysis of different discharge operating parameters and geometric effects	Same as above.
Kumar et al, (2005) [18]	Discharge and fluid flow evolution in the present of a magnetic field and shape effects of the electrode edge	Same model as above.
Singh et al, (2006) [75]	Discharge modeling extended to air chemistry and the corresponding flows effects were studied.	8-species model with atmospheric air chemistry
Visbal et al, (2006) [76]	Control of transitional and turbulent separated flows using phenomenological and first principles based models.	

CHAPTER 3 NUMERICAL MODELING OF GLOW DISCHARGE PLASMA

In chapter 2 we reviewed some of the relevant experimental and numerical efforts in the modeling of the discharge actuator effects for fluid flow applications. We also highlighted some of the numerical issues arising from the multi-scale nature of the problem and how it can limit the computational capability. The presence of these large ranges of scales operating in the problem necessitates the use of modeling strategies which can range from kinetic level models to the more common hydrodynamic/fluid type models. In this chapter, we present a glimpse into some of these different modeling approaches and in the process, present an argument for the choice ‘fluid model’ used to describe the plasma dynamics in the present dissertation. In the second half of this chapter, we present in detail, the various numerical issues associated with fluid model and the presently developed solution algorithm which can efficiently handle the plasma-fluid dynamics. Lastly, a one-dimensional plasma dynamics simulation to model the discharge evolution between parallel plates is presented for validating the present capability.

3.1 Plasma Modeling Hierarchy

Modeling of glow discharge plasmas has been researched considerably more in the context high frequency (radio frequency (MHz) or KHz range) discharges than low frequency (usually smaller than KHz range) atmospheric pressure discharges. However, the studies of radio frequency (RF) discharges do provide insight for handling the stiff, multi-scale and highly non-linear plasma equations coupled with the electrostatics. The

fundamental numerical model describing the high and low-frequency discharges is essentially the same with the lone difference coming from the operating frequency of the driving voltage. While this may impact the nature of the discharge, it retains the same inherent physical characteristics in terms of length and time scales. The following discussion is equally applicable to both high and low frequency modeling studies although most of the work conducted in this dissertation focused on efficiently modeling discharge plasma actuators in the KHz regime.

Computational modeling of discharge plasmas can be achieved using a variety of approaches. In general, we can have

- a fluid treatment
- a kinetic treatment
- a hybrid scheme which combines aspects of the fluid and kinetic schemes.

In this chapter we will deal with the different types and levels of plasma modeling. The hierarchy of models based on complexity will be in three areas namely,

- type of model (fluid or kinetic etc.)
- treatment of plasma chemistry
- space complexity (1D, 2-D).

The various levels of plasma modeling are illustrated in Figure 7. The chapter is organized as follows. A brief overview of the three broad classifications of plasma models will be presented with emphasis on the fluid model which is of interest in the present work. The modeling complexity arising from plasma chemistry and spatial treatment will be discussed in the context of the fluid model.

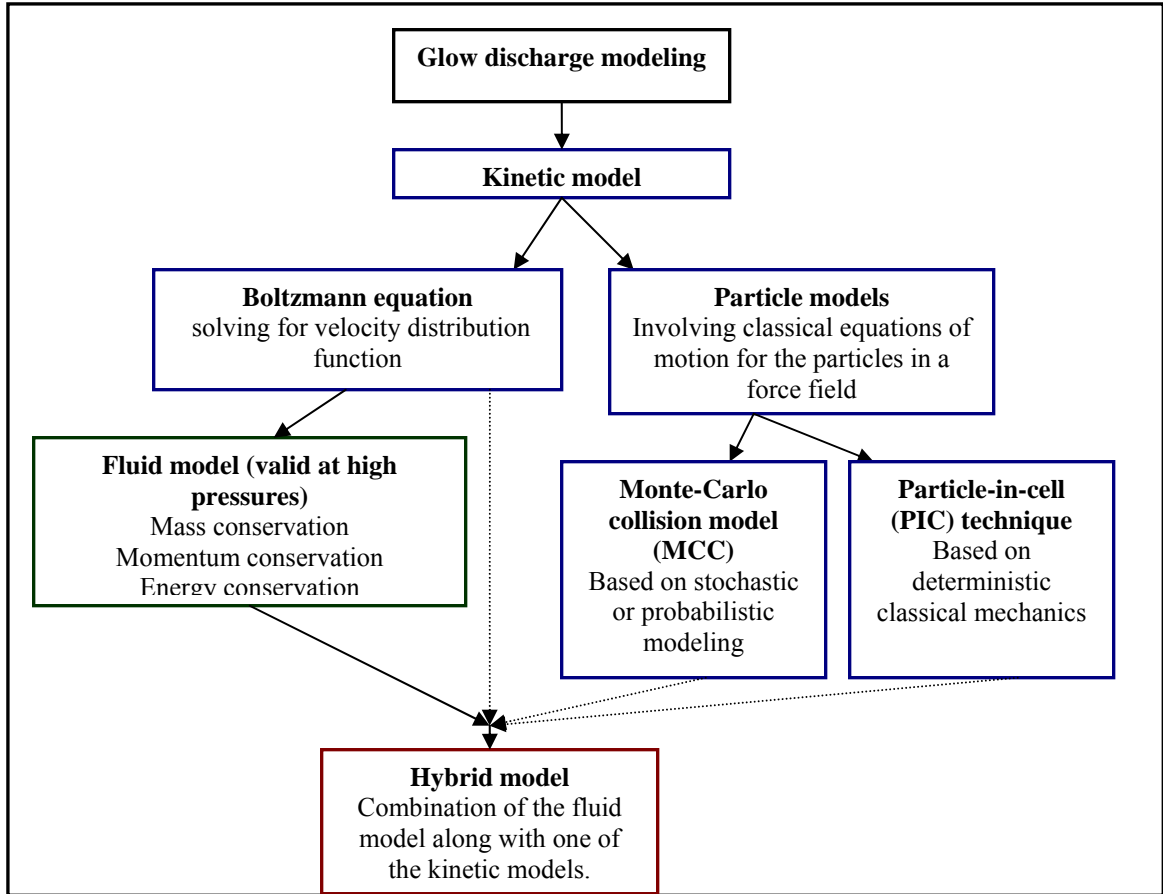


Figure 7 Levels of plasma modeling

3.1.1 Kinetic Modeling Approach

In this section we will give brief overview of the kinetic models and how they compare with the fluid model employed in this work. Kinetic models typically involve the solution of the Boltzmann equation for the species velocity or energy distribution function in both space and time or the particle simulations using techniques such as Monte Carlo methods. Although the Boltzmann equation can provide much more information than the continuum fluid models, its solution is computationally intensive requiring an order of magnitude more computer time than the fluid calculation as kinetic models are inherently higher dimensional and the solutions are functions of the velocity, space and time, the additional degrees of freedom being described in the full phase space

of the problem. For example, Riley et al.[77] use a 1D-2V formulation which implies solving for the particle velocity distribution function (VDF) in a single spatial direction and in two directions of the velocity space. This is in contrast to the fluid models where we assume an equilibrium distribution function for the species.

The coupling between the Boltzmann equation and the Maxwell's equations for electrostatics is a difficult numerical problem as the particle dynamics should include the strong body force effect of electrostatics. The solution variable in the kinetic models is the species velocity distribution function. By assuming an equilibrium distribution function in the case of fluid models, the full Boltzmann equation can be replaced by its first few moments corresponding to the conservation of mass, momentum and energy. In a continuum regime the plasma modeling starts from the Boltzmann equation [55]

$$\frac{\partial f_i}{\partial t} + c_i \cdot \nabla f_i + F_i \cdot \nabla_c (f_i / m_i) = \left(\frac{\partial f_i}{\partial t} \right)_{coll} \quad (2.1)$$

The index 'i' refers to single species. Here f is the distribution function, c the charged particle velocity, F the force, ∇ , the gradient operator in physical space, ∇_c the gradient operator in velocity space. The subscript 'coll' refers to the change of distribution due to collisions. F represents the force vector which can be the Lorentz force on the charge particles. A detailed discussion on the theory of Boltzmann equation and its relation to the fluid models for radio frequency glow discharges is presented in [55]. The index 'i' implies that (2.1) will be written for every kind of species. To enable a self-consistent solution of the above, we need to solve for the electric field E by means of the Poisson equation.

$$\nabla \cdot E = \frac{\rho}{\epsilon_0} \quad (2.2)$$

Table 7 Kinetic model studies of discharge plasmas

Author and year	Work description
Kushner [78], 1983	Monte-Carlo (MC) simulation in rf discharges.
Boswell et al.[79], 1988	Particle-in-cell (PIC) simulation of parallel plate RF discharge
Surendra et al.[80], 1991 Birdsall et al.[67], 1991	PIC-MC technique for rf parallel plate glow discharge in helium
Hitchon et al.[81], 1991	Direct numerical integration of the Boltzmann equation using BGK model for the collision term
DiCarlo et al.[82], 1989	Direct integration of the Boltzmann equation using Flux corrected transport. Direct integration Boltzmann equation using method of characteristics with a finite-difference treatment of the collision integral.
Riley et al.[77], 1994	Solution is accelerated using a time-averaged equation along with the full equation.

Another complexity in solving the Boltzmann equation (2.1) comes from the evaluation of the collision term which is the source of the non-linearity. Typically, the collision term is modeled using a particle technique such as Monte Carlo methods (DSMC- direct simulation Monte Carlo). Other methods such as the particle-in-cell (PIC) technique are also common. Kushner [78] uses a particle simulation of a radio frequency parallel plate discharge using a Monte Carlo model. Boswell et al.[79] used PIC techniques in a self-consistent simulation of parallel plate discharges. Birdsall [67] and Surendra et al.[80] study the PIC-MCC (Monte Carlo collision) technique for modeling discharges. As an improvement over the early PIC techniques to include binary collisions (due to electrostatic effects), the Monte Carlo collision model was incorporated. This is in a way, a hybrid of the PIC and the MCC techniques which existed independently. PIC/Monte Carlo models of radio frequency discharges provide kinetic information self-consistently by integrating the equations of motion of many particles

representing ion and electrons with a simultaneous solution of the Poisson equation with a Monte Carlo treatment of the electron-neutral, ion-neutral collisions. The charged particles are given an initial velocity and the position coordinates and the particle paths are followed through time using the equation of motion until a quasi-steady state condition is achieved. These simulations are then run for an extended period of time to filter out statistical fluctuations and obtain smooth profiles. The Monte-Carlo algorithm is employed to model the charge-neutral collision events following which the new position and velocity distribution is updated for the next time instant.

The PIC [67] by itself is a method based on deterministic classical mechanics of particles with prescribed force fields. In PIC, the simulation region is divided into a number of cells and the resulting grid is used in the solution of a force field from which the force on each particle inside the cell can be determined. The equation of motion of each particle is integrated to get the new position and velocity. On the other hand, Monte-Carlo simulation is a statistical technique which is basically probabilistic in nature and the particle velocities are obtained by directly integrating the equations of motion. The key steps of a integrated particle-in-cell and Monte-Carlo technique (PIC-MC) of Nitschke et al.[68] are the following:

- a. Particle position and velocities are updated each time step using the equation of motion.
- b. Particles which have crossed the system boundaries are accounted for.
- c. Monte-Carlo algorithm to determine probable collisions and the resulting states
- d. New particle positions are linearly interpolated to the nearest grid point to obtain ion and electron spatial density profiles. Poisson's equation (Eq. (2.2)) is

calculated again to determine the electric field to be used in the force term in step a.

Other solution methods for kinetic models include direct solution of Boltzmann equation as in Hitchon et al.[81] where the equation is directly integrated numerically as a partial differential equation. Here the collision term is approximated by a BGK type model (apart from Monte Carlo collision models). Because of the strong convective nature of the equation, higher order oscillation preventing schemes such as Flux Corrected Transport (FCT) (DiCarlo et al.[82]) or the “convective scheme” of Hitchon et al.[82] are employed. The direct solution of the Boltzmann equation is slowed down by the very small time resolution dictated by electron and collision relaxation times. This problem is overcome by Riley et al.[77] using a hybrid formulation which employs a time-averaged description. Here the Boltzmann equation is solved for only a few cycles at a time. The information obtained from the Boltzmann equation solution is used to solve a set of time averaged equations describing the heavy species. The averaged equations are solved for thousands of RF cycles and then the Boltzmann equation is solved again and this process is repeated. This is in a way another type of hybrid approach. Another technique along similar lines where the faster varying scales are solved a few times and the information is used to model the slowly varying processes is used by Highton et al.[81]. This scale up technique accelerates the solution process significantly. Other hybrid models will be presented next. The various kinetic studies are summarized in Table 7.

3.1.2 Hybrid Modeling Approach

The computationally intensive kinetic simulations (as compared to fluid models) are more accurate in the sense that they can be used to model low-pressure (typically $< 100\text{mTorr}$ [68]) or highly non-equilibrium situations for which fluid models are highly suspect. The

hybrid models are typically employed when there is a need to preserve the accuracy and capability of the kinetic schemes and at the same time reducing the computational burden.

Table 8 Summary of hybrid modeling studies

Author and year	Hybrid model
Belenguer et al.[84]	'Bulk-beam' model where the bulk and high speed or beam electrons are treated as fluid and particle species respectively.
Surendra et al.[80] 1990	'Bulk-beam' model
Fiala et al.[85] 1994	Fluid model with Monte-Carlo simulation for the ionization term.

Hybrid models have been studied which combine aspects of both fluid as well kinetic models and thereby achieve a balance between accuracy and efficiency. The charge species in low-pressure discharges are generally not at local thermodynamic equilibrium and one cannot assume in general that these species attain a thermodynamic temperature. This lack of thermodynamic equilibrium complicates the modeling of discharges, since the kinetic models determine the species velocity distribution function as against an assumed distribution function in the case of fluid models. From another perspective, under low pressures the thermal flux is comparable to the drift flux from the electric field and as a result the isotropic behavior for macroscopic properties such as pressure is lost. The kinetic models in such non-equilibrium cases give accurate results as compared to fluid models. One type of hybrid model treats the fast or high energy electrons called as 'beam' electrons as particles and the slow electrons or 'bulk' and ions as fluid and achieves a self-consistent simulation of the entire discharge while addressing the non-equilibrium nature of the high energy electrons. Such a model has been first introduced by Belenguer et al.[84] and used by Surendra et al.[80]. Another type of hybrid procedure is used by Fiala et al.[85] where

the ionization source term is re-calculated by a Monte Carlo simulation after a few hundred time-steps of the fluid equations.

3.1.3 Fluid Modeling Approach

Fluid models generally consist of a few moments of the Boltzmann equation for the various species with an assumed distribution function. However, as discussed previously, the validity of the fluid type description of the plasma is determined by the existence of a local thermodynamic equilibrium. This issue is significant while modeling low-pressure discharges. Nitschke et al.[68] compare the particle-in-cell model with a fluid model simulation of a radio frequency discharge in helium. The results from the two models were compared over a wide range of applied voltages and pressures. Considerable agreement between the studies was observed for pressures greater than 100 mTorr [68,55], which is much smaller than the atmospheric pressure regime of 760 Torr. As a result most of the atmospheric pressure discharge simulations use fluid models which are potentially attractive for computational studies if the limitations to their validity are adequately addressed. In this dissertation, we are interested in the modeling of discharge processes at atmospheric pressures.

Fluid models usually consist of the first three moments of the Boltzmann equation which includes the species continuity, momentum and energy conservation equations. The fluid species usually consist of the ions, electrons and neutral species. The number of species is typically dependent on the extent of plasma chemistry included in the model. A typical fluid description of the model as used by Colella et al.[86] is presented below.

Species continuity equation:

$$\frac{\partial n_i}{\partial t} + \nabla \cdot (n_i u_i) = \sum_j R_{ij} \quad (2.3)$$

Species momentum equation:

$$\frac{\partial(m_i n_i u_i)}{\partial t} + \nabla \cdot (m_i n_i u_i u_i) + \bar{\nabla} \cdot (n_i k T_i) = q_i n_i E - \sum_j \frac{m_i m_j}{m_i + m_j} n_i v_{ij} (u_i - u_j) + \sum_{j|R_j < 0} m_i u_i R_{ij} + \sum_{j|R_j > 0} m_i u_i R_{ij} \quad (2.4)$$

This is a generalized form of the momentum equation incorporating various phenomena.

The third term on the left hand side represents the partial pressure gradient of the i^{th} species. The right side includes all source terms- the Lorentz force, momentum loss from collision and momentum losses from production and destruction, in that order.

Species energy equation:

$$\begin{aligned} & \frac{\partial}{\partial t} \left[n_i \left(\frac{1}{2} m_i u_i \cdot u_i + \varepsilon_i \right) \right] + \nabla \cdot \left[n_i \left(\frac{1}{2} m_i u_i \cdot u_i + \varepsilon_i \right) u_i \right] + \nabla \cdot (n_i k T_i u_i) = q_i n_i u_i \cdot E - \\ & \sum_j \frac{2m_i m_j}{(m_i + m_j)^2} n_i v_{ij} \left[\frac{1}{2} (m_i u_i \cdot u_i - m_j u_j \cdot u_j + (m_j - m_i) u_i \cdot u_j) + \varepsilon_i - \varepsilon_j \right] \quad (2.5) \\ & + \sum_{j|R_j < 0} \left(\frac{1}{2} m_i u_i \cdot u_i + \varepsilon_i \right) R_{ij} + \sum_{j|R_j > 0} \left(\frac{1}{2} m_j u_j \cdot u_j + \varepsilon_j \right) R_{ij} + \sum_j \varepsilon_{ij} S_{ij} \end{aligned}$$

where $\varepsilon_i = \frac{kT_i}{\gamma_i - 1}$. Here the summation notation denotes the summation over the different

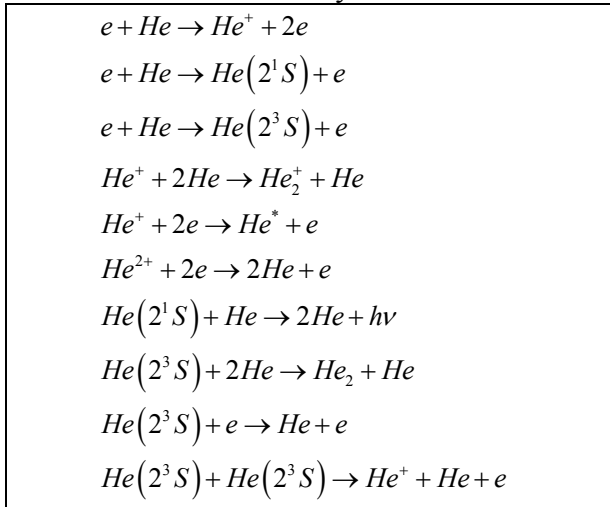
kind of species. In assuming a fluid model, each plasma component (index 'j') is assumed to have a near Maxwellian distribution. The infinite set of moment equations is truncated to include just the moments corresponding to the conservation of mass, momentum and energy for each component. The indices 'i' and 'j' represents the particular species and its complementary ones, respectively. The summation notation indicates summation over all particle species which includes electrons, ions and neutral species.

These transport equations are solved in conjunction with the Maxwell's equations for the electric potential which is written as

$$\Delta\phi = \frac{1}{\varepsilon_0} \left(\sum_i q_i n_i \right) \text{ and } E = -\nabla\phi. \quad (2.6)$$

The number of equations that are solved in the system is determined by the number of species considered in the plasma chemistry and can result in a hugely coupled system. However in reality, the number of equations actually solved is very manageable with the various approximations to the model and the system of equations. One of the common assumptions [20] is approximating the plasma chemistry to include just a single species of positive ion and negative ion or electron. Also, in many cases, the neutral species are not considered because of their lack of contribution to the net charge. However there exists non-charged species such as metastables whose dynamics can differ from those of the neutral species. Such species are usually considered when the complex plasma chemistry is important for the modeling study. This is illustrated below in the context of a helium atmospheric pressure glow discharge where a model with complex set of equations, as given in Tochikubo et al.[63].

Table 9 Plasma chemistry considered in a helium discharge



Source : Tochikubo et al. [63]

The plasma chemistry shown in Table 9 needs to be modeled taking into account the reaction rates to account for the species concentrations and transport. Predominantly, modeling studies are one-dimensional (see Table 4), followed by two-dimensional studies which are less frequent, while three dimensional studies are rare. It should be noted that distinct higher dimensional effects have been observed in studies by Mangolini et al.[62,56]. The fluid modeling studies have already been summarized in Table 4 and Table 5 Comparison of the results of different numerical models for the same set of modeling parameters has been compiled by Surendra [87] for a 1-D RF discharge simulation. The results indicate that fluid models, although less reliable than kinetic models, give reasonably accurate predictions of discharge properties for sufficiently high pressure. Also, the kinetic models, say PIC-MC, compare well with the hybrid models. The fluid models are generally reported to show greater variation than kinetic/hybrid schemes. Since we are interested in the discharge operating at atmospheric pressure, we will focus on the study of fluid models for this dissertation.

3.2 Numerical Modeling of Glow Discharge Plasmas

In this section, we will present the detailed numerical modeling framework for the atmospheric pressure glow discharge plasma. The plasma-fluid-Maxwell equations presented in the previous chapter represent the generalized set of equations. In reality, however, the set of equations solved are much different and less complex from the ones presented, after the various problem specific modeling approximations applied to the system. In this section, we will first discuss the various approximations that can be used from which we can arrive at the final set of equations to be solved. Following this, the numerical nature of these equations will be discussed to highlight the difficulties that will

be encountered during its solution and the techniques to handle them. Finally a solution algorithm will be developed to handle the system of intricately coupled equations.

3.2.1 Plasma Discharge Governing Equations

The fluid model for the plasma can be described by the following equations which describe the first three moments of the Boltzmann equation for the various species. They are the continuity, momentum and energy equations. The plasma is considered as a multi-component fluid comprised of two types of primary species, namely, ions and electrons. A generalized description of the plasma model was presented in section 3.1.3 (Eqs. (2.3)-(2.6)). The various modeling studies use a variety of approximations to simplify the system of equations. In the following section, we will present the commonly used versions and highlight the specific variants used in different studies.

We will describe the composition of the fluid by means of electrons and ions. By ions we imply all charged species which have a mass comparable with the neutral particles. As seen in the previous chapter, the uncharged metastable species also play a significant role in the plasma chemistry. But we shall neglect them in favor of the present focus towards developing an efficient modeling strategy for these plasma fluid equations. Now, we will briefly develop the form of the fluid equations to be used. The continuity equations for the positive ion and electron species are given by

$$\frac{\partial n_e}{\partial t} + \nabla \cdot (n_e v_e) = R_{c,e} - R_{d,e} \quad (2.7)$$

$$\frac{\partial n_i}{\partial t} + \nabla \cdot (n_i v_i) = R_{c,i} - R_{d,i} \quad (2.8)$$

The subscripts e and i stand for electrons and positive ions, respectively. The parameter R_c is the ionization or creation term and R_d , the recombination or destruction term. With no loss of generality, we can have a similar equation for negative ions. The

terms on the right hand sides of eq. (2.7)-(2.8) represents the production from ionization and the loss from destruction, in that order. These two terms are obtained from the collision terms in the actual Boltzmann equation(2.1). The exact forms of these terms are obtained from the type closure model one uses to represent the particle phenomena at the fluid model. This can be done in a variety of ways as mentioned in [55] such as assuming a velocity distribution function (Maxwellian) or by assuming phenomenological expressions for the collision terms. The general form of the source terms is given as

$$\begin{aligned} R_c &= n\nu_c \\ R_d &= n\nu_d \end{aligned} \quad (2.9)$$

where ν_c and ν_d are the creation and destruction frequency which are function of known parameters such number density $n_{i,e}$, velocity $u_{i,e}$ etc. The species velocities are given by u_i and u_e for the ions and electrons respectively. These velocities are obtained from the momentum equations given below. The generalized momentum equation is given in(2.4).

It can be written simply as

$$\frac{\partial}{\partial t}(n_e m_e v_e) + \nabla \cdot (n_e m_e v_e v_e) = -\nabla p_e + n_e m_e q_e E - R_{me} \quad (2.10)$$

$$\frac{\partial}{\partial t}(n_i m_i v_i) + \nabla \cdot (n_i m_i v_i v_i) = -\nabla p_i + n_i m_i q_i E - R_{mi} \quad (2.11)$$

where $R_{mi,me}$ represents the collisional momentum loss of the i^{th} species or electron and $P_{i,e}$ is the partial pressure which can otherwise be written as $n_{i,e}kT_{i,e}$. k is the Boltzmann constant, $T_{i,e}$ is the species temperature and m_i is the species mass. This form of expression for the pressure tensor assumes isotropic behavior and is strictly valid only for a Maxwellian distribution. The momentum loss $R_{mi,me}$ is usually written as

$$R_{me} = m_e n_e \nu_e v_{me} \quad (2.12)$$

$$R_{mi} = m_i n_i \nu_i \mathbf{v}_{mi} \quad (2.13)$$

where $\nu_{mi,me}$ is the frequency of collisions which result in momentum transfer. The second term on the right hand side represents the body force from the electric field with $q_{i,e}$ being the species charge. Combining (2.7)-(2.8) and (2.9) we have

$$\frac{\partial n_e}{\partial t} + \nabla \cdot (n_e \mathbf{v}_e) = \nu_{c,e} n_e - \nu_{d,e} n_e \quad (2.14)$$

$$\frac{\partial n_i}{\partial t} + \nabla \cdot (n_i \mathbf{v}_i) = \nu_{c,i} n_i - \nu_{d,i} n_i \quad (2.15)$$

and substituting (2.12)-(2.13) into (2.10)-(2.11) we have

$$\frac{\partial}{\partial t} (n_e m_e \mathbf{v}_e) + \nabla \cdot (n_e m_e \mathbf{v}_e \mathbf{v}_e) = -\nabla (n_e k T_e) + n_e q_e E - m_e n_e \nu_e \mathbf{v}_e \quad (2.16)$$

$$\frac{\partial}{\partial t} (n_i m_i \mathbf{v}_i) + \nabla \cdot (n_i m_i \mathbf{v}_i \mathbf{v}_i) = -\nabla (n_i k T_i) + n_i q_i E - m_i n_i \nu_i \mathbf{v}_i \quad (2.17)$$

Now we will simplify the momentum equation (2.16)-(2.17) using (2.14)-(2.15), to yield.

$$\begin{aligned} n_e m_e \frac{\partial \mathbf{v}_e}{\partial t} + n_e m_e (\mathbf{v}_e \cdot \nabla) \mathbf{v}_e + n_e m_e \nu_e (\mathbf{v}_{c,e} - \mathbf{v}_{d,e}) + \\ \nabla (n_e k T_e) - n_e q_e E = -n_e m_e \nu_e \mathbf{v}_{me} \end{aligned} \quad (2.18)$$

$$\begin{aligned} n_i m_i \frac{\partial \mathbf{v}_i}{\partial t} + n_i m_i (\mathbf{v}_i \cdot \nabla) \mathbf{v}_i + n_i m_i \nu_i (\mathbf{v}_{c,i} - \mathbf{v}_{d,i}) + \\ \nabla (n_i k T_i) - n_i q_i E = -n_i m_i \nu_i \mathbf{v}_{mi} \end{aligned} \quad (2.19)$$

or

$$\frac{1}{\nu_{me}} \frac{\partial \mathbf{v}_e}{\partial t} + (\mathbf{v}_e \cdot \nabla) \frac{\mathbf{v}_e}{\nu_{me}} + \frac{\mathbf{v}_e}{\nu_{me}} (\nu_{c,e} - \nu_{d,e}) + \frac{\nabla (n_e k T_e)}{n_e m_e \nu_{me}} - \frac{q_e E}{m_e \nu_{me}} = -\mathbf{v}_e \quad (2.20)$$

$$\frac{1}{\nu_{mi}} \frac{\partial \mathbf{v}_i}{\partial t} + (\mathbf{v}_i \cdot \nabla) \frac{\mathbf{v}_i}{\nu_{mi}} + \frac{\mathbf{v}_i}{\nu_{mi}} (\nu_{c,i} - \nu_{d,i}) + \frac{\nabla (n_i k T_i)}{n_i m_i \nu_{mi}} - \frac{q_i E}{m_i \nu_{mi}} = -\mathbf{v}_i \quad (2.21)$$

where time derivative is a substantial derivative. Now we try to simplify the momentum equation using a scaling argument. The first term in (2.20)-(2.21), which is the local derivative scales, as the velocity times the ratio of the driving voltage frequency and the collision frequency. This ratio is usually very small even for driving voltages in the megahertz range as the collision frequency is of the order of a few gigahertz.

$$\frac{1}{v_{mi,me}} \frac{\partial v_{i,e}}{\partial t} \sim O\left(\frac{\omega v_{i,e}}{v_{mi,me}}\right) \quad (2.22)$$

Hence the local derivative can be neglected. For the convection term, momentum loss collision frequency $v_{mi,me}$ scales as the ratio of the thermal velocity and the mean free path.

$$(v_{e,i} \cdot \nabla) \frac{v_{e,i}}{v_{me,mi}} \sim O\left(v_{i,e} \frac{v_{i,e}}{L} \frac{\lambda}{v_T}\right) \quad (2.23)$$

As long as the thermal velocity is comparable to the species drift velocity ($\frac{v_{i,e}}{v_T} \leq 1$) and

we are in the continuum regime ($\frac{\lambda}{L} = Kn \ll 1$), the convection term will be very small

compared to the right hand side (force and collision loss terms). However, for the heavier ions the thermal velocity is comparable to the drift velocity at very low pressures and hence the inertial terms become significant. Hence, at low pressures the distribution function departs significantly from the Maxwellian or equilibrium distribution function.

This makes the diffusivity and pressure tensors anisotropic. But at higher pressures, the above simplification is not too costly and the ion momentum equation has the same form as the electron momentum equation. The third term on the left hand side of (2.20)-(2.21) is the ratio of the creation or destruction frequency and the momentum loss collision

frequency. It is usually expected that the collision processes are more frequent when compared to one which causes ionization and the ratio is negligible. The final simplified form of the momentum equation can be written as

$$\frac{\nabla(n_e k T_e)}{n_e m_e \nu_{me}} - \frac{q_e E}{m_e \nu_{me}} = -v_e. \quad (2.24)$$

$$\frac{\nabla(n_i k T_i)}{n_i m_i \nu_{mi}} - \frac{q_i E}{m_i \nu_{mi}} = -v_i \quad (2.25)$$

Now let us define the species mobility $\mu_{i,e}$ and the diffusivity $D_{i,e}$ as

$$\mu_{i,e} = \frac{q_{i,e}}{m_{i,e} \nu_{mi,me}} \quad (2.26)$$

$$D_{i,e} = \frac{k T_{i,e}}{m_{i,e} \nu_{mi,me}} \quad (2.27)$$

The final form of the momentum equation becomes

$$\frac{\nabla(n_e D_e)}{n_e} - \mu_e E = -v_e \quad (2.28)$$

$$\frac{\nabla(n_i D_i)}{n_i} - \mu_i E = -v_i \quad (2.29)$$

This form of the momentum equation is called as the drift-diffusion approximation.

Further variants of this form have been used in many studies such as by Boeuf et al.[31] etc., and is shown below.

$$\frac{D_e \nabla(n_e)}{n_e} - \mu_e E = -v_e \quad (2.30)$$

$$\frac{D_i \nabla(n_i)}{n_i} - \mu_i E = -v_i \quad (2.31)$$

Now we will briefly derive the simplified form of the energy equation. The general energy equation can be written as

$$\frac{\partial(n_e \varepsilon_e)}{\partial t} + \nabla \cdot (n_e v_e \varepsilon_e + v_e P_e + Q_e) - n_e q_e E \cdot v_e = R_{en} \quad (2.32)$$

where ε is the particle energy, P_e the electron pressure, Q_e the heat conduction and R_{en} the energy loss from collisions etc. As before, assuming a Maxwellian distribution for the velocity, we have

$$P_e = n_e k T_e = \frac{2}{3} n \varepsilon_{T,e} \quad (2.33)$$

and

$$Q_e = -K_e \nabla T_e = -\frac{2}{3} K_e \nabla \left(\frac{\varepsilon_{T,e}}{k} \right) \quad (2.34)$$

Here ε_T is the thermal energy component. The thermal conductivity K_e can be written in terms of the diffusion coefficient D_e , from kinetic theory results as

$$K_e = \frac{3n_e D_e k}{2} \quad (2.35)$$

The fact that all the parameters such as conductivity, diffusivity are written as scalars is because we assume isotropy. Substituting (2.33), (2.34) and (2.35) into (2.32) we get the complete energy equation as

$$\frac{\partial(n_e \varepsilon_e)}{\partial t} + \nabla \cdot \left(n_e v_e \varepsilon_e + \frac{2}{3} n_e v_e \varepsilon_e - n_e D_e \nabla (\varepsilon_{T,e}) \right) - n_e q_e E \cdot v_e = R_{en} \quad (2.36)$$

The form of the energy loss rate R_{en} as well as the parameters $R_{mi,me}$, R_c , R_d , the mobility and diffusivity etc, needs to be identified to close the system. These parameters are usually related to some measurable macroscopic properties. Boeuf et al.[31] and Gogolides et al.[55] among others assume that the above energy loss rates etc., depend on

the mean electron energy as they do under equilibrium conditions when the electron energy gain is locally balanced by the losses. If we assume the following form for R_{en} [31, 55]

$$R_{en} = K_L (E/N) N n_e = \nu_L n_e \quad (2.37)$$

then the energy equation under equilibrium conditions yields

$$K_L = -\frac{q_e \nu_e E}{N} \quad (2.38)$$

At equilibrium, all the mean electron properties such as ϵ_e , D_e and μ_e etc. can be assumed to be a function of E/N . This dependence of the mean electron properties on the local electric field as against the velocity distribution function (in the Boltzmann equation) is called as the local field approximation. This approximation rules out any non-local effects for these properties. The values of the electron properties are the same as that obtained in a uniform electric field condition, where the collision term balances the force term. Detailed discussions are presented in [66,64,72,55] Hence, from (2.38), R_{en} is also a function of E/N . A similar form is used for other parameters such as $R_{mi,me}$, R_c , R_d . The equilibrium dependencies of the various parameters on the ratio E/N are tabulated by solving a Boltzmann equation or a Monte Carlo code under the appropriate conditions. It should be noted that in some hybrid approaches (e.g. Kushner and co-workers [88-89]), the fluid energy equation is dropped and the kinetic energy equation is solved using a 2-D Monte Carlo method.

The ion energy seems to have little effect on the ionization and attachment rates and hence is not solved unless required. To summarize, the electron inertial terms are insignificant considering their negligible mass. Hence, the momentum balance reduces to the drift diffusion form. For the ions, the inertial term is significant at low pressures (<

100 mTorr [55]) and is included in some studies. At high pressures, however, a drift-diffusion approximation is considered reasonable [31,55]. A summary of conservation equations for the mass, momentum and energy used to model high frequency glow discharges is given below. A similar set of equations is presented by Gogolides [55].

Continuity equation:

$$\text{Electrons: } \frac{\partial n_e}{\partial t} + \nabla \cdot (n_e v_e) = K_{c,e}(E/N) N n_e - K_{d,e}(E/N) N n_e \quad (2.39)$$

$$\text{Ions: } \frac{\partial n_i}{\partial t} + \nabla \cdot (n_i v_i) = K_{c,i}(E/N) N n_i - K_{d,i}(E/N) N n_i \quad (2.40)$$

Momentum equation:

$$\text{Electrons: } n_e \mu_e E - \nabla (n_e D_e) = n_e v_e \quad (2.41)$$

$$\text{Ions: } n_i \mu_i E - \nabla (n_i D_i) = n_i v_i \quad (\text{for high pressure discharges}) \quad (2.42)$$

$$\begin{aligned} n_i m_i \frac{\partial v_i}{\partial t} + n_i m_i (v_i \cdot \nabla) v_i + n_i m_i v_i N (K_{c,i} - K_{d,i}) \\ + \nabla (n_i k T_i) - n_i q_i E = -n_i m_i v_i N K_{mi} \end{aligned} \quad (2.43)$$

(for low pressure discharges)

Energy equation:

$$\begin{aligned} \text{Electrons: } \frac{\partial (n_e \mathcal{E}_e)}{\partial t} + \nabla \cdot \left(n_e v_e \mathcal{E}_e + \frac{2}{3} n_e v_e \mathcal{E}_e - n_e D_e \nabla (\mathcal{E}_{T,e}) \right) \\ - n_e q_e E \cdot v_e = K_L (E/N) N n_e \end{aligned} \quad (2.44)$$

Ions: No energy equation is considered as ion energies do not affect ionization processes.

To summarize, the various assumptions made in the development of the fluid equations are:

1. the pressure tensor is isotropic
2. the drift energy is comparable to the thermal energy

3. heat flux is proportional to the electron temperature gradient
4. the mean electron-neutral collision rates depend only on the electron mean energy.

Most of the numerical modeling studies of high frequency glow discharges use whole or part of the above system of equations along with the Poisson equation for the electric field which is written as.

$$\nabla \cdot E = \frac{e}{\epsilon_0} (\sum n_i - n_e) \quad (2.45)$$

The values of the parameters K , mobility, diffusivity etc. are either obtained by solving the spatially homogeneous Boltzmann equation, or assigned curve fitted expressions from experimental data or a combination of both. A standard model for the ionization coefficient is the Townsend expression presented in [61] which is shown below.

$$K_i = \frac{\mu_e E p}{N} (34) e^{\left(\frac{E}{p}\right)^{-16}} \quad (2.46)$$

Here p is the pressure. Some of the numerical issues associated with the system of equations discussed above are as follows. The set of moment equations described above are intricately coupled and strongly non-linear with a wide range of spatial and temporal scales. The solution profiles for the charge particle densities contain steep unsteady gradients especially in the sheaths. The resolution of these sharp gradients accurately requires well refined grids leading to time-intensive computations. Sharply varying production terms such as ionization processes result in stiff source terms which also limit the time step. For these reasons, 3-D and to a lesser extent 2-D modeling studies are less frequently attempted. The continuity equation for the ions and electrons are essentially inhomogeneous Euler equations (as diffusion is mostly small compared to drift) of gas

dynamics augmented with the electrostatic force, collisional and source/sink terms. Solution of this system poses challenges due to its multi-time-scale nature which we will illustrate now. The critical time scales in the problem are listed below.

1. The discharge operating frequency
2. The ion drift
3. The non-linear source term- ionization, collision etc.
4. The electron drift
5. The dielectric relaxation time

The discharge operating frequency time scale is given by

$$\tau_{\omega} = \frac{1}{\omega} \quad (2.47)$$

where ω is the driving frequency. In order to illustrate the time scales we will use the 1-D modeling result from Lee et al.[34] which is shown in Figure 3. The driving voltage is 1.5KV with a frequency of 10 KHz. It can be seen from the figure that the appropriate length scale for the problem would be the size of some physical length such as the positive column or the cathode fall (Figure 3) which is 0.05 cm in a 0.3 cm gap. The drift velocity from the drift-diffusion approximation is μE . The values of the mobility for the helium ions and electrons can be obtained from literature and the electric field value is the peak value in the positive column (~ 20 KV/cm). Then the drift time scales for the ions and electrons can be calculated as the ratio of the width of the positive column and the drift velocities.

$$\tau_{dr,ion} = \frac{l_{dr}}{\mu_{ion} E} \quad (2.48)$$

$$\tau_{dr,elec} = \frac{l_{dr}}{\mu_{elec}E} \quad (2.49)$$

To evaluate the source term time scale, we will use the Townsend formula for calculating the ionization coefficient. From (2.9) the ionization term R_c can be written in terms of the ionization frequency ν_c . From (2.37) and (2.46) we can see that ν_c is of the form

$$\nu_c = \mu_e E p (34) e^{\left(\frac{E}{p}\right)^{0.4}} = \frac{1}{\tau_c} \quad (2.50)$$

which gives the ionization time scale τ_c as the reciprocal of the frequency. We use the above form of the ionization frequency in calculating the timescale in Table 10. Now we shall describe the origin of the dielectric relaxation time scale and evaluate it. This timescale represents the relaxation of the electric field in the medium to adjust to the change in the charge density and is usually the most stringent of all the time-step limitations.

Taking the time derivative of the Poisson equation(2.45), we get

$$\frac{\partial}{\partial t}(\nabla \cdot E) = \frac{e}{\epsilon_0} \left(\frac{\partial n_i}{\partial t} - \frac{\partial n_e}{\partial t} \right). \quad (2.51)$$

Now substitute for right hand side from the continuity equations (2.39)-(2.40), which gives

$$\nabla \cdot \left(\frac{\partial E}{\partial t} \right) = \frac{e}{\epsilon_0} \nabla \cdot (n_e v_e - n_i v_i) \quad (2.52)$$

Getting rid of the divergence operator, we get

$$\frac{\partial E}{\partial t} = \frac{e}{\epsilon_0} (n_e v_e - n_i v_i) + C \quad (2.53)$$

Substituting for the velocities using the drift diffusion approximation (2.28) yields

$$\frac{\partial E}{\partial t} = \frac{e}{\epsilon_0} (\mu_e n_e E - \mu_i n_i E + D_i \nabla n_i - D_e \nabla n_e) + C \quad (2.54)$$

Eq. (2.54) can be viewed as the evolution of the electric field due to the space charge and leads to a time scale as

$$\tau_{diel} = \frac{\epsilon_0}{e(|\mu_e| n_e + |\mu_i| n_i)}. \quad (2.55)$$

This restriction is highly severe and is usually overcome by a semi-implicit solution of (2.54). In other words the above restriction can be viewed as the CFL condition for the current continuity equation. Using the values of the various parameters from the 1-D model of Lee et al.[34], the magnitudes of the various time scales are calculated and tabulated in Table 10. The dielectric relaxation time becomes real small as the number density increases which is the case for high frequency (MHz) discharges and hence needs to be treated accordingly. As can be seen from Table 10, time scales involved in the problem vary over a wide range and this needs to be taken into account while developing a numerical algorithm. If we take into account adequate grid resolution in the sheath regions, this time scale will be further reduced.

3.2.2 Numerical Algorithm

Modeling of plasma fluid equations has been extensively attempted in the last decade or so predominantly for 1-D applications and occasionally 2-D applications. Emphasis was placed on plasma chemistry [89] and studying the limitations of the model by comparison with experiments or kinetic theory based models [68,31,67,80]. Efforts to develop efficient solution algorithms for such systems such as Boeuf et al.[31] Hammond et al.[90] Golubovskii et al.[56] Colella et al.[86] etc. will be discussed in the following

section. These are representative studies and a more comprehensive review has been presented in the previous chapter 2. Except for Golubovskii et al. where an atmospheric pressure glow discharge between two parallel plates is studied, all other efforts are devoted to low pressure high frequency discharges. The set of governing equations employed by the various efforts differ from each and are summarized in Table 11. While the equations have the same form as given in (2.39)-(2.44) the methods of evaluating parameters such as the mobility, ionization etc. may differ from each other. It may be recalled that the two forms of the momentum equations ((2.42) and (2.43)) which include a fully approximated drift-diffusion form and the full transport equation. Both these forms are used in the modeling studies, but the simpler drift-diffusion form is preferred and valid at high pressures for ions. It is generally always used for electrons because of its light mass causing negligible inertial effects.

Table 10 Representative time scales of various processes in a 1-D helium discharge model operating at 10KHz, 1.5KV rms, calculated based on values of parameters.

Time scale	Value (s)
Operating frequency timescale, τ_w (2.47)	1e-4
Ion drift $\tau_{dr,ion}$ (2.48)	2.5e-7
Electron drift $\tau_{dr,electron}$ (2.49)	2.5e-9
Dielectric relaxation τ_{diel} (2.55)	2e-9
Ionization timescale τ_c (2.50)	1.4e-10

Note: Calculate based on parameters taken from Lee et al.[34]

It can also be seen from Table 11 that the electron energy equation is not solved for high pressure simulations (Lee et al.[34], Massines et al.[6]) when the local field approximation is valid. Not solving for the energy equation, however, prevents us from understanding the energetics such as collisional heating or Joule heating. While, the choice of governing equations and their approximations vary from one study to the other,

the numerical characteristics remain fundamentally the same. The governing equations are essentially the inhomogeneous Euler equations of gas dynamics augmented with electrostatic forces, collisional and source/sink terms. The system of equations represents multiple time scales (Table 10) and widely separated spatial scales. The spatial scales can be adequately resolved by using local grid refinement techniques [116] in the regions of sharp gradients coupled with higher order discretization methods which have been successfully applied for modeling neutral fluid flows.

Table 11 Summary of governing equations used in different studies

Author, year	Topic	Governing equations used					
		Continuity		Momentum		Energy	
		Ion	electron	ion	electron	ion	Electron
Boeuf et al.[31] 1995	2-D rf discharge in argon at 100mTorr (low pressure) Develops a conservative finite difference	(2.40)	(2.39)	(2.42)	(2.41)	-	(2.44)
Colella et al.[86] 1999	method for plasma fluid equations for high density low pressure plasmas Numerical modeling of	(2.40)	(2.39)	(2.43)	(2.41)	-	(2.44)
Hammond et al.[90] 2002	low-pressure, high density rf discharges in Helium	(2.40)	(2.39)	(2.43)	(2.41)	-	(2.44)
Lee et al.[34] 2004 Golubovskii et al.[56] 2004	1-D parallel plate discharge in helium at atmospheric pressure 2-D asymmetric discharge	(2.40)	(2.39)	(2.42)	(2.41)	-	-
Roy et al. [15,115] 2005	actuator modeling in air/He (300 torr)	(2.40)	(2.39)	(2.42)	(2.41)	-	-

It should be kept in mind that the choice of convection scheme is also determined by its performance in the range of Peclet numbers encountered and also in the presence of a source term [91]. In the following discussion we will restrict ourselves to the set of governing equations as presented in (2.39)-(2.44). The challenge here is to efficiently handle multiple time scales, and the treatment of the reaction source terms. Such complications are more common in the modeling of reacting flows where detailed modeling of chemical kinetic mechanisms can result in a stiff system of governing equations. The focus of the present dissertation includes the development of an efficient solution algorithm to handle the stiff multi-scale problem as seen in the context of the plasma dynamics. The discharge equations as described in (2.39)-(2.44) involve wavelike ionization fronts which travel through the domain before charging the dielectric or any other boundary surface. The solution procedure needs to be designed to handle the multiple scales efficiently. However, one distinct difference between chemically reacting flows which pose similar challenges is the electric field effect. It has been shown in [86] that the plasma sound speed is modified by the electric field drift with the effective ion sound speed given by

$$c_i = \sqrt{\frac{kT_e + \gamma_i kT_i}{m_i}} \quad (2.56)$$

Here T_e refers to the electron temperature which is usually very high compared to the ion temperature (which is closer to the neutral particle temperature). Thus the modified sound speed is much higher than the neutral sound speed (as ion temperature is \sim neutral). Note that the first term in the square root with T_e comes from the approximation of the electric field in the electrostatic pressure. In the absence of a driving electric field, this term vanishes giving the neutral fluid sound speed (the second component in the square root).

When $T_e \gg T_i \sim T$, the electric field dominates the thermodynamic pressure. Similarly, the characteristic speed for electrons can be obtained as

$$c_e = \sqrt{\frac{kT_e + \gamma_e kT_e}{m_e}} \quad .(2.57)$$

The above expression for the ions shows that the electric drift component is more significant than the thermal component. The ratio of the two species sound speeds goes as the inverse of the square root of their respective mass. The electrons being lighter than ions are faster. In general, from the range of electric fields considered in this problem, the ion and electron sound speeds are much higher than that of the neutral flow and hence the bulk of the acoustic effects are caused by the driving electric field and not the low speed neutral flow. This is different from normal chemically reacting flows where the species characteristic speeds are comparable to that of the neutral fluid. This distinction needs to be kept in mind while dealing with the above strongly convective equations where the reaction and convection time scales are comparable.

Integrating such a system comprising many time scales gets very demanding in terms of computational resources. Both implicit and explicit techniques have been used to march in time with the choice usually based on the extent of stiffness of the system, expected time accuracy etc. Implicit integration methods are attractive in the sense that they are unconditionally stable, but are not time-accurate and in some non-linear situations are even computationally burdensome. This is necessitated by the need to find the root to a highly non-linear equation which might entail very small time-steps to achieve convergence. Also, there is a burden of huge computational requirement. This method works reasonably well when the overall timescales are not very far apart. Several studies aimed at improving the efficiency of stiff integration schemes have been studied

in the context of modeling reacting flow and atmospheric chemistry which involve taking advantage of the problem specific approximations to the Jacobian. In other examples, the stiff variation of the reaction terms which is typically exponential makes it advantageous to study the variation of the logarithmic quantities as against original variables [90]. Another alternative to the implicit procedures used above is the use of matrix free Newton-Krylov methods, which have been reviewed in [92].

Both sequential and fully implicit approaches have been used for discharge modeling. Roy et al.[15-16] used a globally implicit finite element procedure where the system of species continuity and momentum equations are assembled as part of a global matrix to solve for the solution vector. Sequential approaches have also been employed such as in the study of Hammond et al.[90]. Hammond et al.[90] uses a hybrid formulation to solve the plasma fluid equations, where the ions species being slower are treated by an explicit 4th order Runge-Kutta method followed by an implicit treatment of the fast electron equations. The implicit Euler (first order) and implicit Runge-Kutta (second order) methods were used with Newton-Raphson iterations to overcome the non-linearity. Further, the resulting Jacobian is simplified by neglecting the weak off diagonal contributions reducing to a block tri-diagonal system. However, taking into account the computational overhead from the iterative procedure for the fully implicit treatment and the cost of inverting the matrix more than compensated for the gain over explicit procedures. Implicit procedures though are used in the context of obtaining steady state solution with stability and not time accuracy as the consideration. Acceleration to steady state is usually achieved using preconditioning techniques (for e.g. [93]) which decrease the condition number of the system with widely separated scales. These techniques have

been extended to time accurate computations by Merkle [94]. Schwer et al.[95] uses a consistent splitting of operators with implicit transport computations of reacting flows using local preconditioning (Merkle et al.[94]).

Recent modeling strategies use semi-implicit hybrid procedures which seem to be more attractive especially in the context of operator split methods. Here the stiff portions of the system are handled using efficient solvers and integrated with the non-stiff solution procedure. A common practice to handle the stiff reaction terms is to integrate the reaction ODE using a stiff ODE solver (CVODE, DVODE, LSODE) over a time step determined by a non-stiff process. These are essentially based on the backward differentiation formulae of Gear. This integration time-scale in most problems is the convection time-scale of species which is considerably larger. Such a procedure makes for a sequential approach and thereby enables handling smaller time scales by allowing integration sub-cycles for the relevant portion. However, stability and coupling demands appropriate corrector steps and handling of splitting and conservation errors.

Source term treatment in plasma simulations has been discussed by Hagelaar et al.[96] where a linearized implicit correction is used to alleviate the stiffness by means of a semi-implicit solution. This is similar to another common technique which is the point-implicit treatment where the source terms are treated implicitly with a single Newton iteration. Here the source term is linearized and written in terms of a Jacobian which needs to be evaluated every time step. Also, if there are a large number of species with complicated chemistry, inverting the sparse Jacobian becomes expensive and it is common practice to resort to simplifications to accelerate convergence. Updating of the Jacobian is also done only when absolutely necessary and is not usually done for every

step unless it seriously affects convergence. It is shown in [97] that this point implicit method is a special case of a generalized time scale preconditioner where the stiff processes are scaled in time to the speed of slower processes. Preconditioning techniques used to handle multiple scales to solve steady state problems and are reviewed by Turkel [93]. Implicit treatment of stiff terms provides solutions which are accurate at the slow scales and stable at the fast scales. Overall, a fully implicit technique is rarely used, especially with the strong coupling between the various species equations and the resulting non-linearity. However, with the use of efficient solution techniques such as implicit multigrid methods and efficient solvers like LU-SGS of Yoon et al.[98] high speed reacting flows with strong convection have been successfully handled implicitly. In spite of using inversion techniques as above, the species chemistry Jacobian makes it a block inversion which can get expensive. Hence, it is common practice to simplify the species chemistry either adaptively or uniformly or to treat the reaction terms in a partially implicit fashion so that block inversion can be reduced to a scalar inversion.

Explicit methods have been developed to deal with stiff problems, such as stabilized multi-stage Rung-kutta schemes, Runge-Kutta-Chebyshev (RKC) [99] schemes which possess extended real stability intervals. However, with the stability range dependent on the number of stages employed, the computation increases for handling very stiff problems and is almost comparable to implicit schemes. A review of explicit schemes for stiff problem can be found in Verwer [99]. Explicit time-scale splitting using computational singular perturbation (CSP) is presented by Valorani et al.[100]. Here, the fast and slow time scales are split such that the algorithm marches with the slow time

scale with the faster time scales being taken into account at the end of the integration time-step as a correction.

Operator splitting methods are used in reacting flow computations and are discussed in [101]. The treatment of source term using operator splitting has been popular in the computation of reacting flows and discussed in Najm et al.[102] and Oran and Boris [101,102]. Here, the stiff reaction operator is treated as a stiff ODE using the DVODE integrator [103] and is embedded as part of a projection method. Colella et al.[86] employs a time-split integration algorithm of the species equations in a sequential form to decouple the three possible stiff processes namely ionization, convection and dielectric relaxation. The different species equations are handled in a sequential formulation in a predictor-corrector approach wherein the evolution of the various species is appropriately coupled to the electric field.

In the present multiple study, we have employed an operator-split sequential solution algorithm. Some examples of studies which employed such ideas are Najm et al. [102] in combustion problems, Verwer et al. [99] in atmospheric chemistry modeling and Tyson et al. [104] in chemotaxis models. Here, the solution procedure can be adapted to handle the individual processes efficiently and realize overall gain in computation. However, such an approach requires careful attention to stability considerations and performance is highly dependent on the physics of the problem. In certain situations the presence of competing stiff processes can lead to a system with much larger dynamical time-scale than dictated by the individual processes. Such dynamic equilibrium usually cannot be predetermined in general for a non-linear advection-diffusion-reaction system. The stiffness of the reaction part is typically overcome by using stiff integration

procedures in ODE integration packages [105] such as the ones based on the backward-difference formulae (BDF). In using time-split algorithms for processes operating in a range of time-scales, the choice of time-step size is typically determined by the smallest time scale, but need not necessarily be chosen as such. To speed-up the solution procedure, an intermediate time scale is chosen to advance the overall system in time, while the faster processes are advanced by sub-cycling within the time-step. In the present study, the time-step dictated by the slower ion species convection is targeted to march the full discharge system while sub-cycling is used for the faster processes. Also, a predictor-corrector approach is employed to ensure sufficient coupling between the electric field and the species densities. A strong coupling is essential for achieving stable time-accurate simulations while using a sufficiently large global time-step. This method is integrated with a multi-block finite-volume algorithm capable of handling 3-D curvilinear-grids [19]. The implemented solution algorithm conserves space charge and avoids dielectric relaxation time step restrictions. In the following section, an outline of the algorithm is presented.

The split solution algorithm consists of the following steps:

1. Predictor step
2. Solving the Poisson equation
3. Corrector step

1. Predictor step: At the beginning of the $n+1^{\text{th}}$ time level and for the k^{th} species, we have n_k^n, v_k^n, E^n and v_k^n as the known quantities. Here the species continuity equations (2.39)-(2.40), along with the drift-diffusion momentum equations (2.41)-(2.42) are integrated using lagged values for the various coefficients (as they are a function of the

electric field E). The source term is integrated using a higher-order (4th-order) BDF using the CVODE solver [103]. The convection and diffusion operators can be treated either implicitly or explicitly. In this case, we will employ a second-order upwind for the convection term and second-order central difference for the diffusion term. The continuity equation can be written as

$$\frac{\partial n_k}{\partial t} + \nabla \cdot (n_k v_k) = \nu_{c,k} n_k \quad (2.58)$$

As can be seen from Table 10, the presence of processes with disparate time scales can possibly be better handled using operator splitting. Three types of splitting are popular, namely,

- (i) First-order splitting
- (ii) Strang splitting
- (iii) Source splitting.

(i) First-order splitting: The first-order splitting [101] can be written symbolically as

$$\bar{n}_k = T^{M_k}(\Delta t') S(\Delta t) n_k^n \quad (2.59)$$

where S is the reaction operator integrated using the ODE solver CVODE [103] and T is the transport operator. M_k is the number of substeps used for the transport term integration to march to the global timestep Δt . Therefore, we have

$$\Delta t' = \frac{\Delta t}{M_k} \quad (2.60)$$

(ii) Strang splitting: The Strang's time splitting method [106] solves for the conservation law without the source term and the ordinary differential equation (ODE) with the unsteady term and the source term in an alternating fashion. This method is formally second-order in time which is achieved by splitting the operators symmetrically. In this

case, the transport term integration is usually split into two halves to achieve the symmetry since the ODE solver used for the reaction part is computationally burdensome.

$$\bar{n}_k = T^{M_k/2}(\Delta t') S(\Delta t) T^{M_k/2}(\Delta t') n_k^n \quad (2.61)$$

It is worth noting that, in both the first-order and Strang splitting procedures the initial guess for the reaction part is not directly from the previous time-step, but after a half or full time-step of the transport term integration. This results in the introduction of stiff transients in the solution which are nothing but an artifact of the splitting errors arising from the lagged treatment of the coupled processes. These can have significant impact in the presence of strong non-linearities. Even though the Strang splitting is formally second-order, it is rarely achieved [107] in certain stiff problems, where it is known to deteriorate to lower order accuracy. To overcome the solution discontinuities which give rise to stiff transients in the above two splitting methods, the source splitting treats the transport as a piecewise constant source.

(iii) Source splitting: In this study, we limit the discussion to first-order source splitting [99]. For the source splitting, we can write

$$\tilde{n}_k = S(\Delta t) n_k^n \quad (2.62)$$

and

$$\dot{n}_k = \frac{\tilde{n}_k - n_k^n}{\Delta t} \quad (2.63).$$

Therefore, we have

$$\bar{n}_k = \left(T(\Delta t') + \dot{n}_k(\Delta t') \right) n_k^n \quad (2.64)$$

where S is the reaction operator integrated using the ODE solver CVODE [105] and T is the transport operator. M_k is the number of substeps used for the transport term integration to march to the global timestep Δt . Thus, we have

$$\Delta t' = \frac{\Delta t}{M_k} \quad (2.65)$$

The ODE solver employs the following:

- A 5th-order BDF for time integration.
- Newton iteration for non-linearity.
- A direct method with a banded treatment of the Jacobian.
- Normal mode with subcycling within the time-step.
- Relative and absolute tolerances of 1e-12 and 1e-14 respectively.

The above strict tolerances were chosen so that the ODE integration is almost exact. After the predictor-step, we have obtained the guessed values for the species number densities based on the lagged value for the electric field. The strong super-linear dependence of the convection on the electric field dictates the overall stability and requires strong coupling between the variables.

2. Solving the Poisson equation: Here we solve a semi-implicit version of the Poisson equation to overcome the space charge stability constraint leading to the dielectric relaxation time-step constraint. This time step restriction is usually one of the most severe and is equivalent to the CFL type stability criterion for the current continuity equation.

The Poisson equation is

$$\nabla \cdot E = \frac{e}{\epsilon_0} (n_i - n_e) \quad (2.66)$$

The origin of the restriction has been illustrated earlier in this section in (2.51)-(2.55). This restriction is primarily caused by the non-implicit treatment of the electric field in

the species momentum equation. In order to overcome this, a linearized implicit treatment for the species number densities is used.

$$\nabla \cdot E^{n+1} = \frac{e}{\varepsilon_0} \left(n_i^{n+1} - n_e^{n+1} \right) = \frac{e}{\varepsilon_0} \left(n_i^n - n_e^n + \Delta t \left(\frac{\partial n_i}{\partial t} - \frac{\partial n_e}{\partial t} \right)^n \right) \quad (2.67)$$

which can be written using the species continuity equations as

$$\nabla \cdot E^{n+1} = \frac{e}{\varepsilon_0} \left(n_i^n - n_e^n - \Delta t \left(\nabla \cdot (n_i v_i) - \nabla \cdot (n_e v_e) \right)^n \right) \quad (2.68)$$

Note that the only term in the right hand side which contains the velocity and hence the electric field (through the drift-diffusion form of the momentum equation) is the one inside the brackets with Δt . By treating this term implicitly we can overcome the dielectric relaxation time step restriction. The implicit version of the equation can be written as

$$\begin{aligned} \nabla \cdot E^{n+1} &= \frac{e}{\varepsilon_0} \left(n_i^n - n_e^n - \Delta t \left(\nabla \cdot (n_i v_i) - \nabla \cdot (n_e v_e) \right)^{n+1} \right) \\ &\approx \frac{e}{\varepsilon_0} \left(n_i^n - n_e^n - \Delta t \left(\nabla \cdot (\bar{n}_i v_i^{n+1}) - \nabla \cdot (\bar{n}_e v_e^{n+1}) \right) \right) \\ &= \frac{e}{\varepsilon_0} \left(n_i^n - n_e^n - \Delta t \left(\nabla \cdot (\bar{n}_i \mu_i^n E^{n+1} - \nabla (D_i \bar{n}_i)) - \nabla \cdot (\bar{n}_e \mu_e^n E^{n+1} - \nabla (D_e \bar{n}_e)) \right) \right) \end{aligned} \quad (2.69)$$

Here the ion density at the time level $n+1$ is approximated by the predicted density at the end of step 1. The species velocities are directly substituted using the drift-diffusion approximation so that the electric field can be treated implicitly. In the event, the full species momentum equations are solved in step 1, the predicted velocity thus obtained (with the bar) will be used in the Poisson equation. In that case, the non-linearity will be difficult to overcome and will need a Newton-Raphson type treatment. The equation (2.69) leads to a symmetric system for the electric field which needs to be inverted. This

can be done using a point Gauss Seidel method with successive over relaxation (GS-SOR) or a line SOR. The cost of this step is possibly one of the most demanding and hence needs to be performed as less frequently as possible. The choice of the global time-step Δt will be determined taking this into account.

3. Corrector step: At the end of the previous step, the predicted species densities \bar{n}_k and the electric field at the new time level E^{n+1} are available. Now we will obtain the corrected densities at the new time level. It is worth noting here that the corrector step is needed to ensure adequate coupling between the electric field and the species number densities. In other words, we require appropriate coupling between the species continuity equation and the momentum equation (or the drift-diffusion equation). Hence, the corrector step is the same as the predictor step, but performed with the updated coefficients using E^{n+1} . It is also worth noting that if the diffusion term and the source terms are not strongly impacted by the electric field, then the corresponding operators can be removed from the corrector step as correction is required only for the convection term in such cases.

Stability. The stability criterion for the above predictor-corrector approach with stiff sub-steps is not straightforward. Of the time scales listed in Table 10, the ionization source term and the dielectric relaxation time step restrictions are not binding in the above algorithm. The implicit treatment for the reaction source term makes it unconditionally stable and is limited only by the non-linearity. The predictor-corrector formulation with the semi-implicit solution of the Poisson equation ensures space charge stability overcoming the dielectric relaxation time restriction due to the non-linearity. With the split integration procedures for the convection and other processes, the stability of the

system will be determined by the CFL conditions for the individual steps. The global integration time-step Δt , is determined by the slower moving ion CFL condition. Here λ is the CFL number for the different species.

$$\lambda_{i,CFL} = \left| v_i^{\max} \right| \frac{\Delta t}{\Delta x} \quad (2.70)$$

In the case of a number of different species considered, the choice of the global time-step is usually the convection time scales of the slowest species, unless there is a huge variation. This is important if we are considering the neutral species in reaction chemistry whose dynamics are determined by the slower moving neutral fluid. Once this is fixed, the time-step for the faster electron species and the corresponding number of sub-steps M , can be obtained, so as to satisfy the electron CFL limit. However, studies [108] indicate that the CFL stability limits of the split algorithm deviates from that of unsplit algorithm depending on the number of sub-steps M , employed. Knio et al.[108] shows that the critical CFL number due to electron convection sub-stepping decreases monotonically as the number of sub-steps increases in two-dimensional modeling studies of reacting flows. Also, one-dimensional studies indicate a limiting value of the critical CFL being achieved as the number of sub-steps is increased. In spite of the stability criterion becoming stringent the overall computational savings is generally substantial.

3.2.3 1-D Parallel Plate Discharge Modeling in Helium

We study the following test problem to validate our computational capability. A 1-D parallel plate (5mm gap between electrodes) discharge at atmospheric pressure using just two-species chemistry, driven by a voltage of 1.5 KV at 10 KHz was modeled as shown in Figure 8. This model problem has been studied by Ben Gadri et al.[20] and Massines et al.[6]. The governing equations are the species continuity equations ((2.39)-

(2.40)) and the momentum equations with the drift-diffusion approximation ((2.41)-(2.42)). No energy equation is solved for this model. The gas used is helium with a small impurity of Argon (0.5 percent) to simulate the Penning effect arising from the impurities. The parallel plates used are covered by a layer of dielectric with permittivity 9.0 and 0.6 mm thick. A detailed description of the arrangement is presented in [20]. The various transport parameters, such as the species mobility, diffusivity and ionization coefficient are tabulated as a function of the electric field using the ‘BOLSIG’ database. A simplified kinetic model with various collision cross sections is used to develop the database for the various types of species and these are locally interpolated in the code.

The boundary conditions are such that the fluxes near the boundary charge the dielectric which is very significant in terms of maintaining a controlled discharge. However there are inherent difficulties in the fluid model of the plasma in representing the near wall sheath regions. Hence different sets of boundary conditions have been employed in different studies [34,58,62]. For the 1-D species continuity equation we need two boundary conditions in space for the number density. A few of the different choices of boundary conditions employed are shown below in Table 12. A detailed discussion of the issues in the choice of boundary conditions for fluid models of plasma is presented by Hagelaar et al. [109]. In the present discussion we employ set of boundary conditions 1 from Table 12. A uniform time-step of 10^{-9} seconds is used for the time-integration and the domain is uniformly discretized into 201-points. A fine grid with double the number of points is also used and the results are compared with that of Massines et al.[6]. The discharge current over a period of one full cycle after a quasi-steady state has been attained during the discharge is self-sustained and is periodic as shown in Figure 9.

Table 12 Different types of boundary conditions for the ions and electrons used in modeling studies.

Serial no	Ion BC's		Electron BC's	
	Cathode	Anode	Cathode	Anode
1	$\frac{\partial n}{\partial x} = 0$	$N=0$	Sec emission Flux	$\frac{\partial n}{\partial x} = 0$
2	$\frac{\partial n}{\partial x} = 0$	$\frac{\partial n}{\partial x} = 0$	Sec emission Flux	$\frac{\partial n}{\partial x} = 0$
3	$\mu E n + \frac{nv_{th}}{4}$	$\frac{nv_{th}}{4}$	$\frac{nv_{th}}{4} + \text{sec emission}$	$\mu E n + \frac{nv_{th}}{4}$

Note: V_{th} is the thermal flux at the boundary.

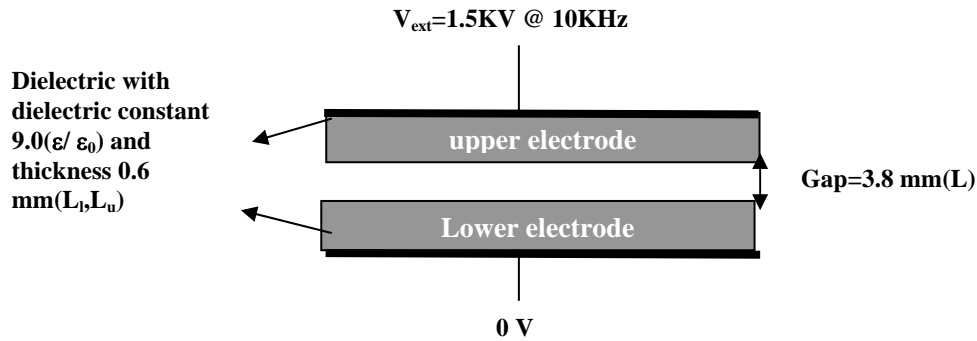


Figure 8 Parallel plate arrangement for modeling DBD discharge

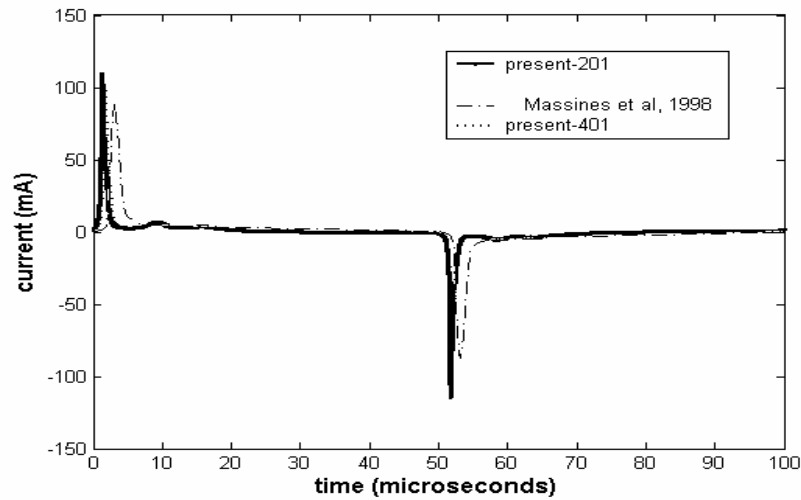


Figure 9 Evolution of discharge current over one period of the discharge cycle

The curves compare the coarse and fine grid results obtained in the present model with that of Massines et al.[6]. As can be seen from Figure 9, the current peak representing the instant after the breakdown slightly differs from that obtained in the reference study. Also, there is a slight difference in the magnitude of the peak current. The possible source of difference could be traced to the slight differences in the choice of material data for the various species employed. However, the overall physics is adequately represented although quantitative differences exist.

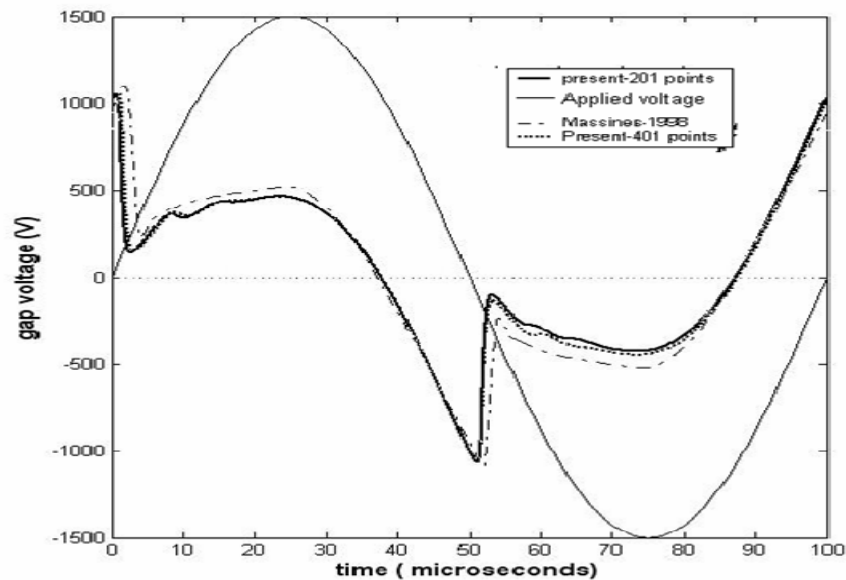


Figure 10 Evolution of the gap voltage over one full cycle

The gap voltage which is the net voltage between the two dielectric layers (or the air gap to be specific) after accounting for the charge build up on the dielectric surfaces is shown in Figure 10. The deviation from the reference results is again seen, but the coarse and fine grid solutions are not much different, indicating possible grid convergence. The peak gap voltage is at the instant just before the breakdown and it drops sharply after the discharge peak, with large currents as seen in the previous figure reducing the voltage. The distribution of the two species especially, the ions and the electrons, during the

discharge are of interest, especially for the present study where the force acting on the fluid needs to be accurately calculated. The species number density distribution over the domain at the instant of the peak current density is presented in Figure 11. The comparison shows that the present calculations have a ten percent error in the peak value of the ion and electron densities. The fine grid results show identical peak densities and hence not shown here. The very small time step required in the above study makes operator split treatment of the various stiff processes necessary. This split approach will be even more valuable when the plasma dynamics need to be solved coupled with the fluid dynamics. As the faster fluid dynamics evolves, they will interact significantly with the evolution of the discharge.

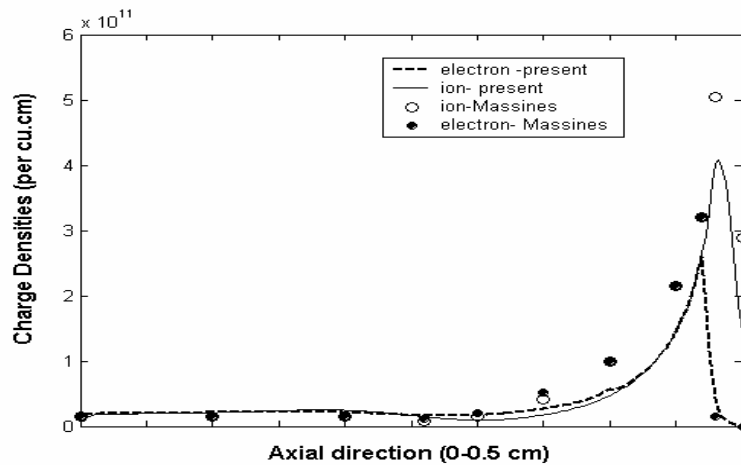


Figure 11 Comparison of peak current species density distributions of the present effort with Massines et al.[6].

3.3 Integration of Plasma Dynamics with Fluid Dynamics

The above discussion pertains to the modeling of the high frequency glow discharge independently which needs to be incorporated in the Navier-Stokes calculations for modeling the coupled system. The first issue is the effect of the neutral flow on the plasma dynamics which needs to be captured. The actual species momentum equation in

a neutral flow would need to include the pressure gradient contribution from the fluid dynamics. We can argue the total pressure as a sum of the partial pressures of the plasma species and the neutral fluid particles. The momentum equation (2.41)-(2.43) should also account for the neutral fluid pressure gradient. Hence the modified momentum equations in the drift-diffusion form are

$$\text{Electrons: } n_e v_e = n_e \mu_e E - \nabla(D_e n_e) - \nabla p_{fluid} \quad (2.71)$$

$$\text{Ions: } n_i v_i = n_i \mu_i E - \nabla(D_i n_i) - \nabla p_{fluid} \quad (2.72)$$

where p_{fluid} is the pressure effect of the neutral fluid. Since we are using the two-fluid model for the plasma-fluid mixture and with the plasma sound speed being much greater than the neutral flow sound speed, the effect of the neutral fluid transport on the species dynamics will be much smaller than the electric drift for the charged species which makes the two pressure gradients in (2.71)-(2.72) negligible. However, the neutral reactant species such as the metastables will still convect on the fluid dynamic scales and evolve at a different rate. Therefore the modeling strategy can use a coupled solution method where the above time-split integration of the plasma model is embedded into a fractional step Navier-Stokes solver such as PISO [110]. In such an arrangement, the corrector step just corrects for the fluid dynamics part of the plasma species equations. This is an approach which is used in the modeling of reacting flows and is computationally demanding. An approximate approach would be to neglect the effect of the neutral fluid flow effects in the plasma discharge equations. This would entail a discharge solution independent of the fluid dynamics which can be solved just once and then be incorporated into the Navier-Stokes equations as shown in Chapter 4. Since the most time consuming part of the solution algorithm is the modeling of the plasma

dynamics, the latter approach makes for a computationally efficient solution procedure. In chapter 4 a framework for representing the plasma effects as a time-averaged body force in the fluid flow is presented. An empirical expression for the body force based on assumed discharge characteristics is used to model the plasma-fluid effects.

CHAPTER 4 MODELING FLUID FLOW WITH PLASMA EFFECTS

In this chapter a framework is presented to model the effects of the discharge on the fluid dynamics. The model for the morphology and time evolution of the glow discharge was presented in the previous chapter. In order to couple the plasma dynamics to the neutral flow an appropriate strategy needs to be used. This usually depends on the problem at hand and the operating conditions. For example, the flow physics needs to be fully coupled and integrated with the discharge plasma simulation if the time scales of the two processes are comparable. Specifically, the largest of the plasma timescales in Table 10 which is typically the inverse of the operating frequency, need to be comparable to the mean flow time scale for the above to be true. However, for the low Reynolds number in the incompressible limit we are interested in, the mean flow responds much slower than the discharge evolution. As an example, the typical fluid flow time-scale for air over a 20 cm chord airfoil at $Re=100$ is of the order of a few seconds while the discharge operates at a few KHz frequency. Hence, a decoupled treatment for the glow discharge with the fluid flow solver would be a reasonable approximation here. In this chapter, a brief description of the body force treatment of the glow discharge plasma will be presented. This is followed by a detailed presentation of the phenomenological body force model and the resulting glow discharge-induced flow effects. Here, an empirical formulation of the body force based on an assumed plasma structure was used to study the resulting flow patterns and the aerodynamics which revealed qualitatively similar characteristics to the experiments. The next section presents the results obtained from the fully self-consistent

plasma dynamics calculations performed on the asymmetric electrode actuator operating on Helium gas using a plasma-fluid model as discussed in the previous chapter. The observed results provide some interesting insight into the mechanism of plasma operation, structure and the resulting force generation. Also, the effect of the various input voltage waveforms, operating parameters (the applied voltage and frequency), electrode spacing and arrangements are studied.

4.1 Body Force Formulation

It is worth recalling that the momentum imparted to the fluid by the discharge is through Lorentzian collisions of the heavier ion species with the neutral particles. We will now revisit the right hand side of the ion momentum equation (2.21) which represents the collision term. Although there will be different kind of collisions, the primary collision loss will be that between the heavier ions and the neutral particles. If we assume that the drift-diffusion approximation (2.25) for the momentum equation is valid, then the net loss due to collision becomes

$$n_i q_i E - \nabla(n_i k T_i) = v_i n_i m_i \mathcal{V}_{mi} = F_{coll}(\bar{x}, t) \quad (3.1)$$

Here, the first term is the contribution from the electric drift and the second is the gradient of the thermodynamic pressure which reduces to more of a diffusion flux if the thermal effects are minimal. If we neglect the diffusion flux, then we get the loss due to collision balanced by the Lorentz force acting on the charged ions. The electrons being lighter are not significant players in terms of momentum transfer. Consequently the electrons reach mean kinetic energy levels higher than those of the heavy components. This loss due to collision F_{coll} can be viewed as the instantaneous local body force acting on the neutral fluid particles and can be modeled as a source term in the Navier-Stokes

equation. Once we have the instantaneous distribution of the ion number density n_i and the electric field E , the instantaneous body force F_{coll} can be calculated as in (3.1). This force acts on a much different time-scale than the characteristic time of the flow and it is important that it be appropriately averaged over time. If we represent the integration timescale by τ and the time-averaged collision force by F_{tave} , we have

$$F_{\text{tave}}(\bar{x}, \tau) = \int_0^{\tau} F(\bar{x}, t) dt \quad (3.2)$$

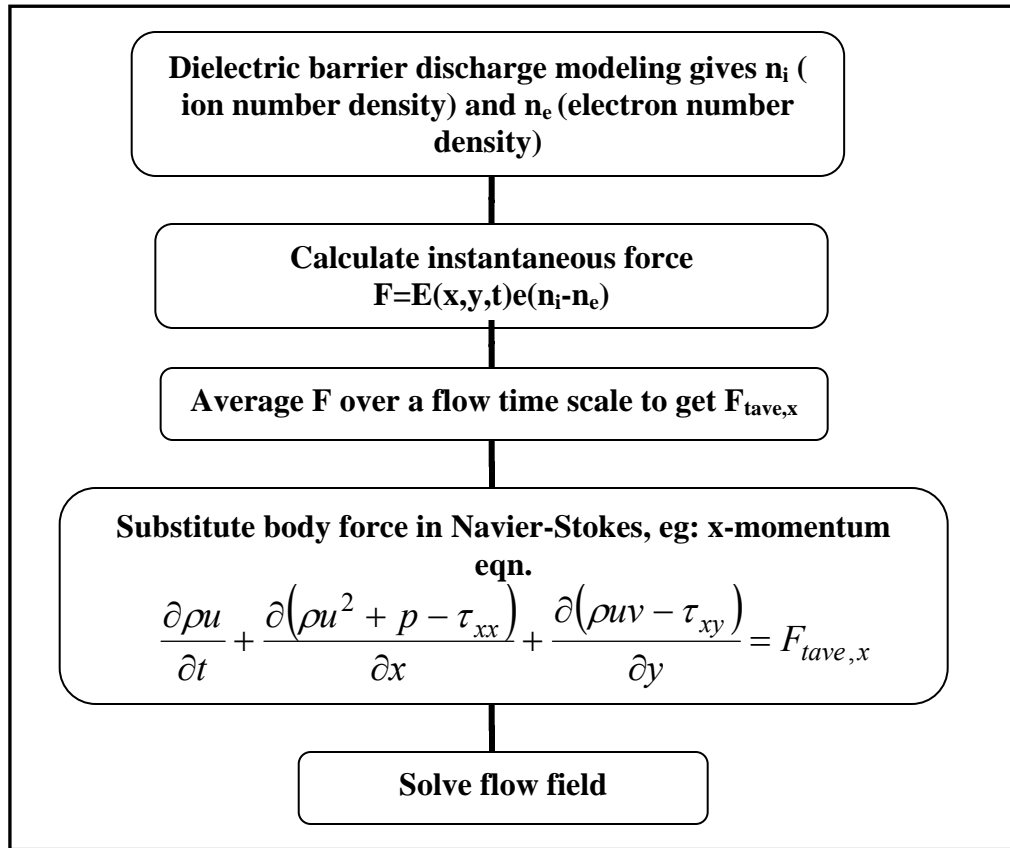


Figure 12 Schematic illustration of the plasma-fluid flow modeling framework.

The choice of this time-scale τ is determined by the smallest of the flow scales which need to be resolved so that the corresponding effect of the force in that time scale can be realized. It is worth noting that if τ is much larger than the time period of the operating voltage cycle, then the averaged force is independent of time. In other words,

the fluid will see the discharge as a source of constant average body force in time. However, if the flow reacts faster than the time period of the driving voltage cycle (which happens to be the largest plasma time scale) then the unsteady forcing effects of the plasma body force will be felt by the flow and hence plasma transients need to be modeled. This is important while modeling subsonic compressible flows or turbulent flows with low plasma frequency. A schematic illustration of the modeling approach is presented in Figure 12.

4.2 Navier-Stokes Equations with Body Force

The numerical model consists of the continuity equation and the two dimensional momentum equations for a steady incompressible viscous flow. The body force terms, which are added to the momentum equations, carry the effect of the plasma discharge on the fluid flow. The fluid is assumed to be incompressible in view of the plasma induced jet being a low Reynolds number and essentially isothermal phenomenon. In the following, we offer a complete set of governing equations, in the two-dimensional form.

$$\frac{\partial \vec{A}}{\partial t} + \frac{\partial \vec{B}}{\partial x} + \frac{\partial \vec{C}}{\partial y} = \vec{D} \quad (3.3)$$

$$\vec{A} = \begin{bmatrix} \rho \\ \rho u \\ \rho v \end{bmatrix} \quad (3.4)$$

$$\vec{B} = \begin{bmatrix} \rho u \\ \rho u^2 + p - \tau_{xx} \\ \rho uv - \tau_{xy} \end{bmatrix} \quad (3.5)$$

$$\vec{C} = \begin{bmatrix} \rho v \\ \rho uv - \tau_{xy} \\ \rho v^2 + p - \tau_{yy} \end{bmatrix} \quad (3.6)$$

$$\vec{D} = \begin{bmatrix} 0 \\ F_{tave,x} \\ F_{tave,y} \end{bmatrix} \quad (3.7)$$

where τ_{xy} is the shear stress and $F_{tave,x}$, $F_{tave,y}$ are the body force components in a 2-D case, as given in (3.2).

4.3 Modeling a Plasma Actuator Using a Phenomenological Force Model

Here we try to model the plasma actuator used by Roth et al.[4] and Corke et al.[25] with dimensions as shown in Figure 13 where L_u , L_l and d are the length of the upper, lower electrodes and gap distances respectively. The plasma generated in this instance is weakly ionized and non-thermal (\sim room temperature) where the electrons alone have a large mean kinetic energy. The ions are more or less in thermal equilibrium with the neutral species because of the extensive collisions with neutrals in a weakly ionized state. A phenomenological plasma model without a detailed simulation is used to depict the glow discharge. The motive of this study was to develop a framework which would take into account detailed balances between momentum transfer mechanisms such as convection, hydrostatic pressure, viscous stresses and the body force arising from the Lorentzian collisions. Now we present a brief phenomenological discussion of the plasma generation in an asymmetric electrode configuration based on our understanding of the plasma structure in a high frequency parallel plate (Massines et al.[6]) arrangement.

4.3.1 Plasma Generation in an Asymmetric Electrode Configuration

At these high frequencies the charged species (mainly electrons) attain high velocities, leaving a very short time for the species to interact and recombine. The ions, being less mobile are believed to be trapped between the electrodes without actually reaching the electrode surfaces. This ion-trapping mechanism is one of the keys for

sustaining the discharge as they ensure adequate seed particles for further breakdown at the beginning of each cycle. This is one of the reasons why at low frequencies (typically $<100\text{Hz}$) when there is enough time to charge the electrodes, the discharge is no more periodic and starts resembling the glows in a DC case. The defining characteristic of the arrangement shown in Figure 13 is the asymmetry which causes the electric field lines to be curved with dominant fringe effects. This distorts the electric field distribution which is far from being uniform and can modify the plasma species dynamics sufficiently. The electric field distribution is strongest in the region closest to the inner edges of the two electrodes which will also be the region of dense ionization. This strength decreases in magnitude as one moves far away from the electrodes.

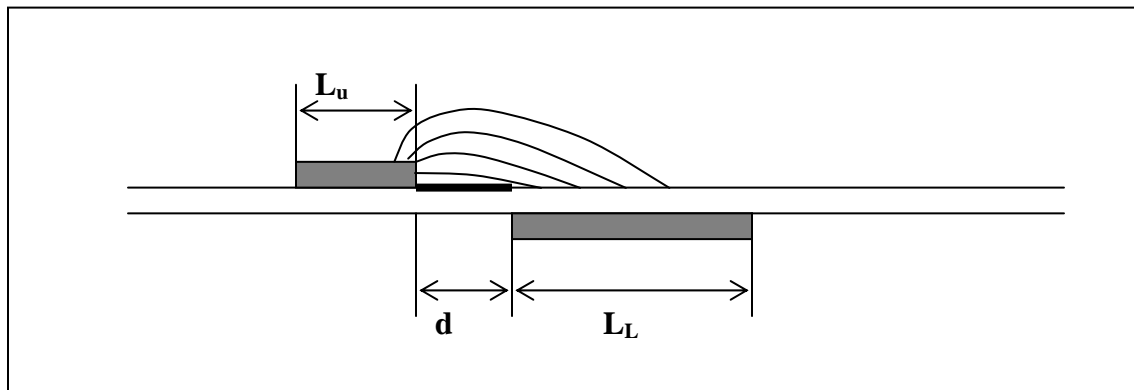


Figure 13 Schematic of the actuator arrangement with approximate shape of electric field lines. The thickness of the electrodes d is 0.1 mm

It was proposed that asymmetry of the anode and cathode configuration as seen by the fluid is responsible for the uni-directional flow generation. Let us look at a single cycle of the discharge. When the voltage rises, the electrons leave the negative electrode (cathode and upper electrode for this half cycle) surface and move towards the anode and in the process are involved in collision, ionization etc. Further, the anode surface (lower electrode) here is not the metal but the dielectric surface which is in contact with the fluid. We can call this as the pseudo anode. Based on Figure 13, the surface area of this

pseudo anode is much larger than that of the cathode. Also the distribution of charges on the dielectric will be different than on an equivalent electrode conductor, as the dielectric prevents movement of charges on the surface. As a result, we have a concentration of charges on the cathode (upper electrode) and a less dense distribution on the dielectric surface, caused both by the asymmetry in the electrode structure and material. Thus we have a much stronger electric field near the cathode and comparatively weak field near the anode. On voltage reversal the memory voltage due to the space charge separation aids recombination which appears as the residual current. Our view is that the weaker electric field near the pseudo cathode (pseudo anode during the previous half cycle) renders the initial accelerating force aiding recombination small when compared to the corresponding force during the previous half cycle. This, in turn results in a lower energy level in the region of the plasma when compared with the first half cycle. Since, in the recombination phase, the lack of electron emission will lead to species depopulation. The subsequent breakdown during this half cycle will depend on the presence of a critical number of electrons with the threshold energy. At low frequency of operation this is usually violated and hence there is little or no breakdown at all. In any case, the discharge in this half cycle is weaker than the corresponding other half. This non-uniform plasma generation coupled with the high-frequency operation can hypothetically explain the thrust produced in one direction alone. It should be stressed that while the electrons are of much higher velocity than ions, due to their small mass their ability to transfer momentum is insignificant. Instead, between the plasma and the ambient fluid, momentum transfer is realized via ions. As can be seen from (3.1), the transferred momentum is a function of both the number density distribution and the electric field

strength. In the present modeling effort we will use the electric field as the key indicator to represent the body force and just consider a uniform species number density distribution. In this study we have incorporated the geometric effect of the electrodes and the resulting impact on the paraelectric force in the computational model.

In the later part of this chapter, we will look at a more detailed first principles-based modeling study to further our understanding of the momentum generation mechanism.

4.3.2 Linearized Electric Body Force

The objective of the following formulation is to sketch a qualitative expression for the body force term acted by the plasma and on the fluid. As one can see from Figure 13, the electric field lines, as shown are concentrated at the cathode and are almost uniformly distributed on the anode. It is reasonable to simply represent the field lines to be parallel in most of the region except the small space near the cathode. Thus as shown in Figure 14, we can linearize the field variation in space without computing the detailed electric field. Specifically, the field lines here are such that the strength of the field decreases as one move far away from the source. This variation of E can be mathematically written a

$$|\vec{E}| = E_0 - k_1x - k_2y \quad (3.8)$$

Where E_0 is the electric field in the darkened region in Figure 13 In general, the constant E_0 is large and, k_1 and k_2 are two positive constants which represent the gradient of electric field intensity along the two mutually perpendicular directions, namely x and y. The positive nature of these two constants ensures that the electric field intensity decreases as one move along the positive directions of the axes.

E_0 can be approximated as

$$E_0 = \frac{U}{d} \quad (3.9)$$

where d (Figure 13) is the distance of separation between the two electrodes in the x direction. The constants are evaluated by using the condition that the field strength is the breakdown value at the plasma fluid boundary. Hence we can find k_1 and k_2 .

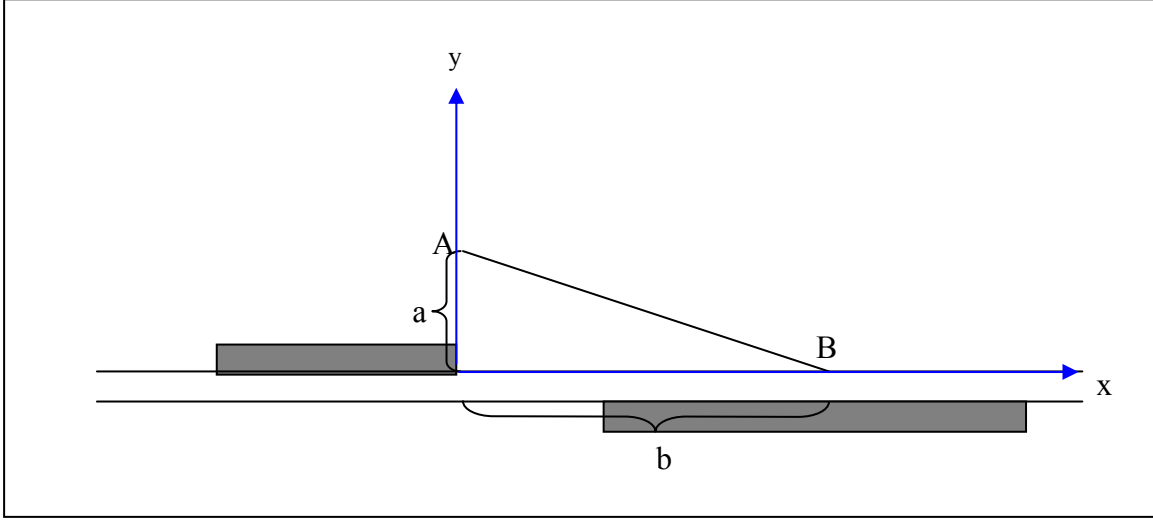


Figure 14 The line A-B constitutes the plasma fluid boundary using linear approximation. The electric field strength outside this line is not strong enough to ionize the air.

The components of the electric field are given by

$$E_x = \frac{Ek_2}{\sqrt{k_1^2 + k_2^2}} \quad (3.10)$$

$$E_y = \frac{Ek_1}{\sqrt{k_1^2 + k_2^2}} \quad (3.11)$$

The period of interest during a particular cycle is the small time Δt during which the plasma discharge takes place. As it is here that we have the high discharge currents and the resulting momentum transfer. The magnitude of this Δt is small compared to the fluid time scales, especially so for the frequency range we are dealing with. Thus the body force components along the x - and y -direction, f_x and f_y , are calculated as

$$f_x = \delta E_x \rho_c e_c \quad (3.12)$$

$$f_y = \delta E_y \rho_c e_c \quad (3.13)$$

This force f , acting on the charged particles is imparted to the neutral molecules. Here, ρ_c is the charge species number density and e_c , the electronic charge. The domain in which the body force acts is determined by the value of E . We use the δ function in the expression for the body force.

$$\delta = 1 \text{ for } E < E_{cr};$$

$$\delta = 0 \text{ for } E \geq E_{cr};$$

The E_{cr} in this case is the break down electric field strength, E_b and represents the voltage boundary. This force acts only during the time Δt (during which the plasma is formed) and that corresponds to one half cycle, as already discussed. The force during the second half of the cycle can be neglected as it has little or no plasma formation. The high frequency of the discharge (around 5 KHz) makes it reasonable to consider the force acting on the fluid as a constant. Hence the force can be time averaged over a complete cycle although it exists only for a small time Δt per cycle.

$$F_{tave,x} = \frac{f_x \Delta t}{T_a} = \nu f_x \Delta t \quad (3.14)$$

$$F_{tave,y} = \frac{f_y \Delta t}{T_a} = \nu f_y \Delta t \quad (3.15)$$

This time period of the cycle T_a is then period of the applied voltage and \mathcal{G} (reciprocal of the time period) is the frequency of the applied voltage. These two components of the body force can be added to the Navier-Stokes equation. We can infer from the above expressions that, when the frequency is zero, the body force term vanishes which is

consistent the expectations. The ' Δt ' used above can be expected to vary with \mathcal{Q} . But this is not the case, as the discharge cannot continue. The memory voltage bounds the Δt in a small range independent of the frequency. This explains the lack of induced flow in the case of DC voltage generated plasma. In the present model, no attempt is made to establish a criterion for the plasma is capable of inducing the fluid flow. Such a criterion requires a more detailed modeling of the plasma dynamics which is presented in section 4.4. The force calculated in (3.14) and (3.15) can be substituted in the Navier-Stokes equations (3.3)-(3.7).

4.3.3 Problem Description

In order to model the plasma induced flow effects a single actuator configuration on flat plate as shown in Figure 13 is included as one boundary of the computational domain as shown in Figure 15. We will only focus on the vicinity of the electrode to investigate the detailed flow field. The flat plate is 20.5 mm long, with the upper electrode fitted 12mm from the leading edge of the plate. The electrode has the length 0.5 mm and the height 0.1 mm. The height of the domain is 10 mm. The flat plate constitutes the lower boundary of the computational domain, with its leading edge 1mm from the vertical boundary of the grid. As shown in Figure 15, three grid blocks constitute the computational grid. The total number of grid points employed is 290x100. The chosen mesh distribution is clustered to focus the computational effort on the flow phenomena occurring around and after the upper electrode where the body force is applied. This grid size and distribution can produce satisfactory solutions in the present study.

The key dimensionless parameters in the present model are:

- (i) Reynolds (Reynolds) number:

$$\frac{\rho_m V_m L_m}{\mu_m}$$

(ii) The ratio of the body force to the inertial force is the same:

$$\frac{\mu_m V_m L_m}{F_m} = \frac{\mu_e V_e L_e}{F_e}$$

where

L is the characteristic length;

V is the free stream velocity;

F is the body force;

ρ is the density;

μ is the coefficient of viscosity;

The subscripts m and e represent the model and experimental values respectively.

For the CFD simulations, we have employed the pressure-based algorithm detailed in [112-113]. The convection scheme we have used is the second order upwind scheme [113].

Boundary condition: The no-slip condition when applied at the solid wall yields,

$$u = v = 0 \text{ at } y = 0 \quad (3.16)$$

At the outlets, zero velocity gradient is assigned taking advantage of the negligible influence of the plasma, far downstream of the electrode.

The plasma discharge boundary is specified by

$$\rho_c = 0 \text{ for } E < E_b. \quad (3.17)$$

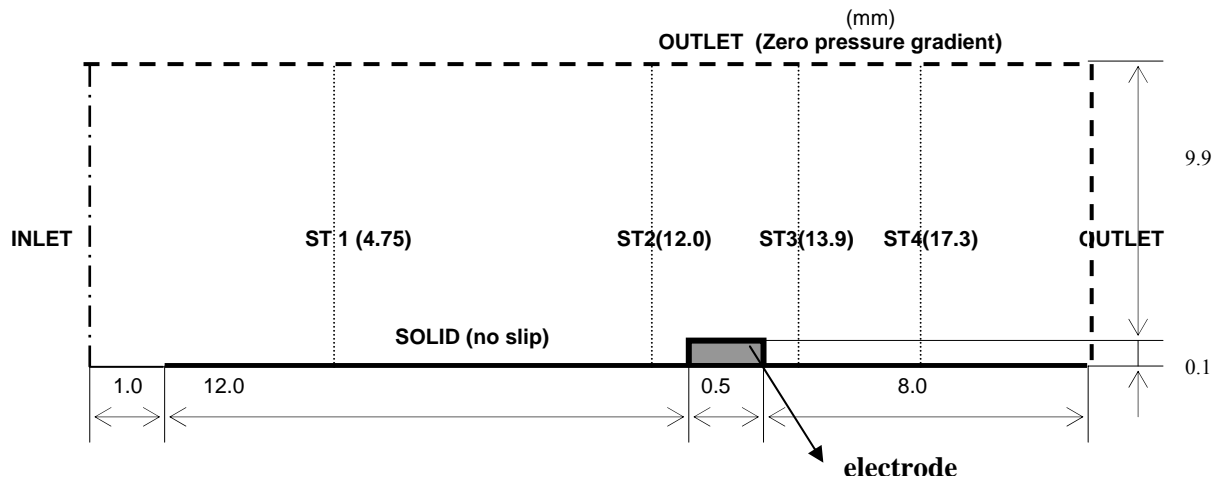


Figure 15 The computational domain used for calculations shows the flat plate with the upper electrode. The various dimensions, the boundary specifications and the stations used for analyzing results are indicated.

4.3.4 Effect on Flow Structure

The various modeling parameters used were the same as that used in the experimental studies [4]. As against experiments which used multiple actuators, only a single actuator was used. Further, heat transfer computations were also performed in which the contact flat plate in Figure 15 is maintained at twice the ambient fluid temperature for the present discussion. All temperatures are non-dimensionalized. The various parameters used are summarized below.

\mathcal{F} = Frequency of applied voltage = 3 kHz

ρ_c = Charge density (electrons) = $1.0 \cdot 10^{11} / \text{cm}^3$

U_a = Applied voltage = 4 kV rms

E_b = Breakdown electric field strength = 30 kV / cm [1]

Δt = Discharge time = 67 μs (obtained from Massines [6])

a = Height of the plasma = 1.5 mm (parameters used to determine the linearized electric field distribution)

b = Width of the plasma = 3 mm (obtained from picture)

d = distance between the plates = 0.25 mm

L_u =length of upper electrode is 0.5 mm

L_l =length of lower electrode is 3.0 mm

An issue of note here is the choice of ρ_c . The value used above is a rough estimate for air based on the data from literature and will vary depending on the gas employed. Specifically for the helium gas we use in section 4.4, the number density is of the order $10^9/\text{cm}^3$. Consequently the force calculated should be expectedly weaker. The values of the various parameters for the different cases in the study are listed below:

- Free stream velocity, V_∞ : 2, 4, 5 and 10 m/s
- Applied voltage, U_a : 3, 4 and 5 kV rms
- Applied frequency, ϑ : 2, 3, 4 and 6 kHz

The corresponding Reynolds numbers (laminar flow) based on the above combinations and the characteristic length, $L_l = 3$ mm (The length of the lower electrode.) are: 411, 822, 1027 and 2054. To study the evolution of the velocity profile and temperature profile four different stations (Figure 15) have been chosen for discussion purposes. In all the results, the reference values for the operating parameters are 4KV rms for the voltage at 3 KHz with a mean flow of 5 m/s which are maintained unless otherwise stated.

The effect of the plasma operation on the various regions of the flow can be seen from the velocity profiles at the various stations is shown in Figure 16. As expected, the maximum peak value of the velocity is obtained downstream of the electrode (i.e. in the high pressure region). The overshoot of velocity above the free-stream velocity indicates the performance index of the actuator. Overall, the velocity structure in the downstream of the electrode resembles that of a wall jet. With the mass being conserved at each vertical plane, the free stream velocity upstream of the electrode does not attain the far-field value, in trying to compensate for the induced mass flux in the wall jet region. The

free stream approaches the far-field value asymptotically as one move far away from the electrode.

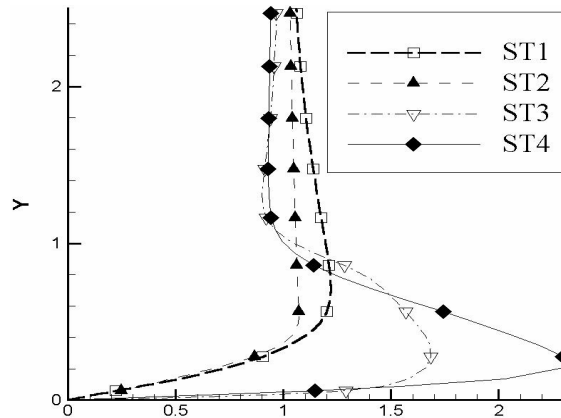
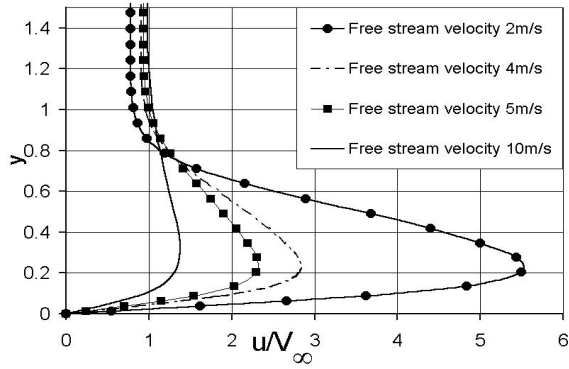


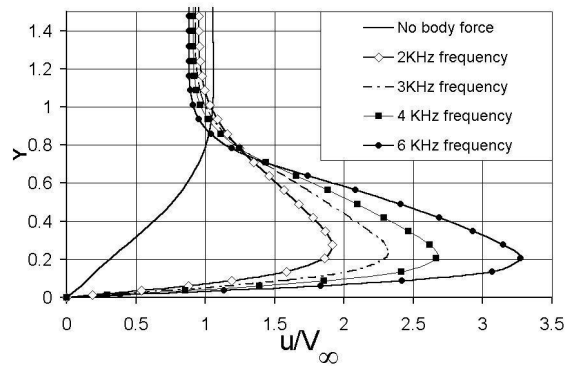
Figure 16 Velocity profiles compared at the four different stations

In the following studies, the parameters which are maintained constant are assumed the reference values of 4KV rms, 3 KHz and 5 m/s for the applied voltage, frequency and inlet velocity respectively. In Figure 17a comparative study of the induced jet velocity profiles for different operating parameters is presented. Figure 17a gives the normalized velocity profile at ST4 for the various free stream velocities. As expected, the plasma actuator is most effective at lower Reynolds numbers. Figure 17b and Figure 17c give the normalized profiles for the different applied voltages and frequencies. The peak jet velocity and the body force are both direct functions of the frequency and applied voltage in the linearized body force model and therefore increase with the actuator operating parameters. It is worth mentioning that with Δt being held constant, the frequency variation becomes a load factor study. However, detailed plasma modeling studies indicate significantly affected plasma structure at different frequencies and this might play a more serious role than just a load factor. In Figure 18, the wall shear profile at ST4 is presented. The wall shear is normalized by the corresponding peak value for the no-

plasma case. Closer to the wall, the wall jet flow reduces the shear stress to a large negative value and farther away the velocities gradually reduce to the free stream value.



(a) Effect of free stream velocity on velocity profiles.



(b) Effect of the frequency of applied voltage.

Figure 17 Effect of the various parameters as seen form the velocity profiles at ST4

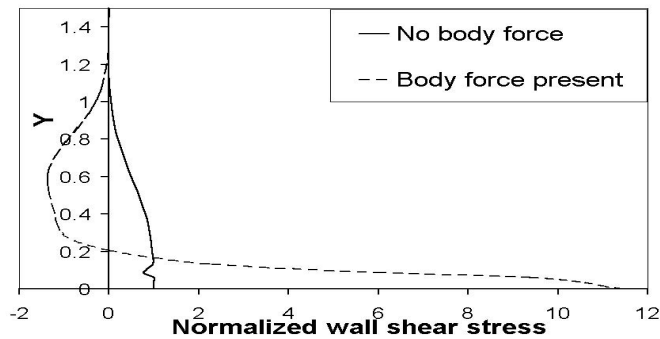


Figure 18 Effect of the body force on the wall shear at ST4

4.3.5 Effect on Heat Transfer

In addition to the flow field, the effect of the induced jet on heat transfer from the surface was also studied. Figure 19 presents the temperature profile along the wall at the different stations. In Figure 19a, the temperature gradient along the normal at ST2, ST3 and ST4 is smaller than that at ST1. This is due to the viscous layer being thinner at ST1. The Reynolds number considered is 1027 (based on the lower electrode length) and Prandtl

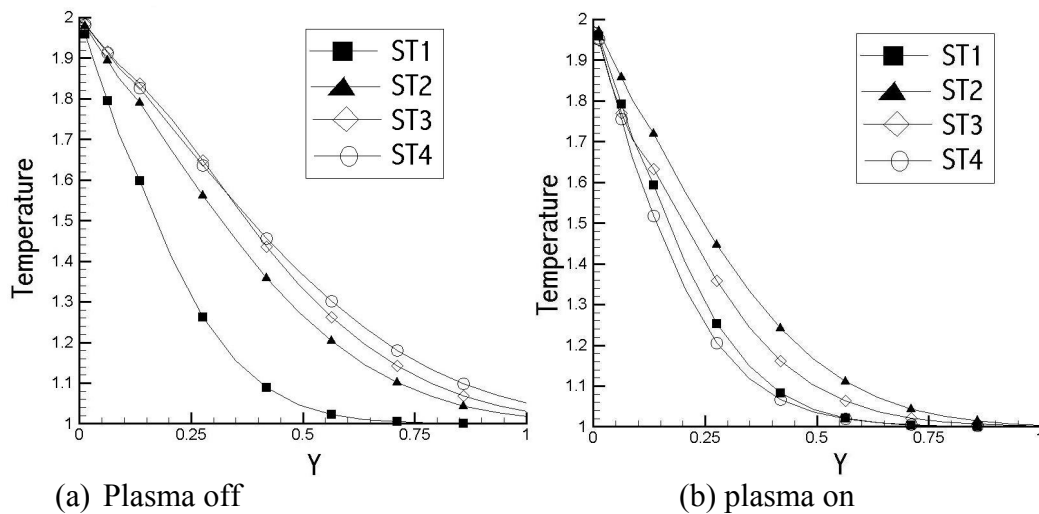
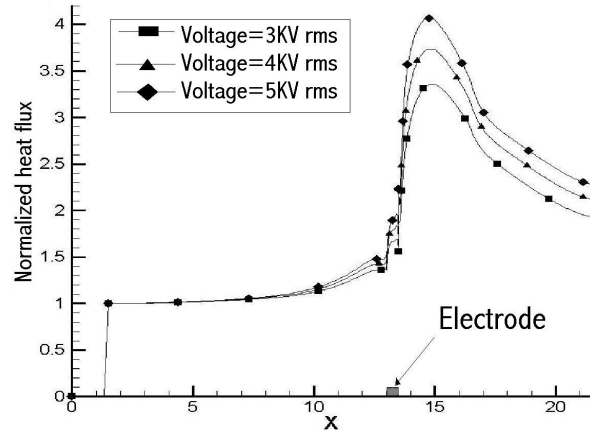
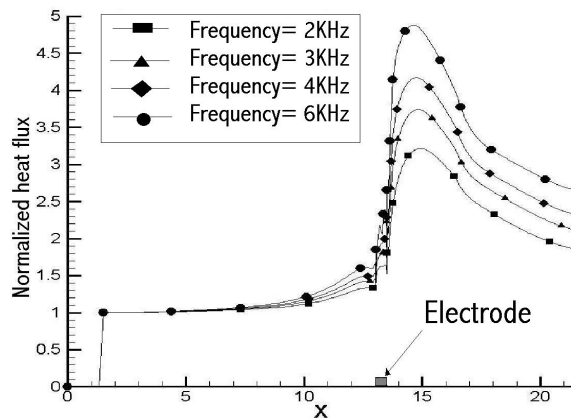


Figure 19 Temperature profile along the wall for $Re=1027$ and $Pr=0.7$

number of 0.7. With the plasma on, the temperature gradients at ST2-ST4 increase but there is no appreciable change at ST1. Figure 20 presents the heat flux from the surface for different applied voltages and frequencies. In Figure 20a and Figure 20b, the effect of the plasma is felt only from a small region upstream of the electrode which is the region near ST2. All heat flux values were normalized using the corresponding plasma off value. The maximum heat flux in the range of frequencies and voltages studied was about four-five times the plasma off value, at a point immediately downstream of the electrode.



(a) Comparison of Normalized heat flux for different applied voltages



(b) Comparison of Normalized heat flux for different frequencies of applied voltage
Figure 20 Comparison of normalized heat flux for different voltages and frequencies

4.3.6. Thrust Estimation

In order to assess the accuracy of the phenomenological body force model developed in the previous sections, we try to compare the thrust produced with the experimental studies [26]. A particular issue pertaining to the model is the procedure for employing the experimental data to fix up the modeling parameters such as the duty cycle, charge density etc. In the following, we present the force prediction under the quiescent condition, in accordance with the experiment conducted by Van Dyken et al.[26]. In these experiments, the force measured is the shear caused by the induced flow on the contact surface in a quiescent environment. After incorporating the duty cycle

factor, the force acting on a fluid element from Eqs. (3.12)-(3.15) and acting on the volume is

$$F_x = \frac{\Delta t}{T} \rho_c e_c E_x A dx \quad (3.18)$$

where A is the area of the face of the differential volume perpendicular to the orientation of dx and E_x is the component of the electric field in the x-direction. Under the linear field approximation, the net force in the x-direction, F_x , acting on the contact surface is obtained by integrating along the discharge operating region b is given by,

$$F_x = \int_0^b E n_x \frac{\Delta t}{T} \rho_c e_c A dx = \int_0^b \frac{\Delta t}{T} (E_0 - k_1 x) n_x \rho_c e_c A dx, \quad (3.19)$$

where n_x is the direction cosine, illustrated in Figure 14. Here, k_2 is neglected as $y=0$ on the surface. From the Maxwell equation we get

$$\left| \frac{dE}{dx} \right| = |k_1| = \left| \frac{\rho_c e_c}{\epsilon_0} \right| \quad (3.20)$$

The absolute values are taken so that we can conveniently ignore the sign conventions while defining the charge on an electron. Using the condition that the electric field is equal to the breakdown field at the edge of the plasma along the surface of the plate we have from (3.20)

$$\rho_c b = \epsilon_0 \frac{(E_0 - E_b)}{e_c} \quad (3.21)$$

The equation (3.20) when substituted in the expression for the force in (3.19) gives,

$$F_x = \int_0^b \frac{\Delta t}{T} (E_0 - k_1 x) n_x k_1 \epsilon_0 A dx. \quad (3.22)$$

Substituting for k_1 and evaluating the integral we get

$$F_x = \left(\frac{E_0^2 - E_b^2}{2} \right) \epsilon_0 n_x A \frac{\Delta t}{T} . \quad (3.23)$$

Note that, by assuming the linear variation for E, we are fixing the direction cosine n_x from the choice of the breakdown lengths a and b.

These two equations (3.21) and (3.23) relate the three parameters, namely E_0, ρ_c and b with the thrust. The duty cycle also varies with the voltage but is assumed constant in the present discussion. All other parameters in the expression for the thrust in (3.23) are fixed within the modeling framework. For a start, let us assume the knowledge of the thrust F and the plasma breakdown length b for a particular value of the voltage. This helps us to calculate the charge number density ρ_c from (3.21) and (3.23). In order to extend the knowledge of two parameters, ρ_c and b, we assume a linear proportionality for above parameters with the applied voltage. The experimental results by Van Dyken et al. [26] present the force generated for various voltages with an electrode 0.625mm wide and Teflon dielectric. Lets us start with a voltage $V=4.66KV$, for which, from the direct measurement, $F=0.3969mN$ and from light intensity measurements given in [26] one deduces that $b=2.8$ mm for the present electrode configuration. The various parameters that are assumed invariant in the present framework are

$$\begin{aligned} \frac{\Delta t}{T} &= 0.77 \\ \epsilon_0 &= 8.852 \times 10^{-12} \text{ Farad / m} \\ A &= 1.15 \times 10^{-6} \text{ m}^2 \\ n_x &= 0.89 \end{aligned}$$

The above duty cycle for a sine waveform of the applied voltage has been measured experimentally by Van Dyken et al.[26]. By substituting the above data into (3.21) we get

$\rho_c = 1.59 \times 10^{11}/\text{cm}^3$. As we can see, this calculated number density is roughly of the same order as the value assumed earlier. Now, the charge number density and the length b are fixed for the assumed voltage. The values of the same for any other voltage can be scaled as:

$$\frac{\rho_{c1}}{\rho_{c2}} = \frac{V_1}{V_2} \quad \text{and} \quad \frac{b_1}{b_2} = \frac{V_1}{V_2}.$$

These values can be substituted back (3.21) and (3.23) to obtain the force. The comparison between the experimentally recorded force and the calculated force is presented in Figure 21.

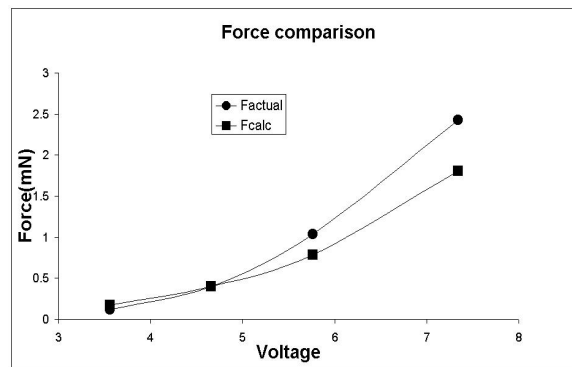


Figure 21 Comparison of the experimental and calculated plasma force for different voltages

Here the F_{actual} represents experimentally measured force while the $F_{\text{calculated}}$ represents the predicted values. While there is a quantitative deviation between the experimental and computational values, the trends between them are consistent. The different results likely arise from linearization of the electric field as well as simplification made during the scaling process described above.

4.3.7 Effect of Plasma on Aerodynamics

The effect of the plasma operation on aerodynamic performance was investigated using the same model as above for the plasma modeling. Corke et al.[25,27] demonstrated that the plasma operation enhances lift as well as drag due to increased shear as well as possible downstream separation of the induced wall jet. In this study, computations were performed in consultation with available experimental evidence [21-22,25] to estimate the generated thrust as well as the aerodynamics. The computational model consists of a flat plate placed in a free stream of fluid as shown in Figure 22. The electrode arrangement serving as an actuator is placed at the middle of the plate. The computational domain encloses the flat plate and electrode arrangement. The boundary conditions for the domain are as shown in Figure 22. To reduce the computational domain and to attain the desirable accuracy, the plate is chosen to be 1cm long, so that the upper electrode, 0.5mm long and 0.25mm thick, can be adequately modeled without excessive computational resources. The main interest here is to probe the effect of the glow discharge-induced fluid flow on the existing flow structures, for both attached and separated fluid flows. The number of grid points used for the simulation is 161×102 . The grid distribution is focused towards capturing the modified flow field in the vicinity of the plasma. The grid points are more clustered near the plate and near the leading edge. The numerical simulation employs a multiblock model solved by a second-order upwind scheme. Detailed discussions can be found in Shyy et al.[112-113]. It is to be noted that, wherever not mentioned, the values for the voltage, frequency and Reynolds number are 4KV (rms), 3KHz and 333 respectively. The values of the various parameters used are

- Free stream velocity, V_∞ : 0.2, 0.4, 0.5m/s
- Reynolds number based on plate length of 0.01m: 133, 266,333

- Angle of attack: 0, 8 and 20 degrees

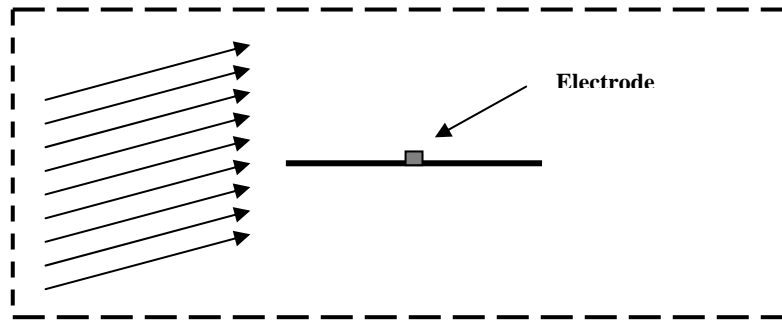


Figure 22 A schematic of the computational domain with the flat plate and the electrode. The electrode has negligible thickness in the above arrangement

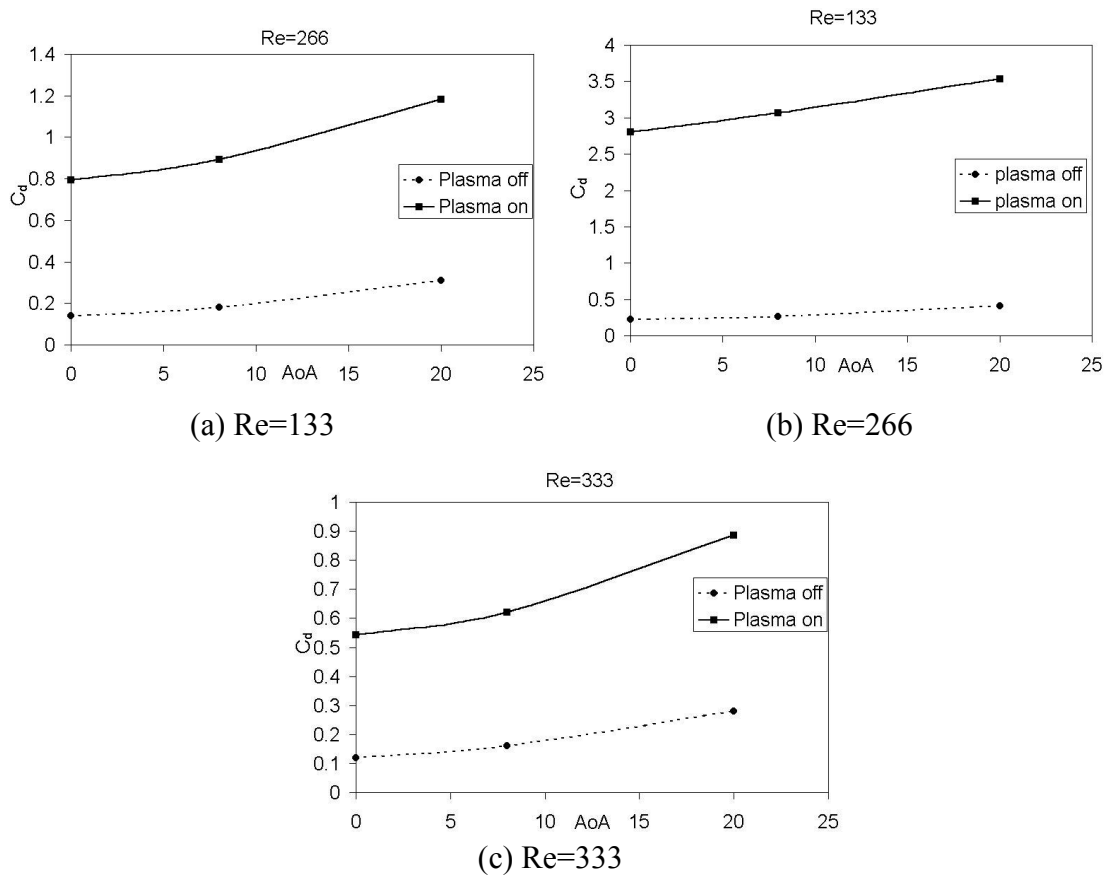


Figure 23 Drag variation with angle of attack for various Re. The plasma is operated at 4KV rms and 3KHz

Fluid flow: The effect of the plasma on various flows at different Reynolds numbers and angles of attack are studied. In the presence of the plasma, the momentum loss will

include the glow discharge-induced body force effect. Figure 23 presents the variation of the drag coefficient with angle of attack for a given Reynolds number in the presence of the plasma. Irrespective of Re, the plasma induced additional drag, which corroborates with the results reported in [25,27]. More importantly, the magnitude of increase in the drag coefficient C_D appears insensitive to angles of attack for a particular Re for the two lower angles of attack (0 and 8 degrees) when the flow is attached. For a 20-degree angle of attack where the flow separates, the plasma effect modifies the separation region and the form drag. The decreased impact of the plasma force for higher Re has been explicitly pointed out by Shyy et al.[9]. The body force term used in the momentum equation is independent of Re and hence becomes smaller when normalized by the dynamic head. We can calculate the increase in drag force ΔD defined by (1.24) instead of the drag coefficient, for a given angle of attack.

$$\Delta D = \Delta C_D \times \frac{1}{2} \rho U^2 \quad (1.24)$$

Table 13 Change in drag coefficient and drag force with Reynolds number

Re	133	266	333
ΔC_D	2.8	0.71	0.46
$\Delta D(N) = \frac{1}{2} \rho U^2 \times \Delta C_D$	6.72	6.816	6.9

Table 14 Change in lift coefficient and lift force with Reynolds number

Re(AoA=8)	133	266	333
ΔC_l	1.51	0.435	0.297
$\Delta L(N) = \frac{1}{2} \rho u^2 \times \Delta C_l$	3.624	4.176	4.455

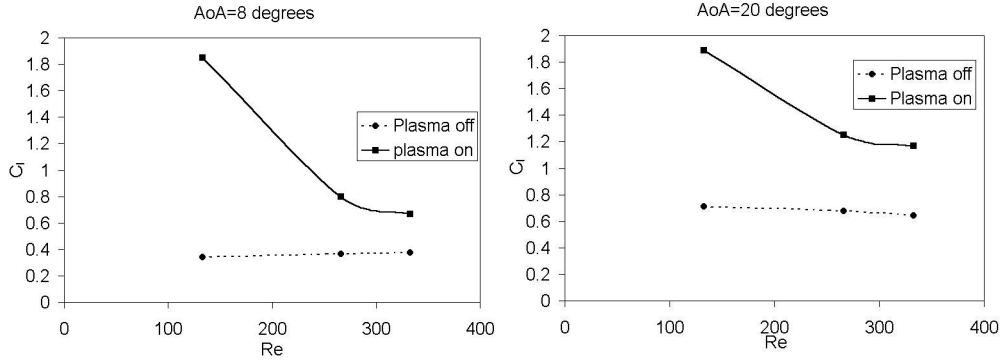
It is observed in Table 14 that the drag force is largely independent of the Reynolds number in the absence of flow separation indicating that, the drag increase is

mainly an artifact of the large plasma force. Similar trends were observed in the experimental results presented by Corke et al.[25]. Figure 24 presents the variation of lift coefficient with Re for a given angle of attack. In general, the plasma on case yields a higher lift. In Figure 24 and Table 14, the increase in lift coefficient becomes smaller as Re increases. However, for separated flows as shown in Figure 24b, there are more substantial increases in lift compared to the attached flow (Figure 24a) with the same glow discharge parameters and Reynolds number. As indicated in Table 14, and consistent with the drag force, the increase in lift force appears to stabilize with larger Re .

Heat transfer: The heat transfer enhancement resulting from glow discharge has been briefly discussed by Shyy et al.[9]. In the present study the heat transfer is studied for various Re and angles of attack. Figure 25 presents the Nusselt number variation with the angle of attack for various Re . The Nusselt number here is given by

$$Nu = \frac{Hl}{K\Delta T} \quad (3.25)$$

where H is the heat flux, l is the characteristic length of the plate, K is the coefficient of thermal conductivity and ΔT is the temperature difference between the ambient fluid and the hot surface, which is set to a non-dimensional value of unity. In all cases, the heat transfer is enhanced during plasma operation and especially so when the angle of attack is high and flow separates. Moreover, the glow discharge-enhanced Nusselt number only exhibits modest variations versus the angle of attack. The plasma helps reattach the flow and enhances heat transfer. The modest deviation in Nu for the high angle of attack cases is due to the incomplete removal of the re-circulation zone. One way to further improve the heat transfer rate is to place multiple electrodes along the stream wise direction to induce stronger fluid flows and also eliminate the re-circulation zone.



(a) Angle of attack= 8 degrees (b) Angle of attack=20 degrees
 Figure 24 Variation of lift with Re for different angles of attack. The plasma is operated at 4KV rms and 3 KHz.

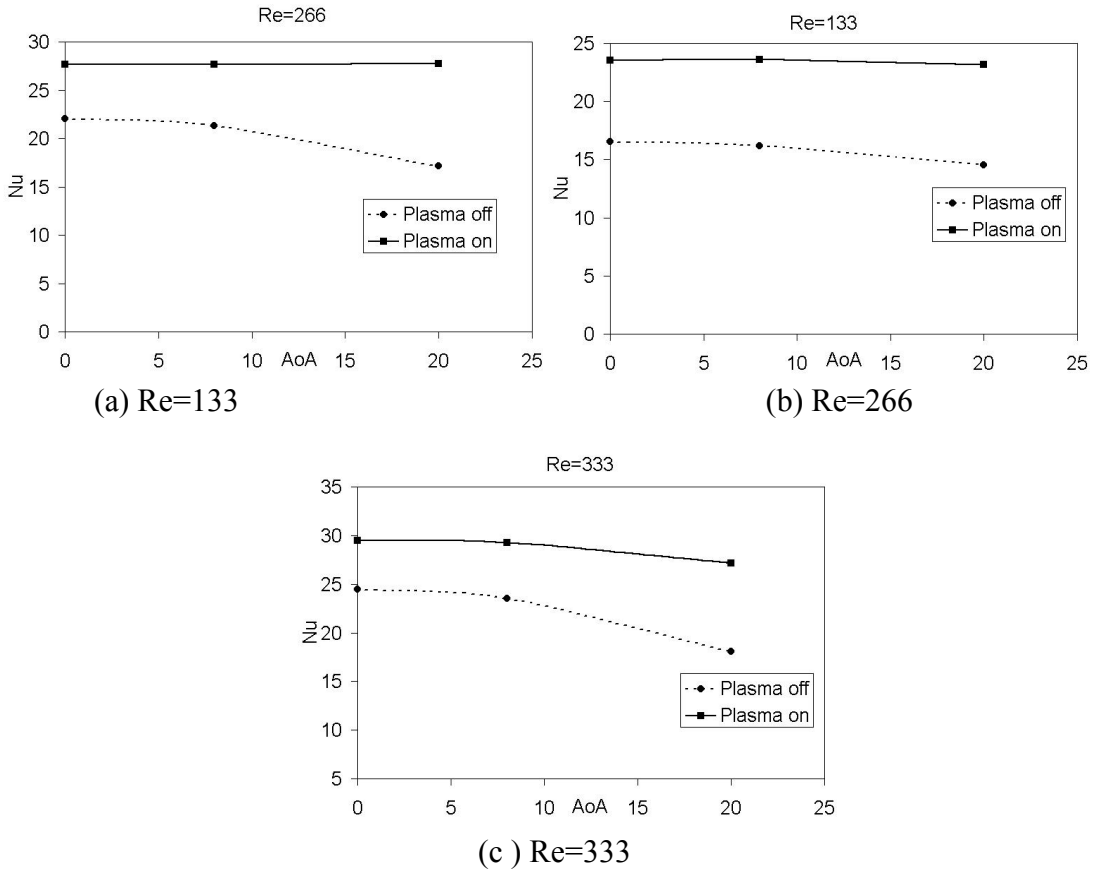


Figure 25 Nusselt number variation with angle of attack for various Reynolds number. The plasma is operated at 4KV rms and 3KHz frequency

Effect of electrode position on the flow: To investigate the effect of the electrode placement position on the flow, two positions (middle of the plate and at a distance of 10

percent length (of the plate) from the leading edge) were considered. The study was conducted for an angle of attack of 20-degrees and $Re=333$. Shown in Table 15 is a comparison of the aerodynamic and heat transfer data.

It appears that the effect of the electrode position on the drag is insignificant, as the observed data seem to be an artifact of the plasma body force. As summarized in Table 15, there are only minor changes in aerodynamics and heat transfer coefficients.

Table 15 Effect of electrode position on aerodynamic and heat transfer properties

Aerodynamic data	Electrode position		
	Middle	10%from leading edge	No plasma
Drag coefficient	1.0	1.0	0.124
Lift coefficient	1.22	1.12	0.636
Nusselt number	28.35	29.57	18.04

Figure 26 compares the streamlines of the flow over a flat plate, with $Re=333$ and an angle of attack of 20 degrees. Figure 26a representing the no plasma case shows a large flow separation. In Figure 26b the electrode is placed at the middle of the plate, while in Figure 26c, the electrode is closer to the leading edge. While the upstream placed electrode can more effectively eliminate the flow separation, both electrode locations produce very comparable outcome in aerodynamics and heat transfer. It seems that the overall impact of the glow discharge, namely, the induced wall jet is not sensitive to the details of the local flow structures for the Re considered, making the present device very attractive for active control. Similar, experimental observations have also been reported by Corke et al.[24-25]. In fact Corke et al, report efficient separation control at angle of attacks well past the stall angle. Also a typical plasma actuator with capacities

described above leads to substantial pressure recovery and also manifold increase in the lift to drag ratio.

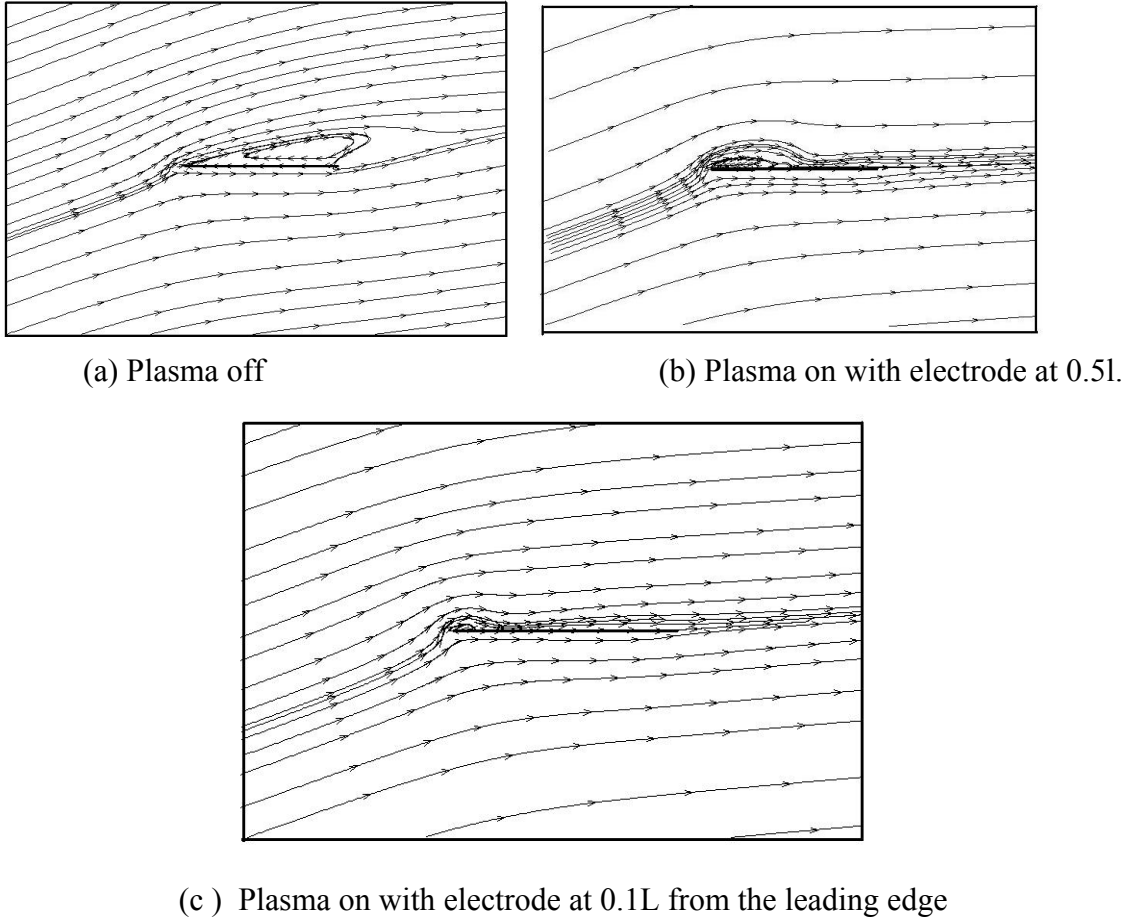


Figure 26 Streamlines showing flow separation for $Re=333$ and an angle of attack twenty degrees for different positions of the electrode

4.4 Self-Consistent Fluid-Model-Based Plasma Dynamics

The key to modeling DBD effects in fluid dynamics is to achieve realistic distributions of the species number densities and their momentum in the domain which interacts with the neutral fluid by solving the plasma-fluid equations along with the Poisson equation for the potential (Eqs. (2.39)-(2.45)). We will use a simplified form of the plasma model as present it below for convenience.

Continuity equation:

$$\text{Electrons: } \frac{\partial n_e}{\partial t} + \nabla \cdot (n_e v_e) = n_e S_{ie} - r n_i n_e \quad (3.26)$$

$$\text{Ions: } \frac{\partial n_i}{\partial t} + \nabla \cdot (n_i v_i) = n_e S_{ie} - r n_i n_e \quad (3.27)$$

Here, the source terms on the right hand side represent the reaction/ionization processes which result in the creation (S) or destruction (r) of the species, as applicable. It is very common to write the ionization coefficient S as a function of E/N.

Momentum equation: The momentum equation for the species at high pressures can be reduced to the drift diffusion form which neglects the inertial and unsteady terms and balances the thermodynamic pressure gradient with the drift force and collision terms.

$$\text{Electrons: } n_e \mu_e E - \nabla (n_e D_e) = n_e v_e \quad (3.28)$$

$$\text{Ions: } n_i \mu_i E - \nabla (n_i D_i) = n_i v_i \quad (\text{for high-pressure discharges}) \quad (3.29)$$

Electric field equation: The electric field E is obtained using the solution of the Poisson equation, given by

$$\nabla \cdot (\epsilon_d E) = \frac{e(n_i - n_e)}{\epsilon_0} \quad (3.30).$$

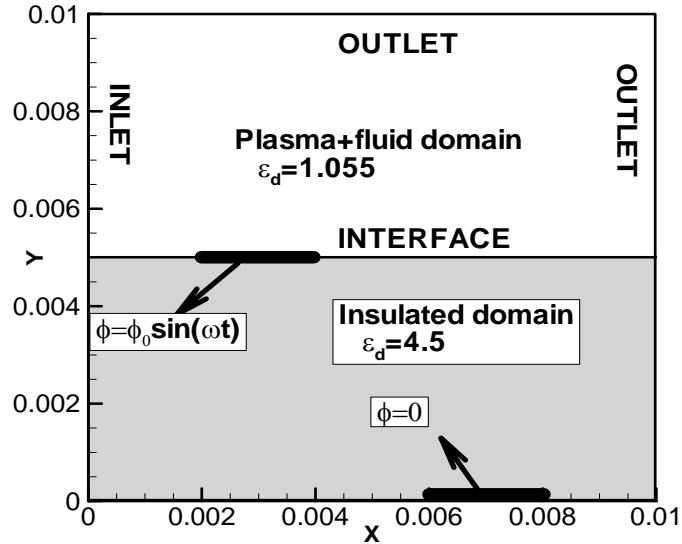
The solution algorithm employed has been discussed extensively in the previous chapter.

4.4.1 Discharge Actuator Setup

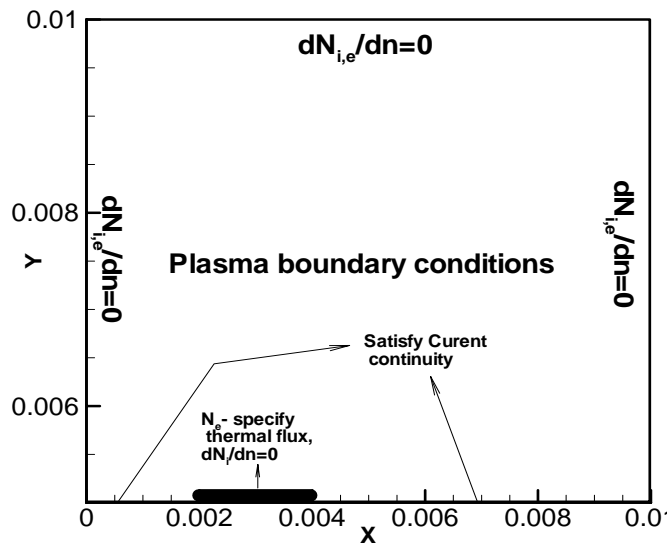
In this section, we will model the two-dimensional radio frequency dielectric barrier discharge (DBD) in helium gas at high pressure in an asymmetric configuration as shown in Figure 27 .

The electrodes are 2mm in length and the insulated bottom electrode is shifted downstream by 2mm. A similar case has been studied by Roy et al.[15]. The helium discharge is modeled at a pressure of 300 Torr, and a temperature of 300K and is driven by an AC voltage of 1 KV (peak voltage) operating at 5 KHz. The thickness of the

electrodes is negligible and the dielectric thickness is 5 mm. The electron temperature is assumed to be 1eV (~11600K), while the ions and the neutrals are essentially in thermal equilibrium at 300K. The various transport properties and property relationships are available in literature and we will use the ones used by Roy et al.[15] for the present study. These are summarized in Table 16.



(a) Complete domain with insulator indicating boundary conditions for fluid flow



(b) Top half of the domain indicating boundary conditions for plasma species and the region where the results are presented.

Figure 27 A representative 2-D asymmetric discharge arrangements

The computational domain employed is a square domain of size 1cm x 1 cm x 1 cm (unit cm in the normal or spanwise direction). The grid consists of 127 x 61 points for the 2-D case as is shown in Figure 27b. The dielectric constant in the fluid/discharge domain is 1.0055; the permittivity of vacuum and that of the insulator is 4.5. For investigation purposes two different frequencies are considered, namely, 5 KHz and 10 KHz, respectively, with all other conditions remaining constant. A global time-step of 10^{-8} s is used for the computations. The initial number density in the plasma is $1.0 \times 10^{15} / \text{m}^3$ for all the different species.

Table 16 Summary of property models employed for the He discharge simulation.

Transport/reaction properties	Models/values employed
μ_i (ion mobility)	$= \frac{8 \times 10^3}{p} (1 - 8 \times 10^{-3} E/p) \text{ cm}^2 \text{ V}^{-1} \text{ s}^{-1} \text{ for } E/p \leq 25 \text{ V cm}^{-1} \text{ torr}^{-1}$
	$= \frac{4.1 \times 10^4}{p \sqrt{E/p}} \left(1 - \frac{27.44}{(E/p)^{1.5}} \right) \text{ cm}^2 \text{ V}^{-1} \text{ s}^{-1} \text{ for } E/p > 25 \text{ V cm}^{-1} \text{ torr}^{-1}$
μ_e (electron mobility)	$= \frac{e}{m_e \nu_{en}} \text{ cm}^2 \text{ V}^{-1} \text{ s}^{-1} \text{ where } \nu_{en} = 10^{12} / \text{s}$
S_{ie} (species ionization model)	$= 4.4 \exp \left(\frac{-14}{(E/p)^{0.4}} \right) p \mu_e E \text{ s}^{-1}$
r (recombination coefficient)	$= 1.09 \times 10^{-20} T^{-9/2} n_e \text{ m}^3 / \text{s}$
D_i (ion diffusivity)	$= 500 \text{ cm}^2 / \text{s}$
D_e (electron diffusivity)	$= \frac{kT_e}{e} \mu_e \text{ cm}^2 / \text{s}$
μ (viscosity of He gas)	$= 2.0 \times 10^{-5} \text{ N s} / \text{m}^2$

Note: Data presented is the same used in [15].

4.4.1.1 Boundary condition

The boundary conditions are schematically presented in Figure 27b. The homogeneous Neumann boundary condition is applied for the electrostatic potential at the open boundaries while the Dirichlet boundary condition is used at the electrode:

- At the exposed electrode: $\phi = \phi_0 \sin(2\pi ft)$, where ϕ_0 is the peak value.
- At the submerged electrode: $\phi = 0$

For the plasma species modeling, the domain boundary away from the insulator/electrode surface is assigned a zero gradient condition assuming insignificant impact far away from the fluid-actuator interface. At the dielectric surface, the drift current and the displacement current from the gas domain is balanced with the displacement current inside the insulator. At the electrode, the treatment is slightly different. The electrons are assumed to be isothermal (at 11600K or 1eV) at boundaries. At the exposed electrode, the thermal flux towards the wall is considered while it is neglected when the drift is away from the wall. For the ions or the heavier species, the drift effects are significant and hence a zero gradient condition ($\frac{\partial n_i}{\partial n} = 0$) is applied. The boundary conditions are summarized in Table 17.

4.4.1.2 Plasma species initial condition

The initial condition used to start the simulation requires specifying the starting number densities for the various species. Ideally the simulation should start from a very small charge concentration, but to accelerate the evolution of the transient behavior to a periodic steady state solution we will use a weakly preionized neutral concentration of $10^9 / \text{cm}^3$. To look into the sensitivity of the solution to the initial guess we look at two initial guesses of 10^{10} , $2.5 \cdot 10^{10} \text{ cm}^{-3}$. We will use a high frequency of 20 KHz and 1 KV acting on the geometry in Figure 27a for the present discussion. Solutions are compared after 70 time-cycles at which time a periodic steady state has been attained as shown in Figure 28. There is a significant difference in the domain averaged number-density values, but the net charge densities and the resulting force field seem to be much closer to

each other for the two initial guesses as the solution approaches a periodic steady state solution. This shows that the dynamics of the operating discharge plasma actuator is only a function of the difference in the values of Ni-Ne or more generally the net charge in the region. The dependence of Ni and Ne on the initial guess is simply due to the non-linear nature of the recombination term in the transport equation (Eq (3.26),(3.27)). It was observed that the periodic steady state solution was attained much quicker with a starting guess of $10^9/\text{cm}^3$ and was used as the initial condition for the results presented in the rest of the discussion.

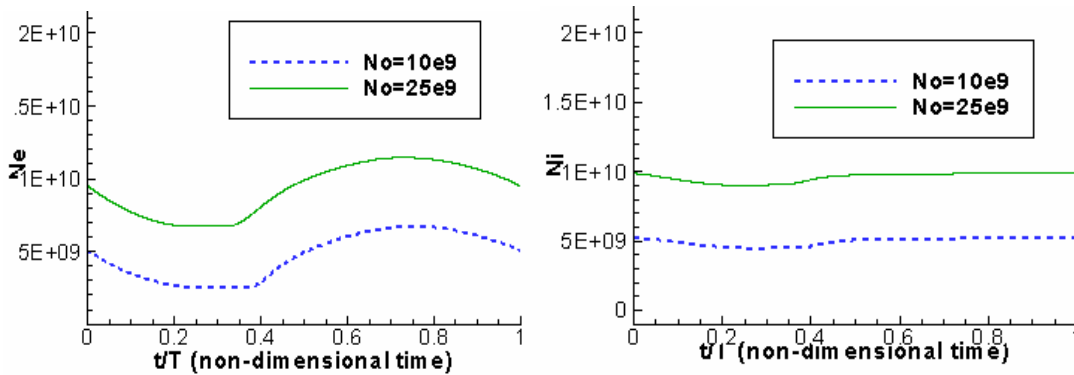
Table 17 Summary of boundary conditions for the different variables

Variable	Open boundary	Electrode/dielectric surface
ϕ - potential	Zero gradient	<p>At the submerged electrode: $\phi = 0$.</p> <p>At the exposed electrode: $\phi = \phi_0 \sin(2\pi ft)$, $\phi_0 = 1KV$</p> <p>The dielectric is not a boundary for the potential.</p> <p><u>Electrode:</u></p> <p><u>Electrons:</u></p> <p>Away from the electrode: flux=0</p> <p>If drift is toward the electrode: flux=$N_e V_{eth}$, where V_{eth} is the thermal flux .</p>
Electron,Ion species	Zero gradient	<p><u>Ions:</u></p> <p>Away from the electrode: flux=0</p> <p>If drift is toward the electrode: Zero gradient</p> <p><u>On the dielectric:</u></p> <p>Allow surface charge accumulation. To do this the current continuity is established.</p> <p>i.e. At the dielectric-gas interface the species flux is determined by</p> $\frac{\partial(\epsilon_{gas} E_{gas})}{\partial t} + \frac{e}{\epsilon_0} (N_i V_i - N_e V_e)_{gas} = \frac{\partial(\epsilon_{dielectric} E_{dielectric})}{\partial t}$

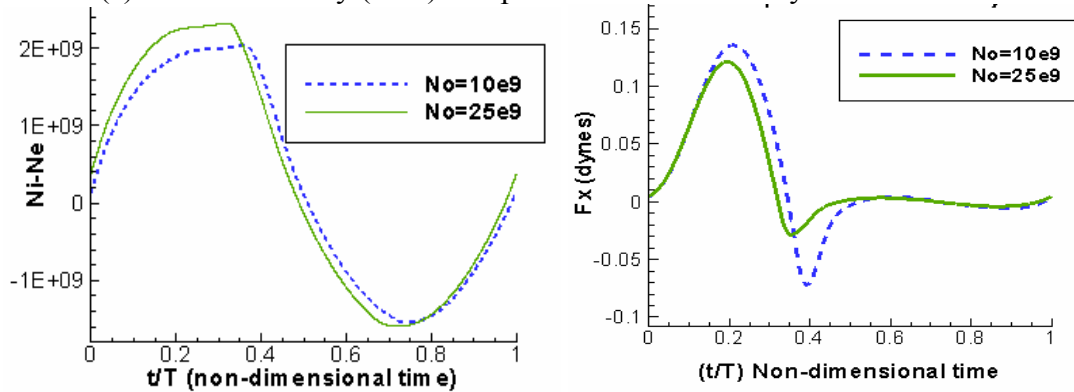
4.4.2 Plasma Structure

In the following discussion we will analyze the discharge structure in space and time with reference to the experimental observations. The experimental results which we will present here are for qualitative comparison purposes and were run with air as the

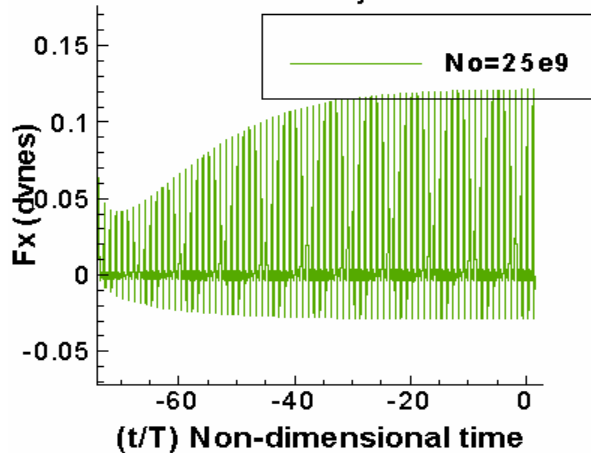
working gas using an applied voltage of 6KV and 2.5 KHz frequency. The numerical simulation shown is for 1KV and 5 KHz applied signal for the configuration described above in Figure 27b and is based on Helium as the working gas. This discussion will shed some light into the operating mechanism of the actuator.



(a) Number density (cm⁻³) comparison after 70 time cycles



(b) Ni-Ne (cm⁻³) and Fx comparison after 70 time-cycles
Time history of Fx



(c) Time history of Fx integrated over the domain

Figure 28 Sensitivity to initial condition (20KHz, 1KV applied voltage)

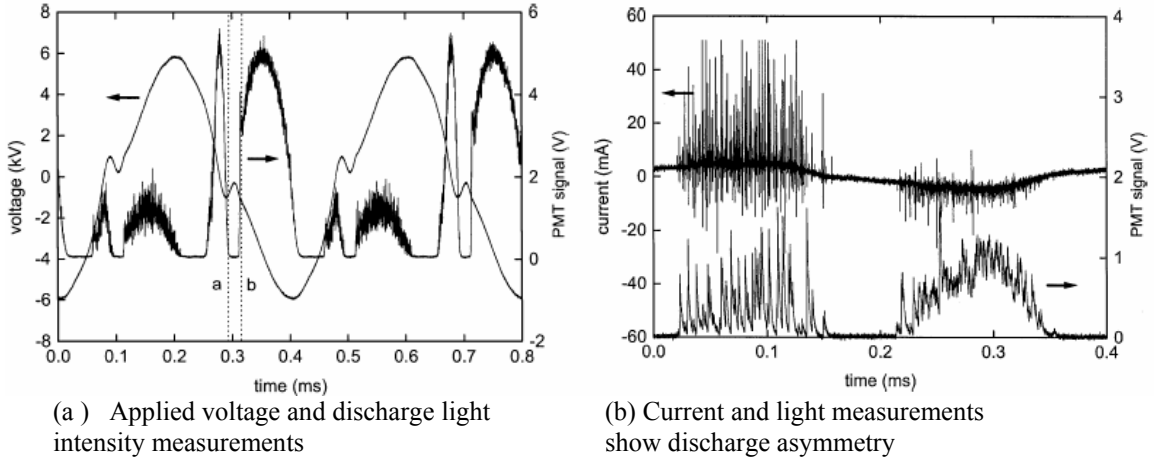


Figure 29 Photo intensity measurements of Enloe et al.[21](pictures reproduced for this discussion) in trying to depict the observed discharge evolution over a time-cycle.

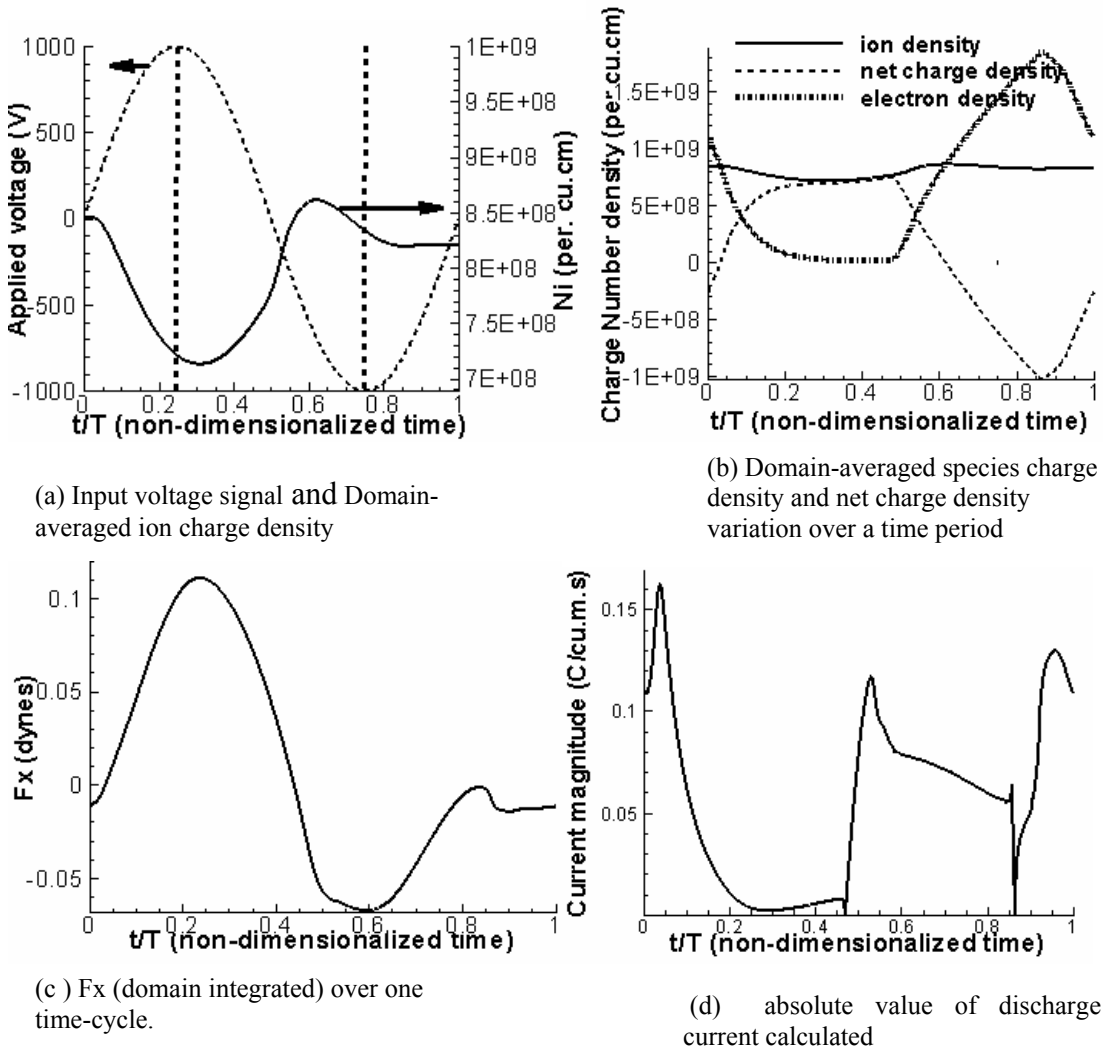
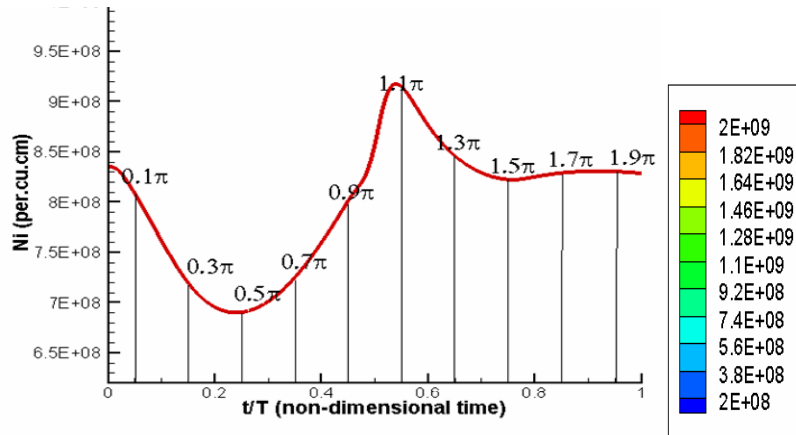


Figure 30 Time dependent plasma behavior (5 KHz, 1KV applied voltage)

Figure 29 shows the experimentally observed light intensity measurements of Enloe et al.[21] to depict the observed discharge evolution over time for an asymmetric plasma actuator. While the light intensity measurements cannot be directly compared to the numerically calculated quantities, we will comment on some of the key qualitative features in the observed results.



(a) Domain-averaged ion number density (per cu.cm) over time.

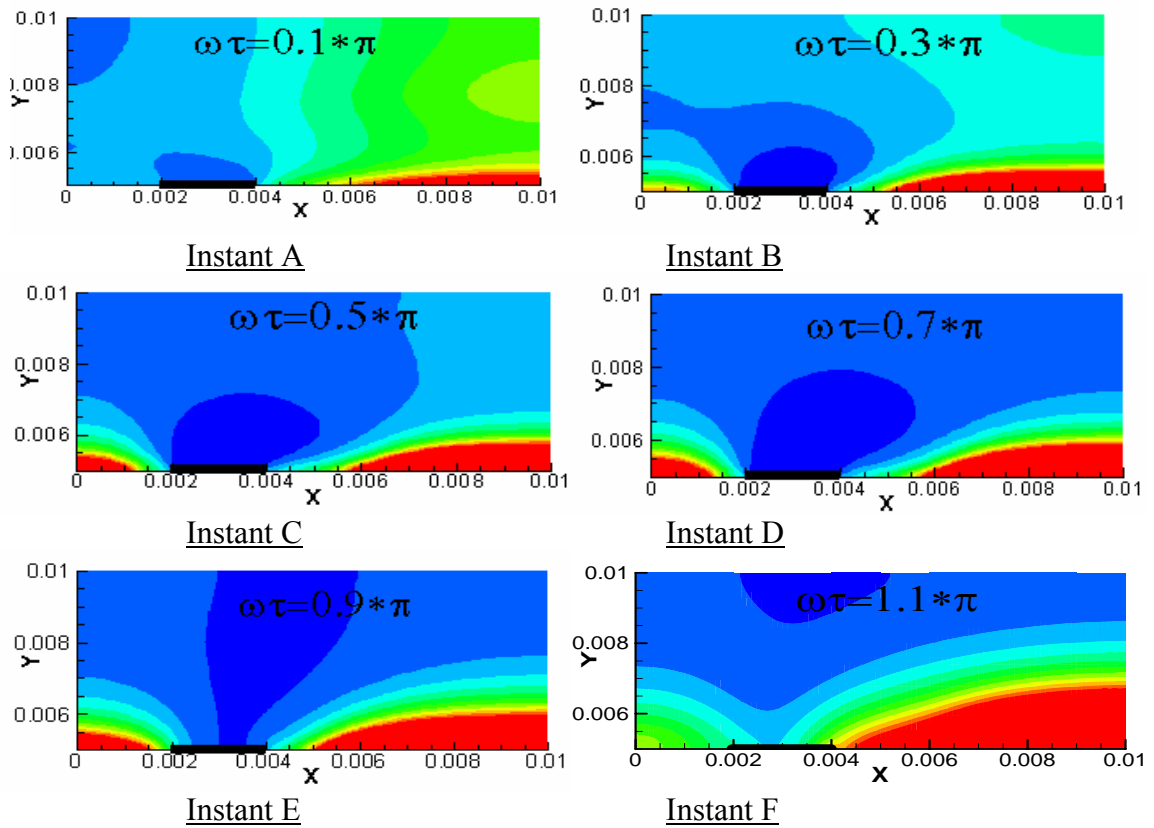
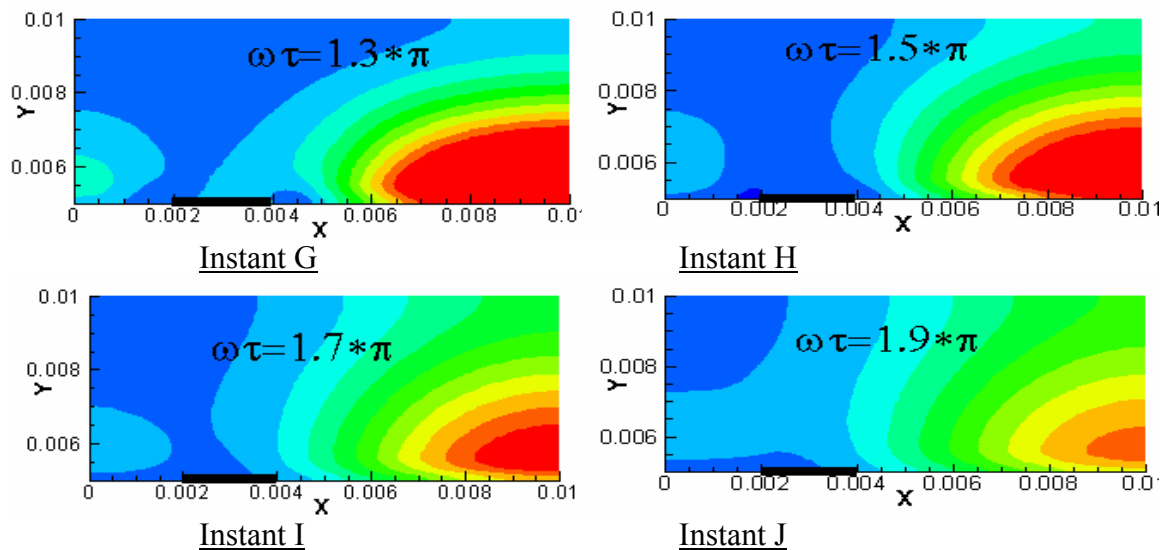
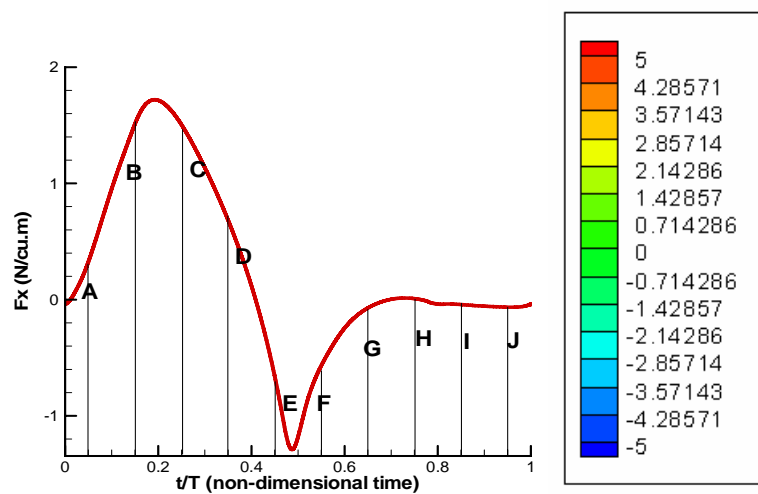


Figure 31 Ion density evolution in the domain over time (5 KHz, 1KV applied voltage)



(b) Instantaneous snapshots of the ion density at different instants over a cycle.
Figure 31. Continued.



(a) Domain averaged force (N/cu.m) variation in time

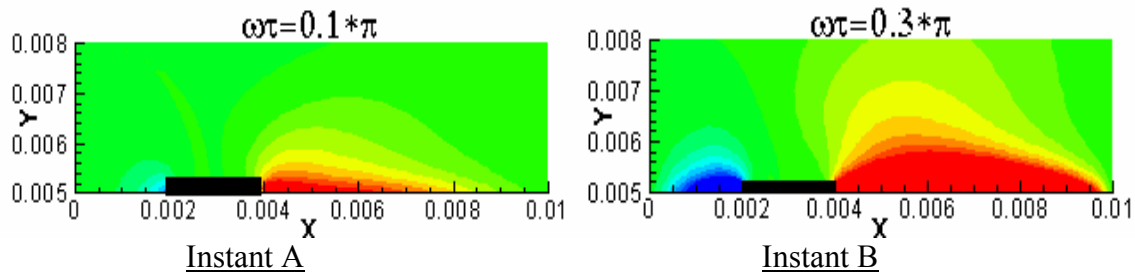
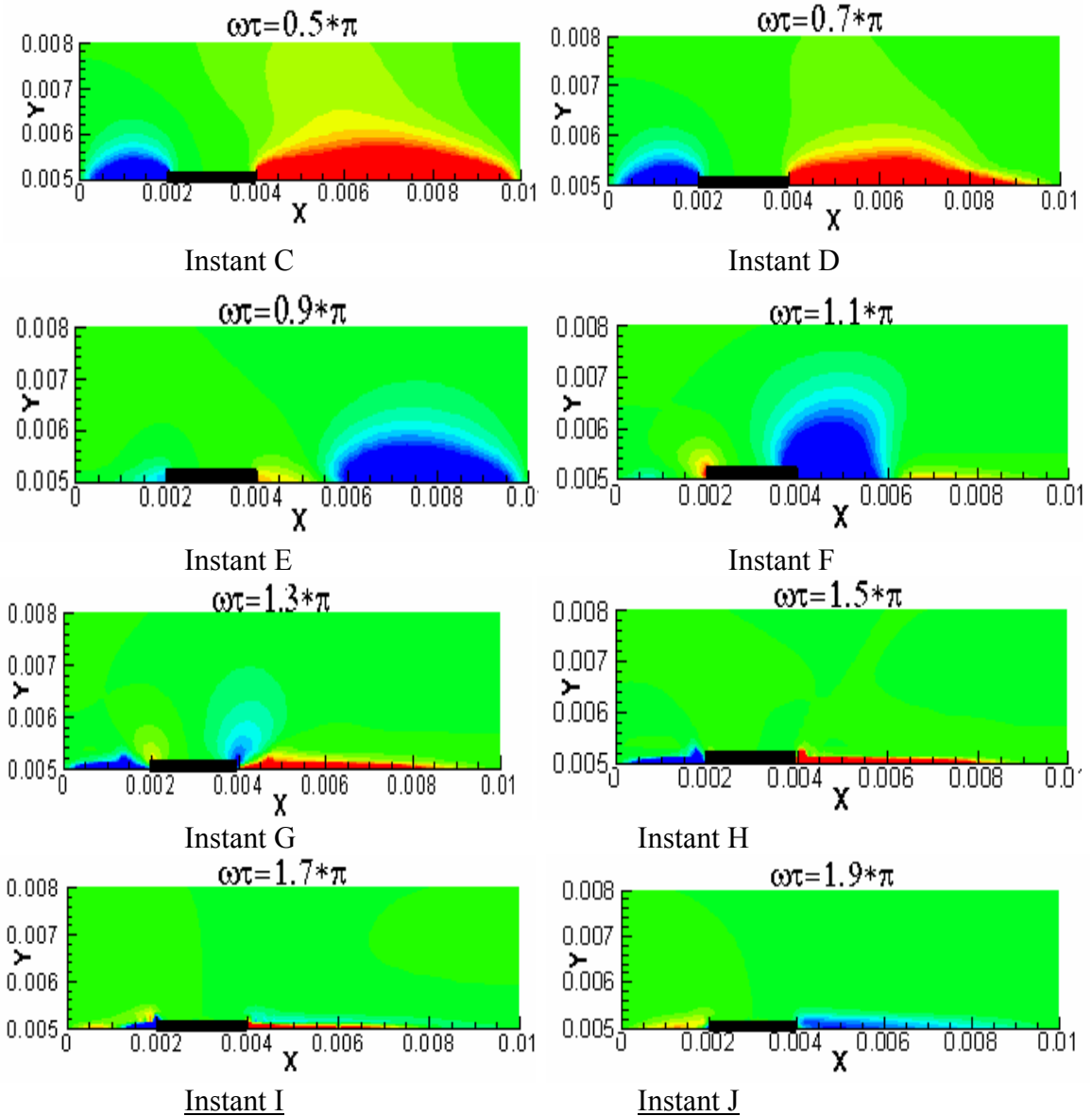


Figure 32 Force evolution over one time cycle (5 KHz, 1KV applied voltage)



(b) Instantaneous snapshots of the force field at different instants over a cycle.
Figure 32. Continued.

Self-limiting Discharge: It is commonly believed that the breakdown is quenched and controlled by the accumulated charge since the discharge terminates on a dielectric surface and hence the self-limiting nature of the discharge. This can be observed from the experimental results in Figure 29a where a continuously varying applied voltage is necessary to sustain the discharge. Here, the light intensity observed is zero as soon as the observed potential reaches either maxima or minima. This phenomenon can be observed

in the numerical results as well. Figure 30a and b show the mean density variation in time for the different species and the net charge density. It is known that in the positive half-cycle the ions move away from the electrode and tend to get deposited on the surface. Hence the decrease in the average ion density over the domain as the averaging process doesn't account for the surface deposition. Similar to the experimental observation this decrease in ion density is stopped when the increase in voltage is zero near the maxima. This can be clearly seen in the evolution of the ion density in the domain as shown in Figure . Specifically in the first quarter of the time-cycle as can be seen in instants A,B and C, the ion concentration really accumulates near the dielectric surface and the free concentration in the domain at its minimum. At instants D, E and F, the applied voltage starts decreasing causing the built up potential from the accumulation to dominate resulting in releasing the ion species into the bulk region. The ion density reaches its maximum value at instant F. At this point the change in polarity enhances the release of ions which travel towards the negative exposed electrode. However, there is no ion build-up during this part of the cycle as the electrode being a conductor absorbs the incoming charge flux. At instant G(1.5π), Figure a shows the ion number density as stabilizing due to the equilibrium attained between the absorption at the electrode and the accumulated ion release from the insulator surface. This behavior continues for the rest of the cycle.

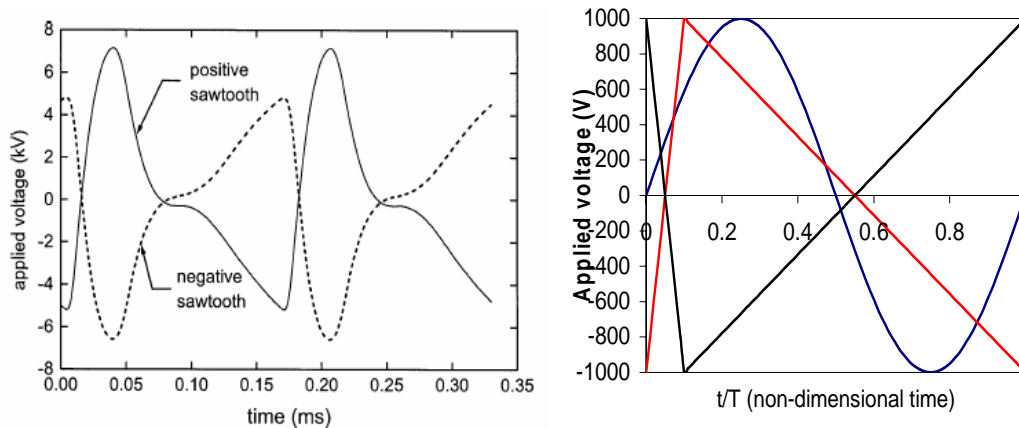
Force variation: As seen from the current measurements (Figure 29b and [21]) much larger fluctuations are observed for the positive half-cycle. The corresponding domain averaged force variation in time presented in Figure a shows that the positive-half cycle is more efficient and has a predominantly positive force, while the less efficient negative half-cycle has both positive and negative components. This is clearly seen from the

evolution of the force field over time as shown in Figure b. It is well known that the bulk of the momentum transfer is achieved by the heavier ion species ion species in the domain. As can be seen from Figure b, the positive half-cycle corresponding to instants A,B,C,D and E correspond to the accumulation of ion species on the insulator surface from the bulk of the domain. Since the submerged electrode is downstream, the bulk of the transport in this half is in the positive direction and to a lesser extent in the negative direction. Hence the strong positive force regions near the insulator surface downstream of the electrode and a weaker component upstream of the electrode for instants A,B,C and D as seen in Figure b. Starting from instant E at which time the charge build-up reverses the polarity of the potential in the region. This happens for half a cycle corresponding to instants E and F during which the weak negative force region near the downstream insulator surface exits due to the ion transport towards the upstream electrode. An interesting phenomenon happens at this instant in the cycle. It should be noted that during this half that the electrons are the species which get accumulated on the dielectric surface resulting in the charge build-up. However, the electrons being lighter species travel faster and hence the faster charge build-up and a quicker reversal of polarity in the domain. There is the qualitative similarity between the instants G,H, I and B,C,D in Figure 32b, but the process is only more quicker. The above mechanism renders the force weaker in this negative half, as the discharge is quenched early. This force generation efficiency is of importance here as the slower response time of the fluid will only see the net overall force generation over a few time-cycles and is less sensitive to the fluctuation over time.

Asymmetry in the discharge: The above discussion on the time evolution of the force field indicates two totally different mechanisms in the two half-cycles. The first half-cycle shows a pure ionization and deposition of the slower ion species on the insulator surface while the second half-cycle shows the exactly similar behavior for the electrons but at a faster rate. This difference in the mobilities of the two species and the geometric asymmetry totally alters the discharge evolution in the second half-cycle. This asymmetry can be observed in the experimental measurements as well. The light intensity measurements Figure 29a and Figure 29b show that the intensity measured over the two half-cycles are distinctly different. Comparing with the voltage waveform, it can be seen that the discharge light emission is irregular in the positive going half-cycle and is more uniform in the negative going half-cycle. It would be useful to establish a correlation between the observed light intensity measurements from the experimental study and the net charge variation shown in Figure 30b. Specifically, the strength of the light intensity measurement over the time-cycle follows the same trend as the absolute value of the time rate of change of the net charge ($N_i - N_e$) in the domain, given by $\left| \frac{d(e(N_i - N_e))}{dt} \right|$. While this may sound arbitrary at first, further insight reveals that this time derivative measure is equivalent to the discharge current from the domain. As Figure 29b from the experimental study shows, the light intensity measure follow the same trend as the magnitude of the discharge current. While not relevant in the present study, the above discussion leads us on to another key aspect which will determine nature of the force field and the momentum coupling. This is the presence of the negative ions and other charged species by including much more extensive chemistry as in the case of atmospheric air modeling. Since, the discharge current variation over time is heavily

dependent on the mobility of the different charged species; the presence of negative ions will significantly alter the discharge evolution in time.

Impact of Voltage Waveform: The observed behavior for the harmonic waveform indicated that the positive going half (irregular) had a different discharge characteristic as compared to the negative going half (uniform discharge) leading to the asymmetry which causes the uni-directional momentum coupling with the fluid flow. Also, in the earlier discussion the positive sawtooth waveform has a much faster positive-going and a slower negative going cycle. The negative sawtooth has a faster negative going and slower positive going cycle.



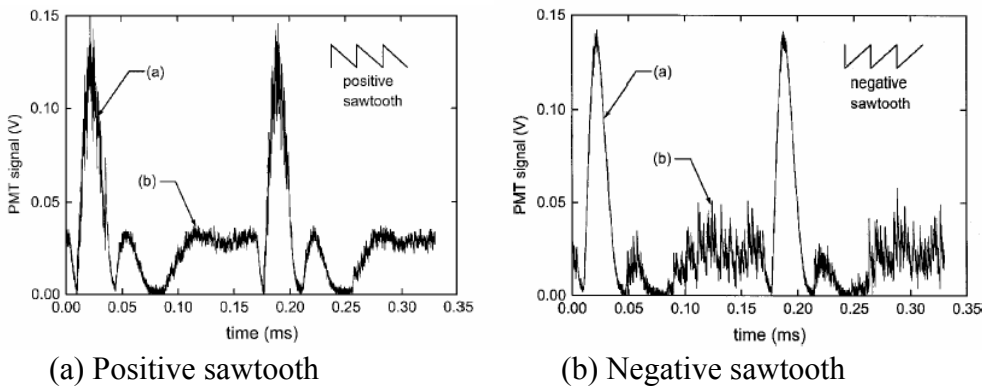
(a) Input sawtooth voltage signal
(7KV, 5.8 KHz) reprinted from Enloe
et al. [211]

(b) Different input voltage signals
(1KV, 10 KHz) used in the numerical study

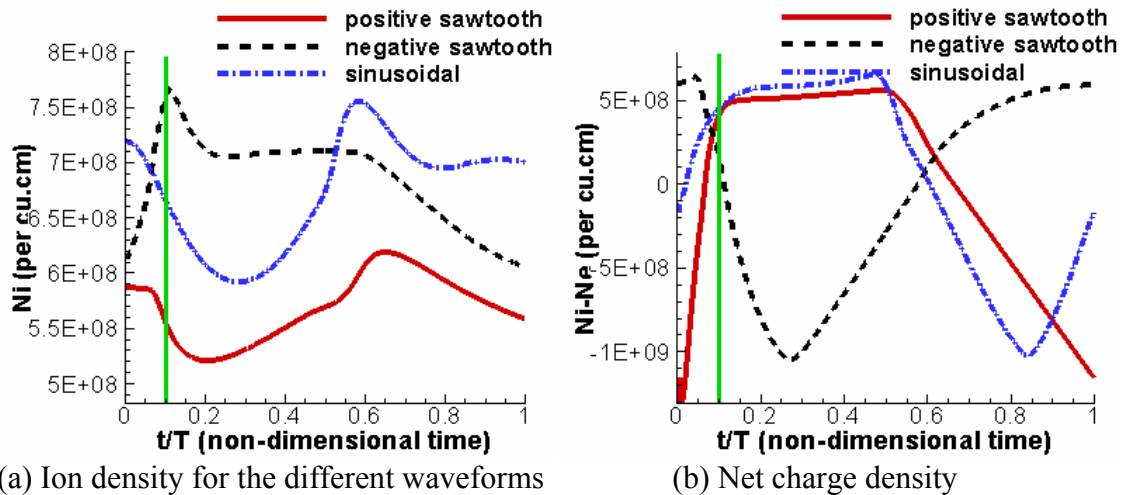
Figure 33 Asymmetric sawtooth voltage waveforms used in the experimental and numerical studies

For both waveforms faster voltage variation results in stronger discharge intensities. The positive sawtooth (Figure 34a) waveform has a stronger positive-going phase which results in an irregular discharge for the stronger peak. Negative sawtooth (Figure 34b) has a weaker positive-going phase and hence the irregular weak discharge is seen for a longer time.

As discussed in the earlier section, the light intensity can be directly correlated to the discharge current or $\left| \frac{d(e(Ni - Ne))}{dt} \right|$. The ion density (Figure 35a) and the net charge density variation (Figure 35b) are shown in Figure 35. As mentioned, the maximum slopes are observed for the two sawtooth waveforms in the early part of the cycle as compared to the harmonic waveforms are much larger.



(a) Positive sawtooth (b) Negative sawtooth
Figure 34 Experimental results of Enloe et al. [21] comparing the discharge observed from the two different sawtooth waveforms (pictures reproduced from [21] for this discussion)



(a) Ion density for the different waveforms (b) Net charge density
Figure 35 Impact of waveform on the species number density

Efficiency of the Waveform: Enloe et al. [21] measures the thrust produced by the actuator for both the above sawtooth waveforms using a mass balance ([21]) to assess efficiency of the two half-cycles. The positive sawtooth has a faster varying positive

going voltage and a slower varying negative going voltage and vice versa for the negative sawtooth.

The experimental thrust measurements in Figure 36 clearly shows that the positive sawtooth is more efficient compared to the negative sawtooth waveform. This is because unlike the light intensity measurements, the force orientation tends to depend heavily on the geometric asymmetry and hence strongly dependent on the polarity of the exposed and the submerged electrodes. On the other hand the magnitude of the force is a function of the strength of the discharge and charge concentration available in the domain. The positive sawtooth has a stronger positive going part which results in a strong breakdown while the negative sawtooth has a stronger negative going part. One can infer from the force response to the harmonic waveform (Figure a) that the positive going part (exposed electrode is positive) is possibly more efficient than the negative going part. The domain-averaged force responses for the sawtooth waveforms are shown in Figure 37. The force for the positive and negative sawtooth waveforms starts the time-cycle in similar fashion with negative slope. For the negative sawtooth, the force continues on its negative slope and attains a negative peak during the fast varying early phase (negative-going voltage) and then steadily increases to a positive value during the slow-varying positive-going phase. Table 18 shows the time-average value of the force in the domain for the three different waveforms. The harmonic waveform seems to be the most efficient waveform. The negative sawtooth is the least efficient with the positive sawtooth falling in between. The force profile over time indicates that the positive going phase is the most efficient part of the voltage cycle for the asymmetric actuator modeled in this study.

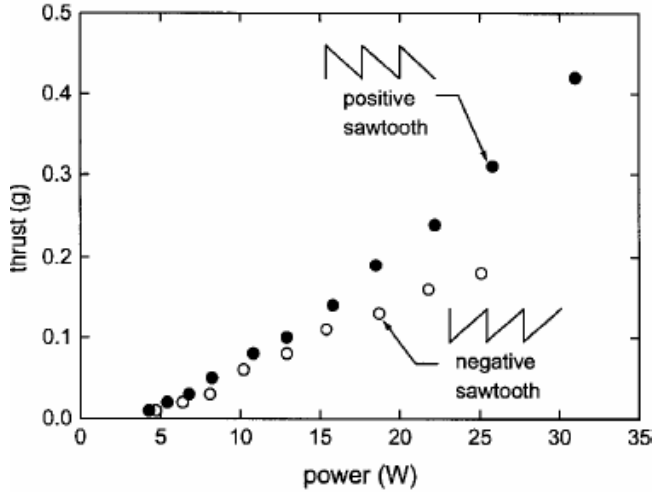


Figure 36 Thrust measurements of Enloe et al. (reproduced with permission from [22]) showing the positive sawtooth waveform as being more efficient

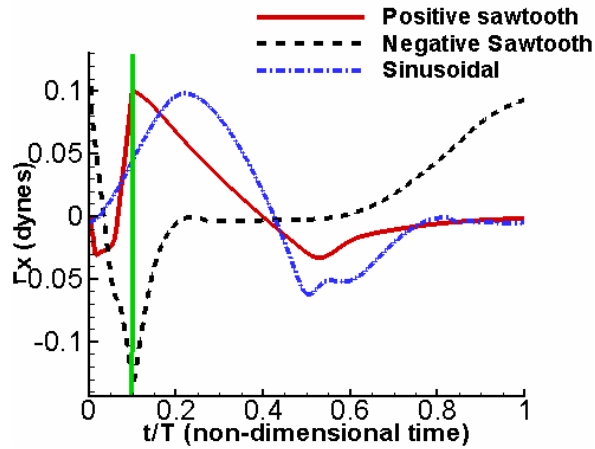


Figure 37 Axial force integrated over the domain with time (F_x (dynes)) for different waveforms (10KHz, 1KV applied voltage). The green vertical line indicates the instant of change in slope in the sawtooth waveform.

Table 18 Domain averaged force over the voltage cycle for different waveforms

Waveform	Average force over the cycle (dynes)
Positive sawtooth	0.0068
Negative Sawtooth	0.0063
Sinusoidal	0.0081

4.4.3 Geometric Effects

4.4.3.1 Impact of electrode spacing

The asymmetry observed in the earlier discussion seems to be heavily orchestrated by the asymmetry in the geometry. So to investigate this we looked at three

different geometric constructions as shown below. The discharge was generated by a 20KHz, 1KV sinusoidal applied voltage waveform.

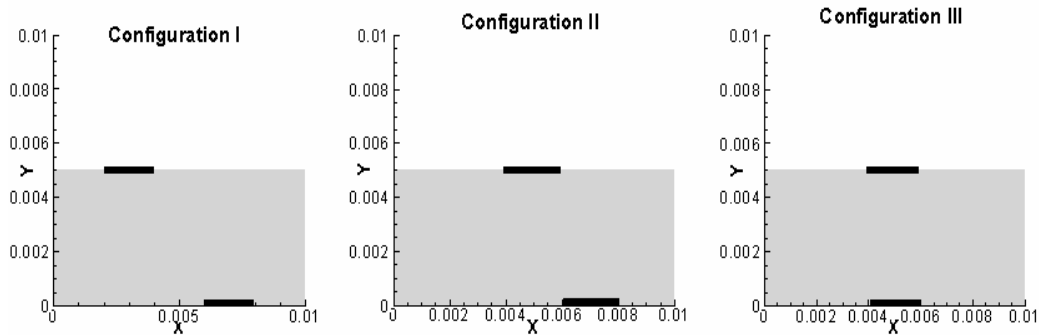


Figure 38 3-Different configurations to study the impact of electrode overlap

Configuration I has two electrode lengths (2*2mm) horizontal separation between exposed and submerged electrode centerlines. Configuration II has a one electrode separation and configuration III has zero separation.

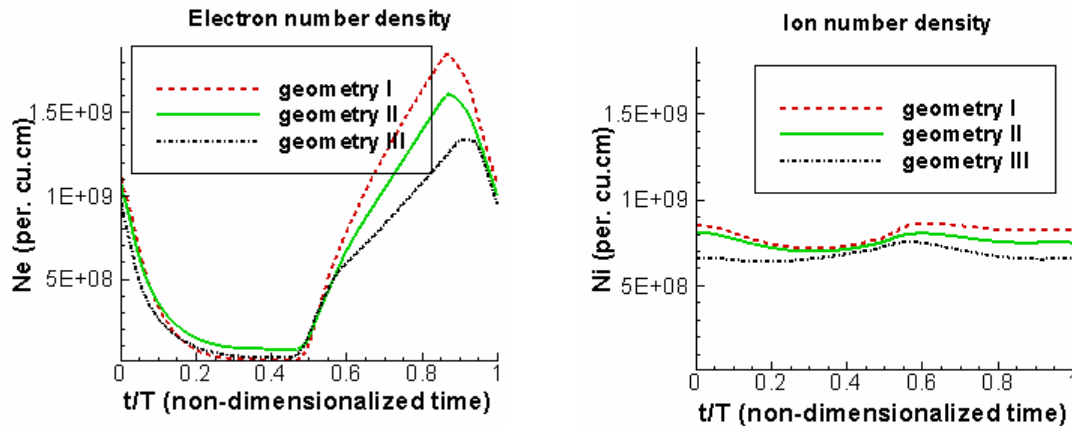


Figure 39 Time evolution of species number density over one time-cycle (20KHz, 1KV voltage signal)

Based on the observed average force values obtained in Table 19, it looks like configuration II is the most efficient while configuration III is the least efficient. Configuration I and II both display strong asymmetry in the domain averaged force over the time-cycle. It can be observed that configuration I results in a weaker average force and that there might exist an optimum gap which gives the best performance. This

asymmetry tends towards a more symmetric force variation in time as the electrode gap is reduced. Configuration III being the symmetric arrangement shows a symmetric variation over time. While the force in itself shows a smaller value as compared to the other cases, the symmetry enhances the overall time-averaged force in the domain.

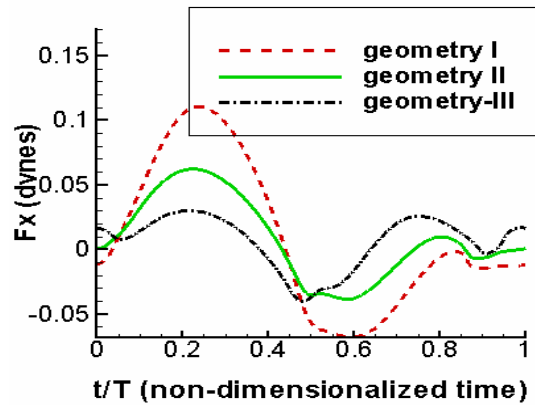


Figure 40 Impact of the geometric configuration on the domain integrated force field (20KHz, 1KV voltage signal)

Table 19 Domain averaged force over the voltage cycle for different configurations

Geometry	Average force over the cycle (dynes)
Configuration I	0.0071
Configuration II	0.0087
Configuration III	0.0065

4.4.3.2 Impact of lower electrode size

Here we fix the length of the top electrode and vary the bottom electrode to gauge the impact of the area covered by the net surface discharge formation. The actuator operates using a 20KHz, 400 V sinusoidal voltage waveform. Figure 42 and Table 20 indicate that the weakest force field is obtained for the 2mm electrode case while there is steady increase in the net force value as the size of the bottom electrode increases. This effect is because the larger lower electrode obviously results in a much larger surface discharge generation and hence the stronger force field. However, once the lower electrode becomes sufficiently large, a balance between size and strength will be reached

signifying the most efficient configuration. Similar trends have been observed by experimental studies such as by Enloe et al.[22].

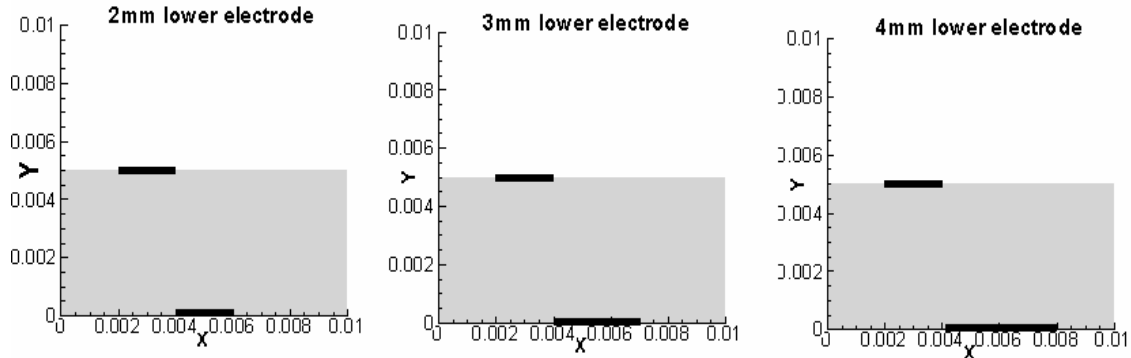


Figure 41 Three different lower electrode lengths modeled to investigate the effect of increased surface area on the discharge

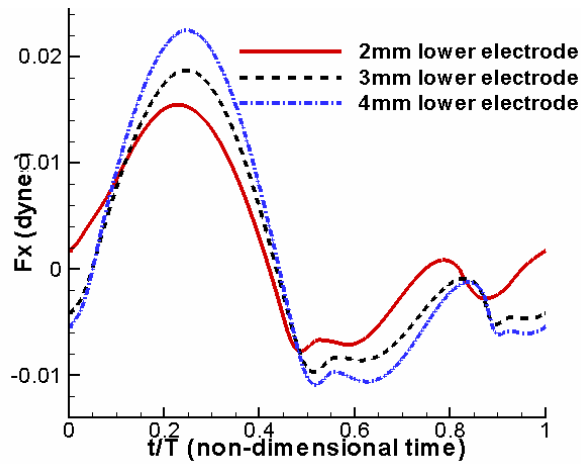


Figure 42 Impact of lower electrode size

Table 20 Force dependence on the lower electrode size

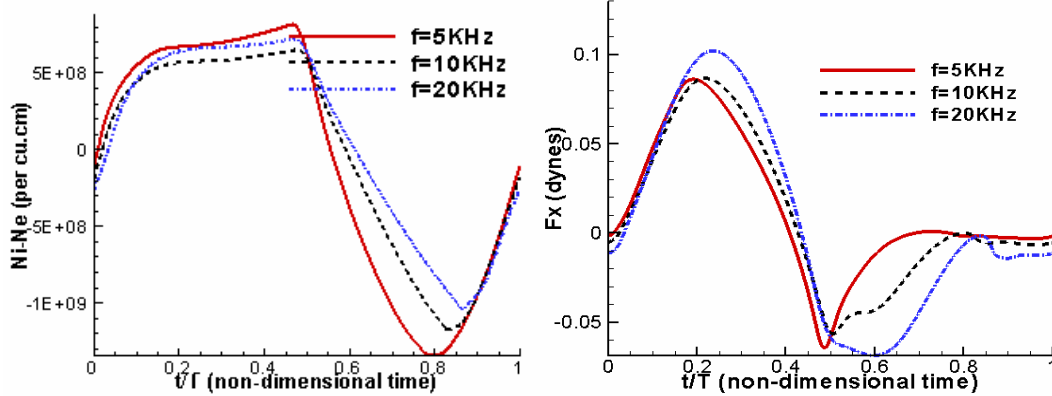
Lower electrode size	Average force over the cycle (dynes)
2 mm	0.00023
3 mm	0.00065
4 mm	0.0010

4.4.4 Impact of Applied Voltage and Frequency

The frequencies used were 20KHz, 10 KHz and 5 KHz with a voltage of 1KV.

The voltages used were 1KV, 500V, 400V and 250 V with a 20KHz frequency.

4.4.4.1 Frequency sensitivity

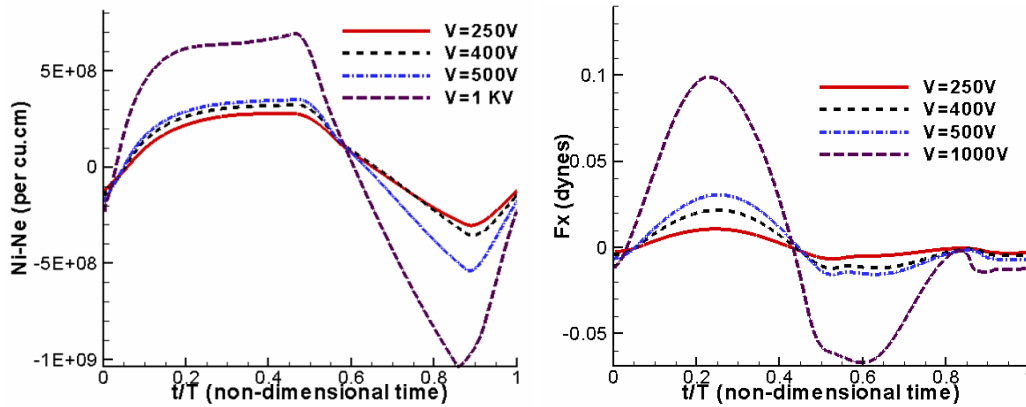


(a) Averaged net charge density (b) Averaged horizontal force component
Figure 43 Charge density and force variation over time for different frequencies

The 5 KHz frequency case seems to show a much larger fluctuation (Figure 43a) in the net charge (over the full time-cycle) as compared to the higher frequencies. This is because the smaller frequency enables the charge in the domain to completely settle down on the insulator surface before voltage reversal occurs. This surface charge accumulation might not be so complete for the higher frequencies. The incomplete accumulation of the charge on the insulator surface for higher frequencies in the force variation over time is shown in Figure 43b. The 5 KHz frequency case shows a sharp transition of F_x upon voltage reversal indicative of charge release from the insulator surface. On the other hand, the higher frequency cases display a slower transition from the negative value in the domain till it stabilizes to a value near zero. The 5 KHz frequency apparently shows a more efficient time-cycle as compared to the higher frequencies. But this can be misleading, since the corresponding duty cycle is much larger. In other words, one cycle of the 5 KHz frequency actuator is equivalent to 4 cycles of the 20 KHz actuator in time and hence will have a stronger impact when acting on a slower process.

Table 21 Domain averaged force over the voltage cycle for different frequencies

Frequency	Average force over the cycle (dynes)
20 KHz	0.0059
10 KHz	0.0095
5 KHz	0.0125



(a) Averaged Net charge density

(b) Averaged horizontal force component

Figure 44 Charge density and force variation over time for different voltages

Table 22 Mean domain averaged force over the time cycle for different voltage

Voltage	Average force over the cycle (dynes)
250 V	0.0008
400 V	0.0017
500 V	0.0026
1000 V	0.006

4.4.4.2 Applied voltage sensitivity

The force shows a power-law dependence on the applied voltage. i.e. $F_x \propto V^{2.1}$. In Figure 45 three different force measurements are compared for their voltage. The experimental (work of Van Dyken et al.[26]) and the phenomenological model data are the same as shows in Figure 21. It can be seen from the figure that all three sets of data corresponding to the plasma-fluid model, empirical approach and the experimental measurements indicate comparable dependence on the applied voltage.

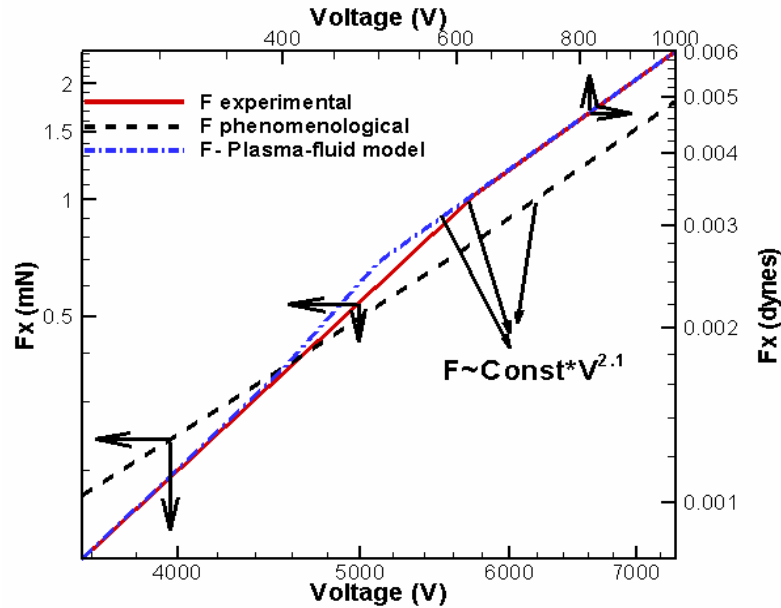


Figure 45 F_x power-law dependence on voltage is compared for two different numerical models- phenomenological and the first principle-based plasma fluid model along with experimental data of [26]. The arrows point to the set of axes chosen for each of the curves.

4.5. Summary

In this chapter, we developed and presented a modeling framework to study the operating mechanism and the thermo-fluid potential of a dielectric barrier discharge actuator.

A phenomenological model was developed assuming a linearized electric field distribution and constant species number density in the region. This approach is basically equivalent to solving a lowest order representation of the problem. Although it required experimental characterization to achieve closure, it was able to reasonably capture some of the wall-jet type flow features and other observed experimental outcomes. However, the need for extensive empirical data, such as the specie charge density, duty-cycle coefficient restricts the scope of this model.

In order to evolve the capability to the next level- a high fidelity, first principles based approach using a plasma-fluid (or plasma-hydrodynamic) continuum formulation

to model the discharge dynamics. The two-species plasma simulations revealed that the generation of the uni-directional momentum coupling is primarily caused by the combination of factors listed below:

- The asymmetry of the geometric arrangement
- Asymmetry of the voltage waveform
- Mobility of the dominant species resulting from the ionization

Overall, the paraelectric momentum coupling mechanism is due to the existence of a dominant force in one direction for a bulk of the time-period and for a lesser time in the other direction. The cumulative effect over time is primarily responsible for the uni-directional coupling. Efficiency of the plasma actuator was analyzed using asymmetric sawtooth waveforms which revealed that the positive going voltage is the most efficient force generating part of the half-cycle. The geometric effects analyzed revealed that the presence of a larger lower electrode will increase the discharge formation region, but will lead to diminishing returns due to a weakening discharge.

Parametric studies such as sensitivity to voltage and frequency were conducted. The effect of frequency was quite modest as compared to the sensitivity to the applied voltage which showed a power-law dependence on the voltage for the measure force in the domain. This power-law relationship showed substantial similarity to the experimental measurements and the phenomenological model.

It is worth noting here, that for the helium gas the observed species number density ($O(10^9)/\text{cm}^3$) is a couple of orders of magnitude smaller than that observed for air ($O(10^{11})/\text{cm}^3$). Also, the force measurement shown is for a unit centimeter length of the actuator in the spanwise direction and explains the very small realized in the high-fidelity

approach. The quadratic dependence of the force on the voltage is significant for realizing large momentum effects using relatively small increases in voltage.

CHAPTER 5 SUMMARY AND FUTURE WORK

5.1 Summary and Conclusions

A glow discharge-induced fluid dynamics model has been proposed where the plasma and the neutral flow are modeled as a two-fluid system with the plasma dynamics and the fluid dynamics solved separately. As a first step we, present an argument to decouple the plasma dynamics and the fluid dynamics using the disparity in the time-scales of the associated physics. The present regime of interest, which is the low Reynolds number flow, operates at a much slower time-scale as compared to the faster discharge breakdown and evolution processes, generated by the high frequency applied voltage. The success of this multi-scale handling of the plasma-fluid flow system will now be determined by an efficient treatment of the plasma model.

To integrate the plasma dynamics and the fluid dynamics, a body force model was developed to represent the effects of the discharge. The instantaneous body force which is the local Lorentz force acting on the charged species operates on the plasma scales and need to be averaged over the smallest fluid dynamic time scale.

Two modeling approaches have been developed.

(i) A phenomenological modeling approach based on linearized force distribution and experimentally observed discharge structure was developed. This model though requires the identification of empirical constants, showed reasonable qualitative agreement with the experimentally observed flow features. This model also captured parametric

dependencies such as the dependence of the force on the voltage comparable to that obtained by the first-principle based approaches and experimental studies.

This approach obviates the need for computing accurate descriptions of the plasma species and hence, the electric field distribution. This model, though required experimental characterization to achieve closure, was able to capture some of the reasonable flow features such as, the wall jet formation and other observed experimental outcomes.

(ii) In order to evolve the capability to the next level- a high fidelity, first principles based –approach using a plasma-fluid (or plasma-hydrodynamic) continuum formulation to model the discharge dynamics. First, a one-dimensional two-species plasma model with reduced chemistry served as a sample test problem for validating the input modeling data and in identifying the various time-scales and modeling limitations. The model was in reasonable quantitative agreement with the experimental results.

To extend to multiple dimensions, an operator splitting algorithm capable of handling multiple time-scales was employed. The resulting multi-scale algorithm enabled the integration of the overall system at the slowest species convection time-scale which is 100 times the dielectric relaxation time-scale. The asymmetric plasma discharge in helium has at 300 torr and 300 K , modeled using the hydrodynamic-plasma model showed characteristic temporal and spatial structure which was consistent with the experimentally observed results of Enloe et al.[21] for atmospheric air. Furthermore, the following conclusions can be drawn. The two-species plasma simulations revealed that the generation of the uni-directional momentum coupling is primarily caused by the combination of factors listed below:

- The difference in the mobility or convection of the two plasma species considered- the faster electron species and the slower ion species
- Difference in the behavior of the absorbing conductor surface (electrode) and the self-limiting charge build-up of the electrode.
- Lastly, the geometric asymmetry due the downstream submerged electrode is closely coupled to the two above mentioned observations.

Overall, the paraelectric momentum coupling mechanism is due to the cumulative effect over time of the force field in the domain, as seen from our computations. The asymmetric sawtooth waveforms revealed that the positive going voltage is the most efficient force generating part of the half-cycle. The geometric effects analyzed revealed that the presence of a larger lower electrode will increase the discharge formation region, but will lead to diminishing returns due to a weakening discharge.

Parametric studies such as sensitivity to voltage and frequency were conducted. The applied voltage revealed a power-law dependence on the voltage for the measured force in the domain. This power-law relationship showed bears resemblance to the experimental measurements and the phenomenological model.

Finally, the neutral fluid on which the plasma acts is assumed incompressible because of the low speed regime of interest in this dissertation and the experimental observations indicating very little heating and hence minimal to no buoyancy related effects. The effects considered in this dissertation are purely mechanical in nature as we assumed the discharge to be in local thermal equilibrium by assuming an efficient collision process leading to more momentum exchange and less thermal heating. However, future efforts might attempt to investigate the potential of these actuators for

converting the input electric power to generate gas heating effects. Based on the phenomenological model for air, the current actuator configuration presented in this dissertation displayed sufficient potential for flow control applications for Re in the range of $O(1000)$. The plasma induced body force effect is similar in nature to the pressure gradient and stronger voltages can enhance the potential performance range of these actuators to $O(10000-100000)$ taking advantage of the power-law dependence.

5.2 Future Work

Based on the accomplishments to date, further efforts are proposed in the following to further advance the predictive capabilities, and to extend the approach to engineering applications including drag reduction, thermal management, and flow control.

- The multi-scale nature of the solution can be further aided by using local grid refinements techniques near the regions of sharp ionization wave propagation. The time and length scales in these regions are of $O(\sim 10^6)$, and consequently, can be better resolved with grid refinement. As evidenced in Chapter 4, the discharge is heavily characterized by breakdown phases followed by the convection phase where the charge species accumulate on the material surface. These processes act in quick succession resulting in the presence of ionization wave-type phenomena which is the reason for the stiffness in the present case of plasma modeling.
- Performance, stability and accuracy considerations of the sequential algorithm employed in the present study should be further assessed with different physical and operating parameters.

- The study of fluid–plasma interactions is common in the area of flow-control applications with a fluid such as air. In such cases the plasma chemistry needs to be modeled in a mixture of nitrogen and oxygen. For example, the role of chemistry, i.e., how the presence of both heavy negative and positive ions can affect resulting flow structure needs to be investigated. In the present effort, only Helium gas was considered due to the wealth of modeling literature available. However, as we have seen, the discharge evolution is critically dependent on the nature and mobility of the individual species concerned. Hence, in order to get a realistic representation of the performance of the actuator in air, we will need to expand the chemistry modeling.

LIST OF REFERENCES

1. S. Hippler, M. Pfau, K.H. Schmidt, and Schoenbach, *Low Temperature Plasma Physics: Fundamental Aspects and Applications*, Wiley-VCH, Berlin (2001).
2. W.Siemens, "Plasma discharges," Poggendorffs Ann. Phys. Chem. 102, pp 66 (1857).
3. U.Kogelschatz, B.Eliasson and W.Egli, "From ozone generators to flat television screens: history and future potential of dielectric-barrier discharges," Pure. Appl. Chem., 71(10), pp 1819-1828 (1999).
4. J.R.Roth, D.M.Sherman and S.P. Wilkinson, "Boundary layer flow control with a one atmosphere uniform glow discharge," AIAA paper 98-0328, 36th AIAA Aerospace Sciences Meeting, Reno NV, January 12-15 (1998).
5. S.Kanazawa, M. Kogoma, T.Moriwaki and S.Okazaki, "Stable glow plasma at atmospheric pressure," Phys. D. Appl. Phys. 21, pp 838 (1988).
6. F.Massines, R.Ben Gadri, A.Rabehi, Ph.Decomps, P.Segur and Ch.Mayoux, "Experimental and theoretical study of a glow discharge at atmospheric pressure controlled by dielectric barrier," J. Appl. Phys, 83(6), pp 2950-2957 (1998).
7. J.R.Roth, "Electrohydrodynamically induced airflow in a one atmosphere uniform glow discharge surface plasma", Paper 6P-67, Proc. 25th IEEE International Conference on Plasma Science, Raleigh, NC June 1-4, pp 291 (1998).
8. B.L.Smith and A.Glezer, "The formation and evolution of synthetic jets," Phys. of Fluids, 10(9), pp 2281-2297 (1998).
9. W.Shyy, B.Jayaraman and A.Anderson, "Modeling of glow-discharge induced flow dynamics," J. Appl. Phys., 92(11), pp 6434-6443 (2002).
10. J.S.Shang, "Recent research in magneto-aerodynamics," Prog. Aero. Sci., 37, pp 1-20, (2001).
11. R.Rivir, A.White, C.Carter, B.Ganguly, J.Jacob, A.Forelines and J.Crafton, "AC and pulsed plasma flow control," AIAA paper 2004-0847, 42nd Aerospace Sciences Meet & Exhibit, Reno, NV, Jan 5-8 (2004).

12. S.Leonov, V.Bityurin and D.Yarantsev, "The effect of plasma induced separation," AIAA paper 2003-3853, 34th AIAA Plasmadynamics and Lasers Conference, Orlando, FL, Jun 23-26 (2003).
13. Y.B.Golubovskii, V.A Maiorov, J.Behnke and J.F.Behnke, "Modeling of homogeneous barrier discharge in helium at atmospheric pressure," J.Phys. D: Appl. Phys. 36, pp 39-49 (2003).
14. D.V.Gaitonde, M.R.Visbal and S.Roy, "Control of flow past a wing section with Plasma-based Body forces," AIAA paper 2005-5302, 36th Plasma Dynamics and Lasers Conference, Toronto, 6-9 June (2005).
15. S.Roy and D.V.Gaitonde, "Modeling surface discharge effects of atmospheric RF on gas flow control," AIAA paper 2005-0160, 43rd AIAA Aerospace Sciences Meeting, Reno NV, January 10-13 (2005).
16. S.Roy and D.V.Gaitonde, "Multidimensional collisional dielectric barrier discharge for flow separation control at atmospheric pressures," AIAA paper 2005-4631, 35th AIAA Fluid dynamics conference, Toronto, Canada, 6-9 June (2005).
17. K.P.Singh and S.Roy, "Simulation of an asymmetric single dielectric barrier plasma actuator," J. App. Phys. 98, pp 083303-1 (2005).
18. H.Kumar and S.Roy, "Multidimensional hydrodynamic plasma-wall model for collisional plasma discharges with and without magnetic-field effects," Phys. Of Plasmas, 12, pp 093508 (2005).
19. S.Thakur, J.Wright and W.Shyy, "STREAM: A computational fluid dynamics and heat transfer Navier-Stokes solver: theory and applications," Application manual, Gainesville, FL: Streamline Numerics, Inc. (2002).
20. R.Ben Gadri, "One atmospheric glow discharge structure revealed by computer modeling," IEEE Trans. Plasma Sci., 27(1) (1999).
21. C.L.Enloe, T.E.Mclaughlin, R.D.Van Dyken and K.D. Kachner, "Mechanisms and responses of a single dielectric barrier plasma actuator: plasma morphology," AIAA J. 42(3) (2004).
22. C.L.Enloe, T.E.Mclaughlin, R.D.Van Dyken, K.D. Kachner, E.J.Jumper, T.C.Corke, M.Post and O.Haddad "Mechanisms and responses of a single dielectric barrier plasma actuator: geometric effects," AIAA J. 42(3) (2004).
23. C.L.Enloe, T.E.Mclaughlin, R.D.Van Dyken and J.C.Fischer, "Plasma structure in the aerodynamic plasma actuator," AIAA paper 2004-0844, 42nd Aerospace Sciences Meet & Exhibit, Reno, NV, Jan 5-8, 2004.
24. T.C.Corke and E.Matlis, "Phased plasma arrays for unsteady flow control," AIAA paper 2000-2323, Fluids 2000, Denver, CO, June 19-22 (2000).

25. T.C.Corke, E.J.Jumper, M.L.Post, D.Orlov and T.E.Mclaughlin, "Application of weakly-ionized plasmas as wing flow-control devices," AIAA paper 2002-0350, 41st Aerospace Sciences Meeting & Exhibit, Reno, NV, Jan 6-9 (2003).
26. R.Van Dyken, T.E.Mclaughlin and C.L.Enloe, "Parametric investigations of a single dielectric barrier plasma actuator," AIAA paper 2004-846, 42nd Aerospace Sciences Meet & Exhibit, Reno, NV, Jan 5-8 (2004).
27. M.L.Post and T.C.Corke, "Seperation control on high angle of attack airfoil using plasma actuators," AIAA paper 2003-1024, 41st Aerospace Sciences Meet & Exhibit, Reno, NV, Jan 6-9 (2003).
28. B.Jayaraman, S.Thakur and W.Shyy, "Modeling of dielectric barrier discharge and resulting fluid dynamics," AIAA paper 2006-0686, 44th Aerospace Sciences Meeting & Exhibit, Reno, NV, January 9-12 (2006).
29. B.Jayaraman, W.Shyy and S.Thakur, "Modeling of fluid dynamics and heat transfer induced by dielectric barrier plasma actuator," J. Heat Trans., Invited paper in the Special Edition in Honour of Dr. S.V. Patankar, submitted for review.
30. R.B.Campbell, R.Veerasingham and R.T.Mcgrath, "A two-dimensional multispecies fluid model of the plasma in an AC plasma display panel," IEEE Trans. on Plasma Sci., 23(4), pp 698-708 (1995).
31. J.P.Boeuf and L.C.Pitchford, "Two-dimensional model of a capacitively coupled rf discharge and comparisons with experiments in the gaseous electronics conference reference reactor," Phys. Rev. E, 51(2), pp 1376-1390 (1995).
32. J.R.Roth, *Industrial Plasma Engineering: Vol. I-Principles*, IOP, Bristol (1995).
33. J.R.Roth, *Industrial Plasma Engineering: Vol. II- Applications to Non-thermal Plasma Processing*, IOP, Bristol (2001).
34. D.Lee, J.M.Park, S.H.Hong and Y.Kim, "Numerical simulation on mode transition of atmospheric dielectric barrier discharge in helium-oxygen mixture," IEEE Trans. on Plasma Sci., 33(2), pp 949-957 (2005).
35. C.Baird, C.L.Enloe, T.E.Mclaughlin and J.W.Baughn, "Acoustic testing of dielectric barrier discharge (DBD) plasma actuator," AIAA paper 2005-0565, 43rd Aerospace Sciences meeting and Exhibit, Reno, NV, Jan 10-13 (2005).
36. C.L.Enloe, T.E.Mclaughlin, G.I.Font and J.W.Baughn, "Parameterization of temporal structure in the single dielectric barrier aerodynamic plasma actuator," AIAA paper 2005-0564, 43rd AIAA Aerospace Sciences Meeting and Exhibit, Reno, NV, Jan 10-13 (2005).

37. T.N.Jukes, K.S.Choi, G.A.Johnson and S.J.Scott, "Characterization of surface plasma-induced wall flows through velocity and temperature measurements", AIAA J., 44(4), pp 764-771 (2005).
38. T.N.Jukes, K.S.Choi, G.A.Johnson and S.J.Scott, "Turbulent boundary-layer control for drag reduction using surface plasma," AIAA paper 2004-2216, 2nd AIAA Flow Control Conference, Portland, Oregon, Jun 28- Jul 1 (2004).
39. J.R.Roth, H.Sin, R.C.M.Madhan and S.P.Wilkinson, "Flow re-attachment and acceleration by paraelectric and peristaltic electrohydrodynamic effects," AIAA paper 2003-0351, 41st Aerospace Sciences Meet & Exhibit, Reno, NV, Jan 6-9 (2003).
40. J.List, A.R.Byerly, T.E.Mclaughlin and R.D.Vandyken, "Using plasma actuator to control laminar separation on a linear cascade turbine blade," AIAA paper 2003-1026, 41st Aerospace Sciences Meet & Exhibit, Reno, NV, Jan 6-9 (2003).
41. A.Santhanakrishnan, N.J.Pern, K.Ramkumar, A.Simpson and J.D.Jacob, "Enabling flow control technology for low speed UAV's," AIAA paper 2005-6960, Infotech at aerospace, Arlington, Virginia, Sept. 26-29 (2005).
42. B.Goskel, D.Greenblatt, I Rechenberg, C.N.Nayeri and C.O.Paschereit, "Steady and unsteady plasma wall jets for separation and circulation control," AIAA paper 2006-3686, 3rd AIAA Flow Control Conference, San Francisco, CA, Jun 5-8 (2006).
43. T.C.Corke, B.Mertz and M.P.Patel, "Plasma flow control optimized airfoil," AIAA paper 2006-1208, 44th AIAA Aerospace Sciences Meeting and Exhibit, Reno, NV, Jan 9-12 (2006).
44. S.Chan, X.Zhang and S.Gabriel, "The attenuation of cavity tones using plasma actuators," AIAA paper 2005-2802, 11th AIAA/CEAS Aeroacoustics Conference (26th AIAA Aeroacoustics Conference) 23 - 25 May 2005, Monterey, California (2005).
45. R.Rivir, A.White, C.Carter, B.Ganguly, A.Forelines and J.Crafton, "Turbine flow control, plasma flows," AIAA paper 2003-6055, 41st Aerospace Sciences Meet & Exhibit, Reno, NV, Jan 6-9 (2003).
46. A.Soldati and S.Banerjee, "Turbulence modification by large-scale organized electrohydrodynamic flows," Phys. of Fluids, 10(7), pp 1742-1756 (1998).
47. A.Soldati and C.Marchioli, "Prospects for modulation of turbulent boundary layer by EHD flows," Turbulence Structure and Modulation, Springer-Verlag, Wien, pp 119-160 (2001).

48. S.P.Wilkinson, "Investigation of an oscillating surface plasma for turbulent drag reduction," AIAA paper 2003-2199, 41st Aerospace Sciences Meet & Exhibit, Reno, NV, Jan 6-9 (2003).
49. Y.Du, V.Symeonidis and G.E.Karniadakis, "Drag reduction in wall-bounded turbulence via a transverse traveling wave," J. Fluid Mech., 457, pp 1-34 (2002).
50. M.R.Dhanak and C.Si, "On reduction of turbulent wall friction through spanwise wall oscillations," J. Fluid Mech., 383, pp 175-195 (1999).
51. K.D.Hall, E.J.Jumper, T.C.Corke and T.E.Mclaughlin, "Potential flow model of a plasma actuator as a lift enhancement device," AIAA paper 2005-0783, 43rd Aerospace Sciences Meeting and Exhibit, Reno, NV, Jan 10-13 (2005).
52. D.M.Orlov and T.C.Corke, Numerical simulation of aerodynamic plasma actuators," AIAA paper 2005-1083, 43rd Aerospace Sciences Meeting and Exhibit, Reno, NV, Jan 10-13 (2005).
53. J. Tepper and M.Lindmayer, "Investigations on two different kinds of homogeneous barrier discharges at atmospheric pressure," Proc. of HAKONE VII, 7th Int. Symp. On High Pressure Low Temperature Plasma Chemistry, Greifswald, vol. 1, Sep 10-13, pp 38 (2000).
54. B. Eliasson and U.Kogelschatz, "Modeling and applications of silent discharge plasmas," IEEE Trans. Plasma Sci. 19(2), pp 309-323 (1991).
55. E.Gogolides and H.H.Sawin, "Continuum modeling of radio-frequency glow discharges. I. Theory and results for electropositive and electronegative gases," J. Appl. Phys. 72(9), pp 3971-3987 (1992).
56. L.Mangolini, K.Orlov, U.Kortshagen, J.Heberlein and U.Kogelschatz, "Radial structure of a low-frequency atmospheric-pressure glow discharge in helium," Applied physics letters, 80(10), pp 1722-1724 (2002).
57. Y.B.Golubovskii, V.A Maiorov, J.Behnke and J.F.Behnke, "Study of homogeneous glow-like discharge in nitrogen at atmospheric pressure," J.Phys. D: Appl. Phys. 37, pp 1346-1356 (2004).
58. P.Segur and F.Massines, "The role of numerical modeling to understand the behavior and to predict the existence of an atmospheric pressure glow discharge controlled by a dielectric barrier," Proc. Of the XIIIth Int. Conf. of Gas Discharges and their applications, Glasgow, Sep. 3-8, pp 15-24 (2000).
59. X.Xu and M.J.Kushner, "Multiple microdischarges dynamics in dielectric barrier charges," J. Appl. Phys. 84(8), pp 4153-4160 (1998).

60. Y.B.Golubovskii, V.A Maiorov, J.Behnke and J.F.Behnke, "Influence of interaction between charged particles and dielectric surface over a homogeneous barrier discharge in nitrogen," *J.Phys. D: Appl. Phys.* 35, pp 751-761 (2002).
61. J.Shin and L.L.Raja, "Dynamics of pulse phenomena in helium dielectric-barrier atmospheric-pressure glow discharges," *J. Appl. Phys.* 94(12), pp 7408-7415 (2003).
62. L.Mangolini, C.Anderson, J.Heberlein and U.Kortshagen, "Effects of current limitation through the dielectric in atmospheric pressure glows in helium," *J.Phys D: Appl. Phys.*, 37, pp 1021-1030 (2004).
63. F.Tochikubo, T.Chiba and T.Watanabe, "Structure of low-frequency helium glow discharge at atmospheric pressure between parallel plate dielectric electrodes," *Jpn. J. Appl. Phys.* 38, pp 5244-5250 (1999).
64. T.R.Govindan and M.Meyappan, "One-dimensional modeling studies of the gaseous electronic conference RF reference cell," *J. Research, NIST*, 100(4), pp 463-472 (1995).
65. X.Yuan and L.L.Raja, "Computational study of capacitively coupled high-pressure glow discharges in helium," *IEEE Trans. Plasma Sci.*, 31(4), pp 495-503 (2003).
66. J.P.Boeuf, "Numerical modeling of rf glow discharges," *Phys. Rev. A*, 36(6), pp 2782-2792 (1987).
67. C.K.Birdsall, "Particle-in-cell charged-particle simulations, plus Monte Carlo collisions with neutral atoms," *IEEE Trans. Plasma Sci.*, 19(2), pp 65-85 (1991).
68. T.E.Nitschke and D.B.Graves, "A comparison of particle in cell and fluid model simulations of low-pressure radio frequency discharges," *J. Appl. Phys.* 76(10), pp 5646-5660 (1994).
69. S.K.Dhali and P.F.Williams, "Two-dimensional studies of streamers in gases," *J. Appl. Phys.* 62, pp 4696 (1987).
70. D.P Lymberopoulos and D.J.Economou, "Two-dimensional self-consistent radio frequency plasma simulations relevant to the gaseous electronics conference RF refernce cell," *J. Research of the NIST*, 100(4) (1995).
71. J.Meunier, Ph.Belenguer and J.P.Boeuf, "Numerical model of an ac plasma display panel cell neon-xenon mixtures," *J. Appl. Phys* 78(2), pp 731-745 (1995).
72. R. Veerasingham, R.B.Campbell and R.T.Mcgrath, "One-dimensional single and multipulse simulations of the ON/OFF voltages and the bistable margin for He, Xe filled plasma display panels," *IEEE Trans. Plasma Sci.*, 24(6), pp 1399-1410 (1996).

73. W.M.Hilbun and B.J.Case, "Preliminary development of a computational model of a dielectric barrier discharge," AIAA paper 2005-1176, 43rd Aerospace Sciences Meeting and Exhibit, Reno, NV, Jan 10-13 (2005).
74. B.Jayaraman and W.Shyy, "Flow control and thermal management using dielectric glow discharge concepts," AIAA paper 2003-3712, 33rd AIAA Fluid Dynamics Conference and Exhibit, Orlando, June 23-26 (2003).
75. K.P.Singh, S.Roy and D.V.Gaitonde, "Modeling of dielectric barrier discharge plasma actuator with atmospheric air chemistry," AIAA paper 2006-3381, 37th AIAA Plasmadynamics and Lasers conference, San Francisco, CA, 5-8 June (2006).
76. M.R.Visbal, D.V.Gaitonde and S.Roy, "Control of transitional and turbulent flows using plasma-based actuators", AIAA paper 2006-3230, 36th AIAA Fluid Dynamics Conference and Exhibit, San Francisco, CA, 5-8 June, 2006.
77. M.E.Riley, K.E.Greenberg, G.A.Hebner and P.Drallos, "Theoretical and experimental study of low-temperature, capacitively coupled, radio-frequency helium plasmas," J. Appl. Phys, 75(6), pp 2789-2798 (1994).
78. M.J.Kushner, "Mechanisms for power deposition in Ar/SiH₄ capacitively coupled RF discharges," IEEE Trans. Plasma Sci., 14(4), pp. 188 (1985).
79. R.W.Boswell and I.J.Morey, "Self-consistent simulation of a parallel-plate rf discharge," Appl. Phys. Lett. 52(1), pp 21-23 (1988).
80. M.Surendra and D.B.Graves, "Particle simulations of radio-frequency glow discharges," IEEE Trans. Plasma Sci., 19(2), pp 144-157 (1991).
81. W.Nicholas G.Hitchon, T.J.Sommerer and J.E Lawler, "A self-consistent kinetic plasma model with rapid convergence," IEEE Trans. Plasma Sci., 19(2), pp 113-121 (1991).
82. J.V.DiCarlo and M.J.Kushner, "Solving the spatially dependent Boltzmann's equation for the electron velocity distribution using flux corrected transport," J. Appl. Phys. 66(12), pp 5763-5774 (1989).
83. W.N.G.Hitchon, D.J.Koch and J.B.Adams, "An Efficient scheme for convection dominated transport," J. Comput. Phys. 83, 79 (1989).
84. Ph.Belenguer and J.P.Boeuf, "Transition between different regimes of rf glow discharges," Phys. Rev. A, 41, pp 4447 (1990).
85. A.Fiala, L.C.Pitchford and J.P.Boeuf, "Two-dimensional, hybrid model of low-pressure glow discharges," Phys. Rev. E, 49(6), pp 5607 (1994).

86. P.Colella, M.R.Dorr and D.D.Wake, "A conservative finite difference method for the numerical solution of plasma fluid equations," *J. Comp. Phys.* 149, pp 168-193 (1999).
87. M.Surendra, "Radio frequency discharge benchmark model comparison," *Plasma Sources Sci. Technol.* 4, pp 56-73 (1995).
88. P.L.G. Ventzek, T.J.Sommerer, R.J.Hoekstra and M.J.Kushner, "Two-dimensional hybrid model of inductively coupled plasma sourced for etching," *Appl. Phys Lett.* 62, pp 3247-3249 (1993).
89. T.J.Sommerer and M.J.Kushner, "Numerical investigation of the kinetics and chemistry of rf glow discharge plasmas sustained in He, N₂, O₂, He/ N₂/ O₂, He/CF₄/O₂, and SiH₄/NH₃ using a Monte Carlo-fluid hybrid model," *J. Appl. Phys.* 71(4), pp 1654-1673 (1992).
90. E.P.Hammond, K.Mahesh and P.Moin, "A Numerical method to simulate radio-frequency plasma discharges," *J.Comp. Phys.*, 176, pp 402-429 (2002).
91. Shyy, W. "A Study of finite difference approximations to steady-state, convection dominated flow problems," *J. Comp. Phys.* 57, pp 415-438 (1985).
92. D.A.Knoll and D.E.Keyes, "Jacobian-free Newton Krylov Methods: a Survey of Approaches and Applications," *J. Comp. Phys.* 193, pp 357-397 (2004).
93. E. Turkel, "Review of preconditioning methods for fluid dynamics," NASA CR-189712, ICASE Report no 92-47 (1992).
94. C.L.Merkle, J.Y.Sullivan, P.E.O.Buelow and S.Venkateswaran, "Computations of flows with arbitrary equations of state," *AIAA J.* 36(4), pp. 515, 1998.
95. D.A.Schwer, P.Lu, W.H.Green Jr. and V.Semiao, "A Consistent-splitting approach to computing stiff steady-state reacting flows with adaptive chemistry," *Comb. Theory Modeling*, 7, pp 383-399 (2003).
96. G.J.M. Hagelaar and G.M.W. Kroesen, "Speeding up fluid models for gas discharges by implicit treatment of the electron energy source term," *J. Comp. Phys.* 159(1), pp 1-12 (2000).
97. T.R.A.Bussing and E.M.Murman, "Finite-volume method for the calculation of compressible chemically reacting flows," *AIAA J.* 26(9), pp 1070-1078.
98. S.Yoon and A.Jameson. "Lower-upper symmetric Gauss-Seidel method for the Euler and Navier-Stokes Equations," *AIAA J.* 26(9), pp1025 (1988).
99. J.G.Verwer, "Explicit Runge-Kutta methods for parabolic partial differential equations," *Appl. Numer. Math.* 22, pp 359-379 (1996).

100. M.Valorani and D.A. Goussis, "Explicit time-scale splitting algorithms for stiff problems: auto-ignition of gaseous mixtures behind a steady shock," J. Comp. Phys. 169 pp 44-79 (2001).
101. E.S.Oran and J.P.Boris, *Numerical Simulation of Reactive Flow*, Cambridge university press, 2nd Edition (2001).
102. H.N.Najm, P.S.Wyckoff and O.M. Knio, "A semi-implicit numerical scheme for reacting flow," J. Comp. Phys. 143, pp 381-402 (1998).
103. P.N.Brown, G.D.Byrne, and A.C.Hindmarsh, "VODE: A variable coefficient ODE solver," SIAM J. Sci. Stat. Comput. 10, pp 1038 (1989).
104. R.Tyson, L.G.Stern and R.J.Leveque, "Fractional steps method applied to chemotaxis model," J. Math. Biol. 41, pp 455-475 (2000).
105. S.D.Cohen, A.C.Hindmarsh, "CVODE: a stiff/nonstiff ODE solver in C," Comp.Phys. 10(2), pp 138-143 (1996).
106. G.Strang, "On the construction and comparison of difference schemes," SIAM J. Num. Anal. 21, pp 994-1011 (1969).
107. B.Sportissee, "An analysis of operator splitting techniques in the stiff case," J. Comp. Phys. 161, pp 140-168 (2000).
108. O.M.Knio, H.N.Najm and P.S.Wyckoff, "A semi-implicit numerical scheme for reacting flow," J.Comp. Phys. 154, pp 428-467 (1999).
109. G.J.M.Hagelaar, F.J. de Hoog and G.M.W. Kroesen, "Boundary conditions in fluid models of gas discharges," Phs. Rev. E. 62(1), pp 1452-1454 (2000).
110. C.Enloe, T.Mclaughlin, R.Van Dyken and J.Fischer, "Plasma structure in the aerodynamic plasma actuator," AIAA paper 2004-0846, 42nd AIAA Aerospace Sciences Meeting and Exhibit, Reno, Nevada, Jan. 5-8 (2004).
111. S.Thakur and J.Wright, "A multi-block operator splitting algorithm for unsteady flows at all speeds in complex geometries," Int. J. Num. Meth. Fluids, 46, pp 383-413 (2004).
112. W.Shyy, S.Thakur, H.Ouyang, J.Liu and E.Blosch, *Computational Techniques for Complex Transport Phenomena*, Cambridge University Press, Cambridge, United Kingdom (1997).
113. W.Shyy, *Computational Modeling for Fluid Flow and Interfacial Transport*, Elsevier, Amsterdam, Netherlands (1994).

114. M.Surendra, D.B.Graves and G.M.Jellum, "Self-consistent model of a direct-current glow discharge: Treatment of fast electrons," Phys. Rev. A, 41(2), pp 1112-1126 (1990).
115. D.V.Gaitonde, M.R.Visbal and S.Roy, "A coupled approach for plasma-based flow control simulations of wing sections," AIAA paper 2006-1205, 44th AIAA Aerospace Engineering Sciences Meeting and Exhibit, Reno, NV, 9-12 Jan (2006).
116. P.Colella, M.R.Dorr and D.D.Wake, "Numerical solution of plasma fluid equations using locally refined grids," J. Comp. Phys. 152, pp 550-583 (1999).

BIOGRAPHICAL SKETCH

Balaji Jayaraman was born in the city of Madras in southern India in 1980. After completing his preliminary schooling, he was fortunate to pursue his Bachelor of Technology degree in naval architecture and ocean engineering at the Indian Institute of Technology, Madras. On completion of his B.Tech, he began his graduate school to pursue his Ph.D. at UF under Dr. Wei Shyy in the fall of 2001.